PE&RS
January 2023 Volume 89, Number 1

Photogrammetric Engineering & Remote Sensing *The official journal for imaging and geospatial information science and technology*

GEO WEEK

FEBRUARY 13-15, 2023
DENVER, CO - USA
geo-week.com

The intersection of **geospatial** + the **built world**

asprs THE IMAGING & GEOSPATIAL INFORMATION SOCIETY

Learn more!
geo-week.com/asprs

Geo Week is proud to partner with ASPRS to bring the ASPRS Annual Conference and exclusive workshops to Geo Week with sessions including:

- Ethical and Legal Concerns of AI-Driven Remote Sensing Applications
- Remote Sensing Data Quality and Interoperability Requirements
- Incorporating Lidar into Remote Sensing Projects
- Photogrammetric Processing and Applications
- Commercial Perspectives on the Uses of Imagery in GIS
- Guidelines and Standards for Topographic and Bathymetric Lidar
- Advanced Remote Sensing Analysis using Machine Learning and AI
- Revision of the ASPRS Positional Accuracy Standards for Geospatial Data
- Climate Change and Urban Analysis
- UAS Data Processing and Applications

ASPRS member discounts are available through the member portal. Geo Week conference passes can be purchased at an additional discount rate when bundled with the ASPRS Annual Conference Pass.

INDUSTRIES SERVED

Architecture, Engineering & Construction
Asset & Facility Management
Disaster & Emergency Response
Earth Observation & Satellite Applications
Energy & Utilities
Infrastructure & Transportation
Land & Natural Resource Management
Mining & Aggregates
Surveying & Mapping
Urban Planning/ Smart Cities

EVENT PARTNERS

asprs THE IMAGING & GEOSPATIAL INFORMATION SOCIETY
MAPPS
USIBD U.S. Institute of BUILDING DOCUMENTATION
WGIC World Geospatial Industry Council

Produced by diversified COMMUNICATIONS

To have your press release published in *PE&RS*, contact Rae Kelley, rkelley@asprs.org.

INDUSTRYNEWS

ANNOUNCEMENTS

NV5 Global, Inc., a provider of technology, conformity assessment, and consulting solutions, announced today that it has been awarded a $9 million contract by the National Oceanic and Atmospheric Administration's (NOAA) National Geodetic Survey to provide topobathymetric lidar, 4-band imagery, and mapping of the Maine shoreline.

Under the two-year contract, NV5 will deliver accurate and consistent measurement of the shoreline to support marine navigation safety, nautical charting, marine debris surveys, and marine resource management assessments. Geospatial data for the project will be obtained through topobathymetric lidar collection and processing and 4-band imagery of 3,115 sq miles of coastal Maine to provide views of both the shoreline and shallow water coastal area.

"We are pleased to continue our work with NOAA to support the accurate measurement of the nation's shoreline," said Dickerson Wright, PE, Chairman and CEO of NV5. "Our innovative work with topobathymetric lidar has made shoreline data acquisition possible in some of the most difficult coastal terrains and will support the work of marine industries and multiple government organizations."

For more information, visit https://www.nv5.com/geospatial/.

At the 2022 Technology Impact Awards in British Colombia, the Vancouver International Airport (YVR) recently received the Excellence in Industry Innovation Award by the BC Tech Association. The award-winning project involved a Digital Twin that was produced by GEO1 using **RIEGL** LiDAR and in partnership with GeoSim and Talon Helicopters.

A Digital Twin is a virtual representation that serves as the real-time digital counterpart of a physical object or process. Digital Twin models are being used at an increasing rate by airports to anticipate passenger movement and deploy resources, such as staff and vehicles, accordingly. They can also be used to develop simulations for training ground personnel and first responders, as well as to model emergency events or visualize future infrastructure development.

Once the data for YVR had been acquired by GEO1 with two RIEGL VUX-1LR Long Range Laser Scanners at an oblique angle to get improved coverage, the data could be stitched together by GeoSim to produce the final 3D model.

As the second largest airport in Canada, this Digital Twin allows YVR to be positioned at the forefront of innovation in the industry.

With an array of Phase One 150-megapixel cameras and RIEGL VUX-1LR Long Range Laser Scanners, the GEO1 team collected data at the rate of almost 1,000 megabytes per second.

For more information, visit https://newsroom.riegl.international/.

The U.S. Department of Agriculture (USDA) has consolidated several of its major geospatial programs under one new Blanket Purchase Agreement (BPA) called the PINE Aerial Imagery contract. As one of the award recipients, Surdex Corporation will provide geospatial services under five Farm Production and Conservation (FPAC) programs:

- National Agriculture Imagery Program (NAIP), a state-based orthoimagery program acquiring imagery during peak agricultural growing seasons.
- National Resource Inventory (NRI), a multi-agency, state-based program of high-resolution orthoimagery for the National Resource Conservation Service (NRCS).
- Stewardship Lands Inventory (SLI), an easement-based collection program for high-resolution orthoimagery supporting NRCS conservation easement programs.
- Resource, for collection of high-resolution orthoimagery for the USFS.
- Ad hoc and Disaster Support, which covers small to medium-sized areas identified for various USDA projects.

The 5-year PINE contract is being administered through the General Services Administration's (GSA) Multiple Award contract vehicle and will operate through mid-November of 2026.

For more information, visit https://www.surdex.com/blog/category/news/.

CALENDAR

- 27 January, **ASPRS GeoByte — Allen Coral Atlas: A New Technology for Coral Reef Conservation**. For more information, visit https://www.asprs.org/geobytes.html.
- 15-17 February, **ASPRS Annual Conference at Geo Week**, Denver, Colorado. For more information, visit https://my.asprs.org/2023conference.
- 5 May, **ASPRS GeoByte — SeaSketch 2.0: A New, Free and Open Source software Service for Map-based Surveys and Collaborative Geodesign.** For more information, visit https://www.asprs.org/geobytes.html.

PUBLISHING OPEN-ACCESS IN *PE&RS* IS NOW EASIER!

ASPRS is changing the subscription model of our monthly journal, *PE&RS*. ASPRS is waiving open-access fees for primary authors from subscribing institutions. Additionally, primary authors who are Individual Members of ASPRS will be able to publish one open-access article per year at no cost and will receive a 50% discount on open-access fees for additional articles.

- **Open Access matters!** By providing unrestricted access to research we can advance the geospatial industry and provide research that is available to everyone.
- **Institutions and authors receive more recognition!** Giving permission to everyone to read, share, reuse the research without asking for permission, as long as the author is credited.
- **Reputation matters!** Known for its high standards, *PE&RS* is the industry leading peer-review journal. Adding open access increases authors' visibility and reputation for quality research.
- **Fostering the geospatial industry!** Open access allows for sharing without restriction. Research is freely available to everyone without an embargo period.

Under the previous subscription model, authors and institutions paid $1500 or more in open-access fees per article. This will represent a significant cost savings. Open-access publications benefit authors through greater visibility of their work and conformance with open science mandates of funding agencies.

Subscriptions asprs.org/subscribe
Membership asprs.org/membership

asprs THE IMAGING & GEOSPATIAL INFORMATION SOCIETY

PE&RS
PHOTOGRAMMETRIC ENGINEERING & REMOTE SENSING
The official journal for imaging and geospatial information science and technology
January 2023 Volume 89 Number 1

COLUMNS

ANNOUNCEMENTS

DEPARTMENTS

See the Cover Description on Page 4

COVER DESCRIPTION

Along the coast of Senegal in West Africa, just a kilometer of beach separates the bright pink waters of Lake Retba from the dark blue-green waters of the Atlantic Ocean. But conditions at the lake (also called Lac Rose) are not always so rosy.

Located about 40 kilometers (25 miles) northeast of Dakar, Lake Retba attracts visitors who want to see its unique color and float in its salty, buoyant waters. With a concentration of salt that surpasses the Dead Sea, Lake Retba is also important to the local economy. Harvesters collect thousands of tons of salt from its waters each year, which is used locally for cooking and preserving food and is also exported to nearby countries.

The water's pink hue comes from Dunaliella salina—a single-celled algae that can tolerate salty environments. D. salina are a type of green algae, but under stressful conditions, such as high salinity or intense sunlight, they produce protective carotenoids, including orange-red beta carotene.

The lake is typically at its pinkest during the dry season (November to June) when there is persistent sunlight and high concentrations of salt. The top image, acquired by the Operational Land Imager (OLI) on Landsat 8, shows the lake on May 19, 2022, when waters appeared rosy.

The pink color fades during the region's wet season (July to October) when more clouds mean less sunlight and the waters become fresher due to rainwater. The bottom image, acquired with the Operational Land Imager-2 (OLI-2) on Landsat 9, shows the lake on September 16, 2022, when its color nearly matched the Atlantic Ocean.

The wet season in 2022 was especially wet. Bouts of torrential rain in early August and early September led to deadly flooding in Dakar and surrounding areas. The extreme rainfall impacted more than the lake's color; for example, floodwaters in September breached the lake's bank and washed away salt mounds that harvesters had collected there.

Lake Retba is the only pink lake in Africa, but the phenomenon occurs elsewhere around the planet. For example, Torrevieja Lagoon in Spain and Lonar Lake in India both take on rosy hues from the same single-celled algae.

NASA Earth Observatory images by Lauren Dauphin, using Landsat data from the U.S. Geological Survey. Story by Kathryn Hansen.

For more information, visit https://landsat.visibleearth.nasa.gov/view.php?id=150419.

asprs
THE IMAGING & GEOSPATIAL INFORMATION SOCIETY

PHOTOGRAMMETRIC ENGINEERING & REMOTE SENSING

JOURNAL STAFF

Publisher ASPRS
Editor-In-Chief Alper Yilmaz
Director of Publications Rae Kelley
Electronic Publications Manager/Graphic Artist Matthew Austin

Photogrammetric Engineering & Remote Sensing is the official journal of the American Society for Photogrammetry and Remote Sensing. It is devoted to the exchange of ideas and information about the applications of photogrammetry, remote sensing, and geographic information systems. The technical activities of the Society are conducted through the following Technical Divisions: Geographic Information Systems, Photogrammetric Applications, Lidar, Primary Data Acquisition, Professional Practice, Remote Sensing Applications, and Unmanned Autonomous Systems. Additional information on the functioning of the Technical Divisions and the Society can be found in the Yearbook issue of *PE&RS*.

All written correspondence should be directed to the American Society for Photogrammetry and Remote Sensing, PO Box 14713, Baton Rouge, LA 70898, including general inquiries, memberships, subscriptions, business and editorial matters, changes in address, manuscripts for publication, advertising, back issues, and publications. The telephone number of the Society Headquarters is 301-493-0290; the fax number is 225-408-4422; web address is www.asprs.org.

PE&RS. *PE&RS* (ISSN0099-1112) is published monthly by the American Society for Photogrammetry and Remote Sensing, 8550 United Plaza Blvd, Suite 1001, Baton Rouge, Louisiana 70809 . Periodicals postage paid at Bethesda, Maryland and at additional mailing offices.

SUBSCRIPTION. *PE&RS* is available as an e-Subscription (single-site and multi-site licenses) and an e-Subscription with print add-on (single-site license only). PE&RS subscriptions are on a calendar-year, beginning in January and ending in December.

The rate for a single-site e-Subscription for the USA/Non-USA is $1040 USD, for Canadian* is $1092 USD.

The rate for a multi-site e-Subscription for the USA/Non-USA is $1040 USD plus $250 USD for each additional license, for Canadian* is $1092 USD plus $263 for each additional license.

The rate for e-Subscription with print add-on for the USA is $1525 USD, for Canadian* is $1612 USD, and for Non-USA is $1565 USD.

*Note: Subscription prices for Canada includes 5% of the total amount for Canada's Goods and Services Tax (GST #135123065). **PLEASE NOTE: All Subscription Agencies receive a 20.00 USD discount.**

POSTMASTER. Send address changes to PE&RS, ASPRS, PO Box 14713, Baton Rouge, LA 70898. CDN CPM #(40020812).

MEMBERSHIP. Membership is open to any person actively engaged in the practice of photogrammetry, photointerpretation, remote sensing and geographic information systems; or who by means of education or profession is interested in the application or development of these arts and sciences. Membership is for one year, with renewal based on the anniversary date of the month joined. Membership Dues include a 12-month electronic subscription to *PE&RS*. Annual Individual Membership dues are $150.00 USD and Student Membership dues are $50.00 USD. A tax of 5% for Canada's Goods and Service Tax (GST #135123065) is applied to all members residing in Canada.

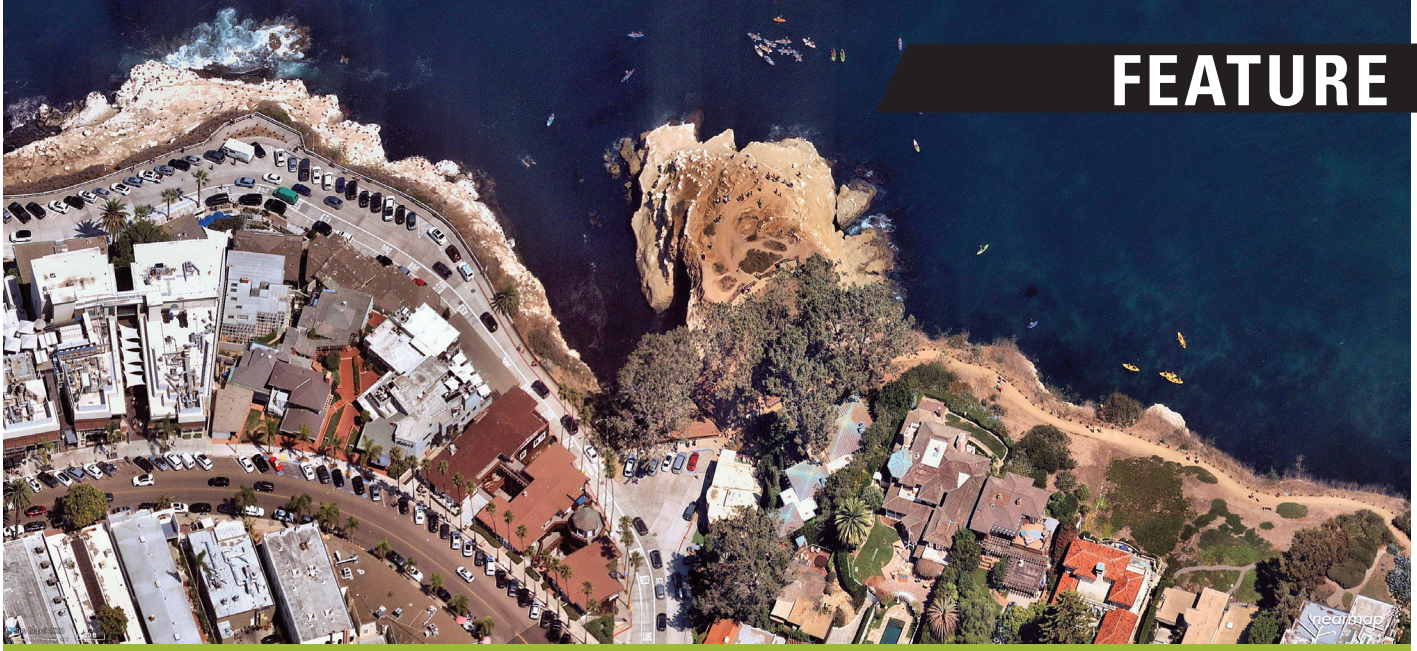

Aerial image provided by Nearmap of La Jolla, CA taken on 9/25/2021.

A Different Point-of-View
Using Aerial Imagery to Build Stronger Cities

By Shelly Carroll, Vice President and General Manager, Public Sector, Nearmap

When it comes to aerial imagery, city governments often make do with sporadically updated captures that fail to provide the most up-to-date information about the changing landscape of their urban areas. While they understand and appreciate the value of collecting this data, the update cadence is often too infrequent to reveal vital changes. As a result, information that is essential to successful planning and ongoing operations can go unrecorded and unanticipated.

This era of cities having to "make do" with self-collected aerial data may be coming to an end, thanks to new and enhanced photogrammetric products and possibilities. Increasingly, municipalities are realizing that frequently refreshed and consistent aerial imagery is a requirement if they are to keep pace with fast-growing and quickly evolving communities.

Sioux Falls Streamlines Assessments with Aerial Imagery

One recent example of this technology in action is happening in Sioux Falls, South Dakota, an Upper Midwestern city with a population of more than 200000. The most populous city in South Dakota, Sioux Falls accounts for more than 30% of the state's population.

Working with Nearmap, a leading aerial imagery and location intelligence company, Sioux Falls was able to streamline current assessment processes, leading to more accurate and easier-to-obtain data for their entire team of property assessors.

The company's premium geospatial content, combined with world-class mapping software and integrations, provided city assessors a consistent "source of truth" throughout the year. Armed with frequently refreshed images, the assessors were no longer constrained by the usual clutch of springtime image captures. Now they were able to review and assess based on late-season captures, as well, a time when many constructions projects near completion.

All data was openly accessible to anyone in the assessor's department with cloud-based access, allowing staffers to instantly stream imagery across devices. Easy integrations with CAD and GIS applications like Esri ArcGIS Pro were also essential for decision-makers from every municipal area, from public works employees to elected officials. The Sioux Falls team especially appreciated the ability to view current and historical imagery side-by-side, which is a feature of the Nearmap system that augments long-range planning activities.

City staff found that Nearmap's 3D Textured Mesh, a fully textured and colorized model, provided an enhanced understanding of actual conditions, which contributed to better informed decisions. Lauri Sohl, Civic Analytics Manager for the City of Sioux Falls, says, "While 3D urban models of proposed buildings are useful, combining them with Nearmap Textured Mesh gives people a true understanding of a project."

Photogrammetric Engineering & Remote Sensing
Vol. 89, No. 1, January 2023, pp. 5-8.
0099-1112/22/5-8

doi: 10.14358/PERS.89.1.5

Aerial image provided by Nearmap of Sun Lakes, AZ taken on 5/23/22

Breaking Down Silos for Smarter Cities

Many cities are finding that frequently updated imagery can break through existing departmental silos and support more efficient planning and operations throughout City Hall and beyond. Instead of relying on often-costly and inefficient bespoke aerial acquisitions, local governments are making the move to aerial capture programs, like the one in place in Sioux Falls. This way, users receive frequently refreshed high-resolution imagery and derived datasets that help them understand change at scale. Here's how municipal departments use these images:

- **Assessors** are able to conveniently and accurately inspect land, building structures, ground surfaces, and other taxable items for correct property valuations. They are able to remotely inspect parcels to identify new taxable activity and successfully defend against appeals.
- **Inspectors** rely on date-stamped aerial imagery to identify properties on which to focus attention. This reduces wasted trips to sites where, for example, construction has not yet begun or has slowed down mid-project.
- **Emergencies** require products like Nearmap's rapid ImpactResponse flights for the latest high-resolution basemaps to safely route police, fire, and response teams. Current aerial imagery is critical for coordinating actions on the ground, providing emergency staff a Common Operating Picture critical to developing strategy and coordinating tactics. And once the immediate danger of an emergency is over, teams can use the data to assess roof repairs, street blockages and other damage, accelerating the insurance claim process.
- **Transportation and road crews** can view even the smallest pavement irregularities – including potholes – with high-resolution, up-to-date aerial imagery. They can keep track of vegetation removal and planting projects, repairs, and they benefit from a bird's eye view of conditions as the seasons change. Officials can also use the imagery and 3D data to expand visibility into the material condition of assets like roads, vehicle depots, stations, rail tracks, bridges, pavement markings, and signage.
- **Public works, parks and recreation and environmental services** teams are able to work together seamlessly with a clear, current and consistent source of truth. For example, aerial imagery and derived datasets enable measurement and assessment of trees and greenspaces over time. For areas under water restrictions, officials can identify and monitor areas of concern that may indicate unauthorized use of scarce water resources.
- **Water, electricity, waste, and environmental utilities** use high-resolution aerial basemaps to track infrastructure, deploy crews efficiently, and respond quickly to interruptions. Large utility inventories can be quickly tracked through feature extraction and measurement of assets like electric distribution lines and poles, manholes, and water features. Potential risks to power lines or other vulnerable infrastructure from vegetation can be highlighted through historical image reviews.
- **City council, mayor, and other elected officials** value the presentation of planning materials that use GIS-integrated, high resolution recent aerial imagery to showcase environmental, social, and governance (ESG) trends. Policy development may be malinformed without the insights of location-based intelligence. And the common vision provided by recent aerial imagery is critical to a successful public input process.
- **Residents** are likely to be more engaged when better equipped with information that is easy to access and understand. Updates about the progress of road construction, new sidewalks, or park improvements can make planning their days easier. Cities are finding that communicating more accurate projections about projects helps gain public acceptance and green-light planned future efforts.

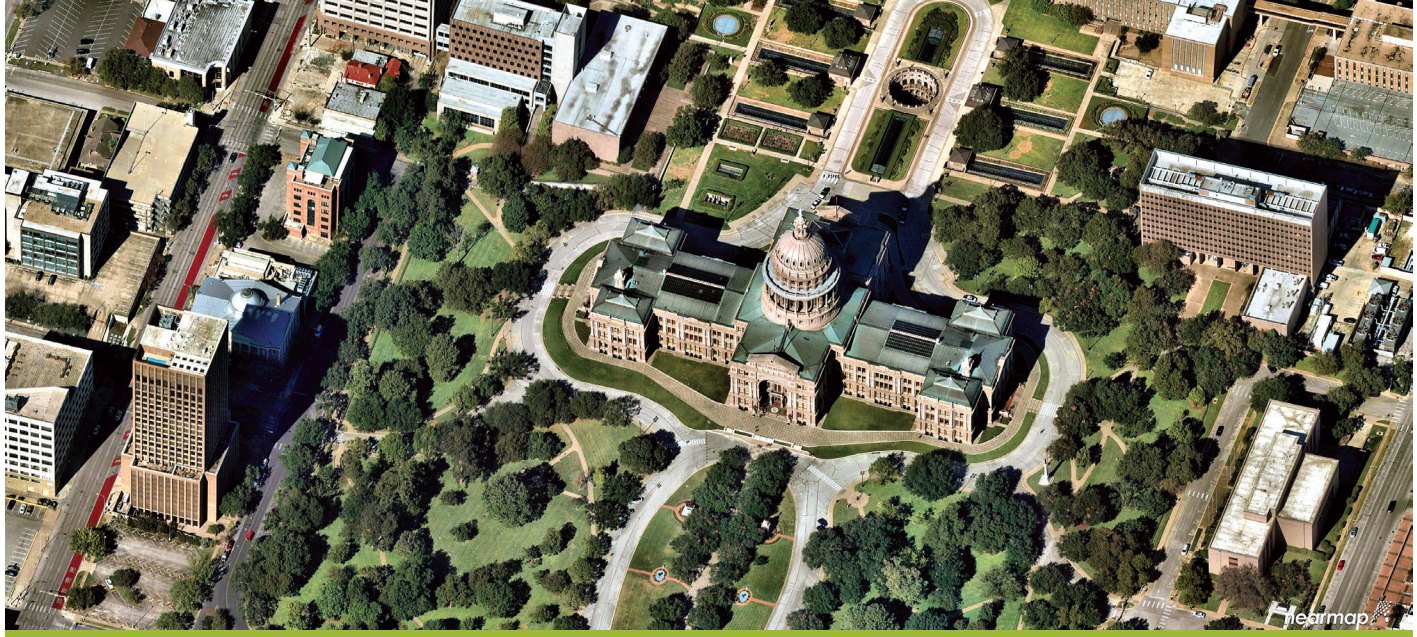

Aerial image provided by Nearmap of the Texas State Capitol taken on 10/30/2021.

How it Works

Nearmap proactively acquires and processes aerial imagery and positional data, providing subscription-based access to an ever-growing library of geospatial content. Over 80% of the U.S. parcel base is captured annually at a frequency of up to three times per year. The Nearmap ImpactResponse Program focuses on areas of natural disaster, prepositioning resources and acquiring imagery immediately following flood, wind, fire, and other events. Rounding out the acquisition offerings is the NearmapNow Program, which allows customers to obtain custom flights. In 2022, these three programs captured data for over 1.7 million square kilometers across North America.

Nearmap has built and owns its entire technology stack, from sensing systems to processing pipelines through delivery solutions. This patented digital "ecosystem" optimizes the quality, consistency, and speed of deliverables while minimizing the operational risk associated with capturing petabytes of data globally.

HyperCamera 2, the current generation of camera system, captures vertical imagery at a Ground Sample Distance (GSD) of 5.5cm (2.2") and horizontal accuracy of 19.8cm (7.8"). Oblique imagery and positional data are acquired concurrently. A full compliment of 3D content and Artificial-Intelligence (AI)-derived data layers result from each capture: textured mesh, Digital Surface Models (DSMs), point clouds,

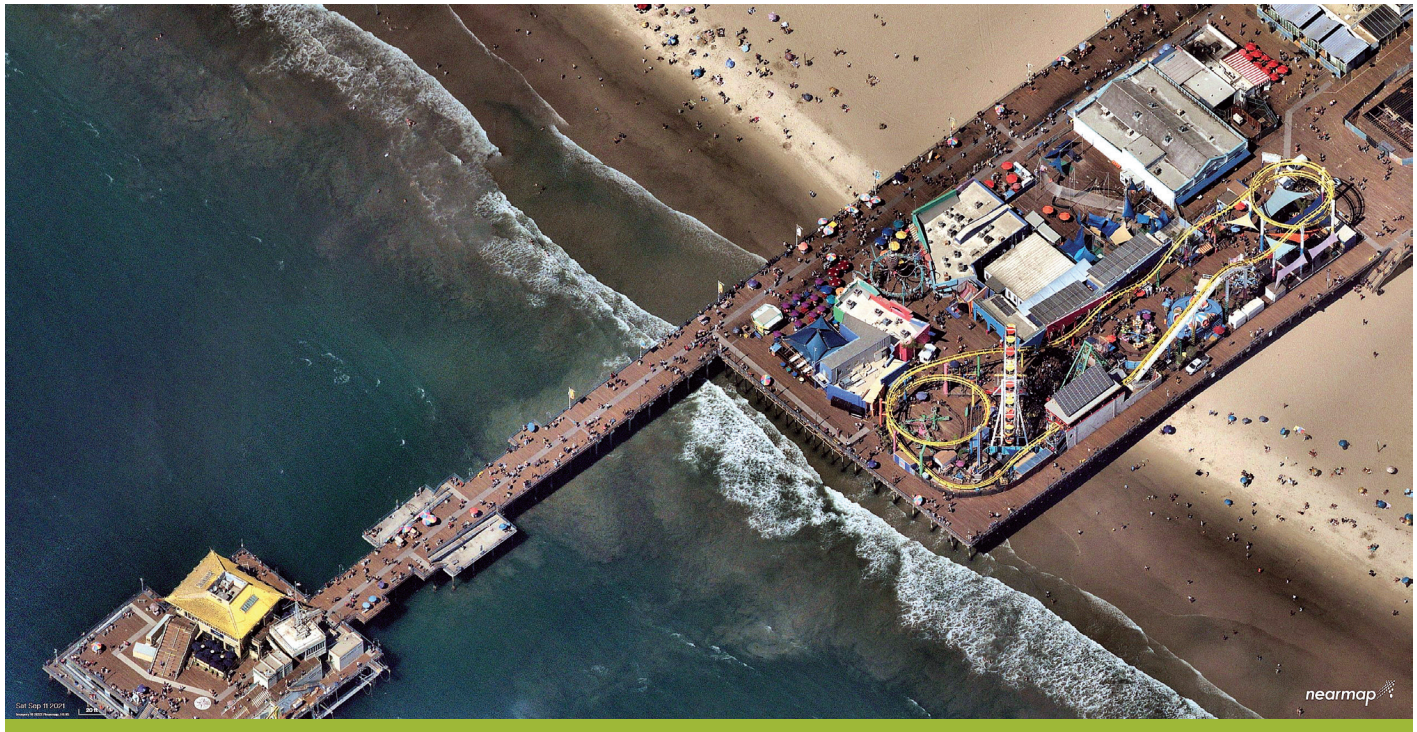

Aerial image provided by Nearmap of Santa Monica Pier, CA taken on 9/11/2021.

Aerial image provided by Nearmap of Red River Showdown in TX, taken on 10/9/2021.

and over 75 thematic vector datasets. HyperCamera 3 will debut in spring of 2023, with technological advances that significantly enhance spatial and spectral resolution, as well as the processed deliverables.

Nearmap's cloud-based photogrammetry pipeline generates these products for streamed access to customers within days of capture. Integration with GIS, CAD, Asset Management, and other decision support systems is seamless, enriching their content and context. The imagery, 3D, and AI content serves as source of truth to power a government's common operating picture (COP), allowing cities to maximize the value of all their location intelligence assets.

City Officials Weigh In

For cities that have made the move to frequently captured high-quality aerial imagery, the improvement is notable. They have been able to embrace change and build a more sustainable future by relying on the more current geospatial information.

For Trisha Favulli, Director of Assessing for Falmouth, Massachusetts, the move to more frequent aerial data has allowed her town to get ahead of a serious assessment backlog. "Before Nearmap, we were already two years behind on our imagery capture through our county commission. With Nearmap, my view has never been clearer or more up-to-date."

Timothy Zimmer, the GIS Administrator for Shelby County 911 in the Memphis metropolitan area, is impressed with the overall improvement of the accuracy of the information he can now access any time, from any connected device. "I really like how Nearmap is integrated into the GIS stack," he says. "We are able to stay on top of new developments, roads, and addresses. And being able to have Nearmap imagery integrated into our GIS systems helps us to be much more accurate."

The frequency of information updates has made a difference for Matthew W. Bradbury, GIS Administrator for the City of Redlands, California. "Nearmap affords us the ability of a bird's-eye view of our city not just once a year, but several times per year, at a resolution that is rarely obtainable within our budget," he says.

The Future is Now

Cities of the past often operated within clearly defined departmental silos that limited knowledge-sharing and mutually beneficial planning opportunities. Street crews might dig up and resurface a major road, unaware that the water utility teams had a pipe-replacement project planned for the area six months later. The street closures required for a city festival might not be effectively communicated to traffic, public works, or sanitation crews. And citizens might feel confused about the purpose and status of city improvement projects, or blindsided by changes proposed for their neighborhood.

Today, cities supported by frequently updated imagery are able to operate with a more data-driven mindset. High resolution imagery and derived data encourage a Common Operating Picture, from which everyone can share knowledge, and in which cities can grow and thrive, fueled by an understanding of the history and the changes within their boundaries.

About the Author

Shelly Carroll, shelly.carroll@nearmap.com, is the Vice President and General Manager, Public Sector of Nearmap. She has served the geospatial profession for over 25 years in both the public and private sector. Her expertise includes planning, emergency response, and resiliency. She holds the accreditation in Agile Certified Practitioner (ACP), Certified Business Analyst Professional (CBAP), Project Management Professional (PMP). Nearmap, 10897 S River Front Pkwy, South Jordan, UT 84095.

GIS Tips & Tricks

Al Karlin, Ph.D. CMS-L, GISP

When is Sharing not Sharing?

If you have been following this column, you know that I often draw my tips and tricks from student questions in my GIS class. This month's tips originate in what I thought would be a simple assignment at the beginning of the semester.

Background

My class is comprised typically of students from various backgrounds, academic-level (Sophomores through Seniors although an occasion Freshman sneaks in), and disciplines, some technical (think marine science or environmental science), some from the social sciences (think sociology or history) and some from the business school (think business management.) Most, are familiar with their personal computers, but, that computer happens to be some flavor of a MacBook running some version of MacOS X. The "gottcha" is that in the GIS laboratory, the university is running Esri-ArcGIS Pro (v2.9) on Windows 10x64 computers. So, what would appear to be a simple task for a Windows 10x64 user, turns out to be a pretty complex assignment for most of my beginning GIS students.

The Assignment

At your choice of GIS-data rich websites (I provided six URLs to websites in the state), download 3 (or more) datasets, add each to a Map Frame, symbolize each in whatever makes sense to you, construct a layer package, and upload that package the class DropBox folder (all students have access to class DropBox folders.)

After being deluged by student e-mails asking for help, here are my tips:

Tip #1 — When downloading GIS data files, the most common data exchange format is an Esri Shapefile (we actually discuss this in class and the need for four computer files.) The files; a .shp, .shx, .dbf, .prj, etc. are usually archived into a single ZIPped (.zip) file for downloading. The Esri ArcGIS Pro file browser recognizes the .zip format BUT when attempting to open a ZIPped file archive, it appears empty to the Esri file browser. The ZIPped archive must be unzipped using the Windows Operating System (or a dedicated, third-party software program) before ArcGIS can read the files and construct a layer. Of course, unZIPping a file is as easy as clicking on the file and selecting the "Extract All" function on the Windows 10 ribbon. Functionality not commonly used in the MacOS environment.

Tip#2—Adding a shapefile to a Map Frame is as easy as selecting the .shp file from a Windows file browser (left-clicking on it) and dragging (holding down the left mouse-button) the selected file onto the Map Frame.

However, quickly looking at the Windows File Browser will show two .shp files as shown in Figure 1. Careful inspection reveals that one is a SHP file while the other is an XML Document Selecting and dragging the XML Document file (immediately below the SHP file in Figure 1) onto a Map Frame will result in an "Add data" error (Figure 2.)

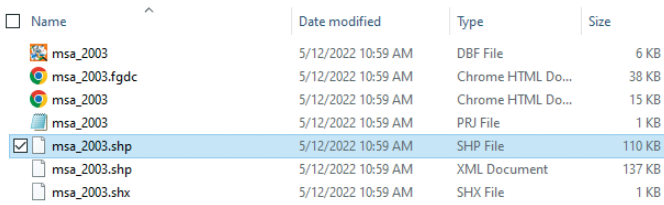

Figure 1. The SHP file for this GIS dataset is highlighted. It can be selected and dragged onto an ArcGIS Pro Map Frame. Dragging the XML Document file, also with the .shp extension, as shown immediately below the highlighted file, onto the Map Frame will result in an error (Figure 2.)

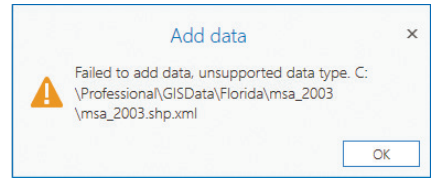

Figure 2. This error will result when the XML Document file is selected and dragged onto an ArcGIS Pro Map Frame.

Alternatively, you can attach to a folder in either Catalog or the Map Frame (Insert | Add Folder) and navigate through the ArcGIS Pro file browser interface. Again, navigation through a file structure is not common in the MacOS environment. (Note: If the feature classes are already contained in a GeoDatabase, then just dragging the feature class onto the Map Frame adds it to the Contents pane.)

Photogrammetric Engineering & Remote Sensing
Vol. 89, No. 1, January 2023, pp. 9-11.
0099-1112/22/9-11

doi: 10.14358/PERS.89.1.9

Tip #3 — Creating a Group is as easy as selecting the all the desired layers (holding the <CTRL> down and left clicking on the layers) in the Contents Pane and then right-clicking and selecting "Group" from the options menu (Figure 3.)

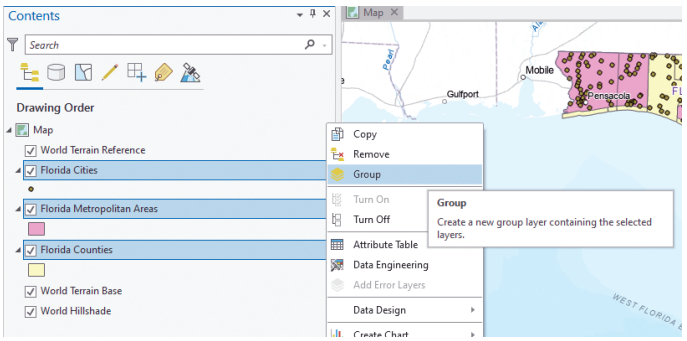

Figure 3. Selecting multiple layers in the Contents Pane and constructing a Group Layer.

Alternatively, Selecting the Map in the Contents Frame, and right-clicking activates the options menu where you can select "New Group Layer". In either case, name the New Group Layer and drag the layers into the group as needed. Another function not found in the MacOS environment.

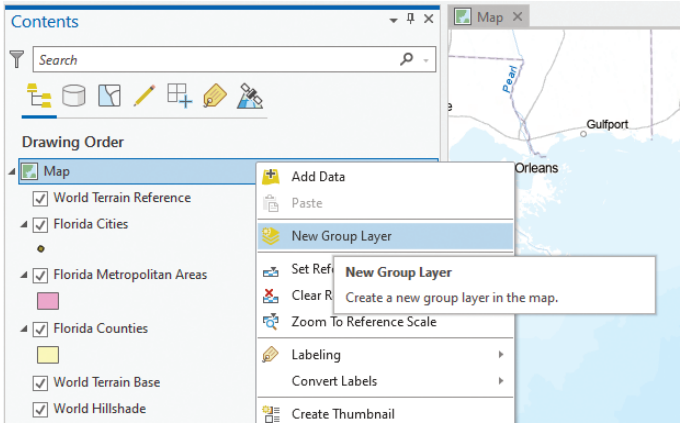

Figure 4. Constructing an empty Group Layer from the Map options.

Tip #4 — In the Esri-world, making (and saving) a Layer Package is called "Sharing". This was a source of endless confusion, as I told the students to make, save the package, and send it to our DropBox for me to review. Most were trying to "save" something, but they did not know what (or how) to save.

Right-clicking on the Group Layer presents several options including the "Share As Layer Package" as in Figure 5.

Selecting the "Share As a Layer Package" will start the "Sharing As A Layer Package" wizard (Figure 6). In the Start Packaging section, make sure to select the "Save package to file" radio button; then, in the Item Details | Name field use the folder to open the file browser and navigate to a writable folder to specify an output file path and name. To prevent errors and warnings, also include a Summary and some Tags. In the Finish Packaging section, use the "Analyze" button to check the file before using the "Package" button to SHARE (=Save) the Layer Package. Of course, if there are any errors, you will need to fix them before you can Package the Layer Package.

Once everything is error-free, it may take a few moments to write the package and finally the Layer Package (Figure 7) will be ready for others to use. This file can be sent to other ArcGIS Pro users for inclusion in their maps. It contains the GIS data, as well as, assigned symbology.

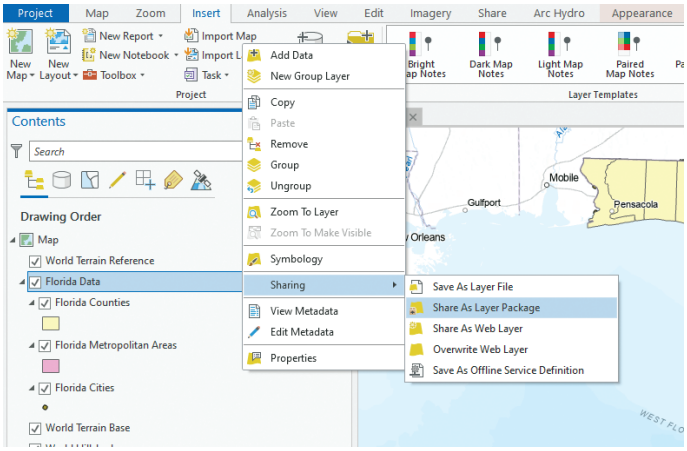

Figure 5. The options menu for a Group Layer shows the "Sharing" options. There is no "save" choice on the options menu.

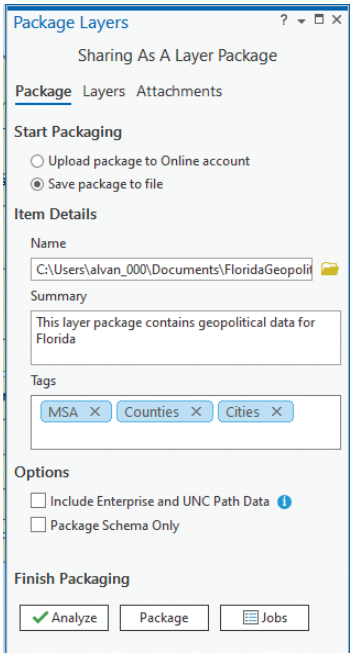

Figure 6. The Package Layers | Sharing as a Layer Package wizard. If wanting to "save" the Layer Package, it is necessary to activate the "Save Package to File" radio button.

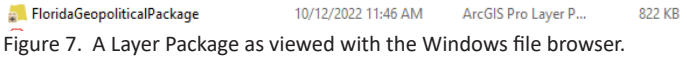

Figure 7. A Layer Package as viewed with the Windows file browser.

For those of you who use QGIS, similar functionality can be achieved using the following workflow:

1. Symbolize the layers in the QGIS Layers Pane,
2. Select the desired layers (left-click while holding down the <CTRL> Key),
3. Right-click in the Layers Pane to activate the options and choose "Group Selected" as in Figure 8,
4. Rename the Group Layer,
5. Select and Export the Group Layer | Save as Layer Definition File. This will start a file browser; browse to a writable directory and write the .qlr file.

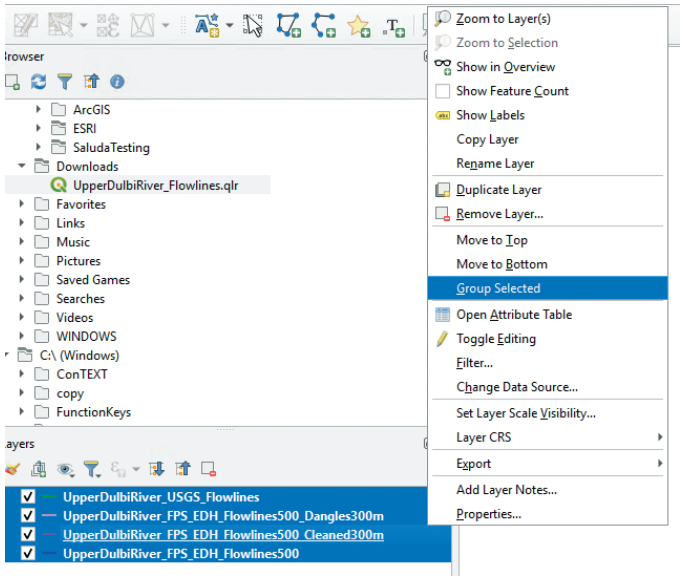

Figure 8. Selecting four layers in the QGIS Layer Pane for grouping.

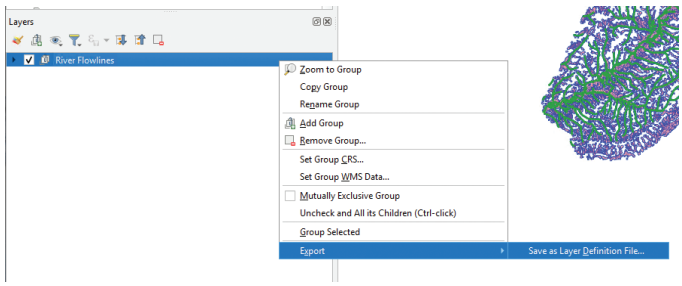

Figure 9. Exporting (saving) the Grouped Layers as a Layer Definition File in QGIS.

As with the Esri-derived layer package (.lpkx) file, this QGIS-derived layer package (.qlr) file contains the geometry, symbology and can be ported into another QGIS map frame. It is important to note that these files are NOT interchangeable; ArcGIS Pro cannot draw the QGIS layer package and vice versa.

Send your questions, comments, and tips to GISTT@ASPRS.org.

Al Karlin, Ph.D., CMS-L, GISP is with Dewberry's Geospatial and Technology Services group in Tampa, FL. As a senior geospatial scientist, Al works with all aspects of Lidar, remote sensing, photogrammetry, and GIS-related projects. He also teaches beginning map making at the University of Tampa.

ASPRS GeoByte

Allen Coral Atlas: A New Technology for Coral Reef Conservation

September 23rd at 12 Noon ET

Presenter: Brianna Bambic, *Arizona State University*

Coral reef managers and decision makers at multiple scales need information, in near real time, to react to the increasing threats facing reefs. However, more than three quarters of the world's coral reefs have never been mapped and lack monitoring. To address this knowledge gap and to support, inform, and inspire critical actions to manage and protect coral reefs, the Allen Coral Atlas combines high resolution satellite imagery, machine learning, and field data to produce globally consistent benthic and geomorphic maps and monitoring systems of the world's coral reefs. The initiative's goal is to help stakeholders ranging from local communities to regional and national governments reach their conservation targets and improve their coastal resilience. The multi-disciplinary partnership is led by Arizona State University, in collaboration with Planet, University of Queensland, and the Coral Reef Alliance.

Baseline maps have multiple uses, including: sustainable coastal development, site selection of marine protected areas, planning of restoration activities, and reef fisheries management. In this presentation, we will demonstrate how the Allen Coral Atlas supports data-driven management, conservation, and restoration of coral reefs at local, national, regional, and global scales. We have developed online courses to facilitate increased use and impact of the Atlas, and are collaborating with networks of individuals and institutions who can be alerted when changes are detected (e.g., large-scale bleaching or sedimentation events).

Brianna Bambic leads the Allen Coral Atlas Field Engagement team at the Arizona State University. With a coral reef biology and resource management background, she was an Independent Researcher for 7 years that culminated in a virtual reality experience of Half Moon Caye National Monument, Belize with a National Geographic Explorer Grant, helping communicate science to the public. Brianna received her MS in natural resource management from the University of Akureyri, Iceland in 2019. Her expertise includes coastal and marine management, global science communication, and developing capacity around remote sensing and mapping. With countless hours underwater and >700 logged dives, she loves spending time exploring the ocean..

To register, visit
https://www.asprs.org/geobytes.html

STAND OUT FROM THE REST

EARN ASPRS CERTIFICATION

ASPRS congratulates these recently Certified and Re-certified individuals:

CERTIFIED LIDAR TECHNOLOGIST

Christina Gray, Certification #LT076
Effective October 26, 2022, expires October 26, 2025

Thomas Rokita, Certification #LT077
Effective September 14, 2022, expires September 14, 2025

CERTIFIED MAPPING SCIENTIST GIS/LIS

Gabriel Ladd, Certification #GS313
Effective November 2, 2022, expires November 2, 2027

CERTIFIED MAPPING SCIENTIST – REMOTE SENSING

Su Zhang, Certification #RS240
Effective October 20, 2022, expires October 20, 2027

Gabriel Ladd, Certification #RS241
Effective November 1, 2022, expires November 1, 2027

CERTIFIED PHOTOGRAMMETRIST

Gabriel Ladd, Certification #CP1670
Effective October 26, 2022, expires October 26, 2027

Gregory Saunders, Certification #CP1671
Effective November 16, 2022, expires November 16, 2027

RECERTIFIED LIDAR TECHNOLOGIST

Ciaran Manning, Certification #R047LT
Effective November 7, 2022, expires November 7, 2025

Greg Jackson, Certification #R004LT
Effective February 1, 2022, expires February 1, 2025

RECERTIFIED PHOTOGRAMMETRIST

David Walls, Certification #R1338CP
Effective November 17, 2022, expires November 17, 2027

Mohannad Al-Durgham, Certification #R1621CP
Effective August 11, 2022, expires August 12, 2027

Douglas Lee Smith, Certification #R1090CP
Effective March 21, 2022, expires March 21, 2027

Edward Kaster, Certification #R1624CP
Effective October 10, 2022, expires October 10, 2027

Paul J. Emilius, Jr., Certification #R994CP
Effective March 1, 2022, expires March 1, 2027

Jessica S. Parsons, Certification #R1536CP
Effective November 25, 2022, expires November 25, 2027

Michael J. Lalla, Certification #R1511CP
Effective October 21, 2022, expires October 21, 2026

Timothy M. Bohn, Certification #R1207CP
Effective October 18, 2022, expires October 18, 2027

Jon Dewald, Certification #R1535CP
Effective November 18, 2022, expires November 18, 2027

Michael Rodger, Certification #R1330CP
Effective May 23, 2022, expires May 23, 2027

RECERTIFIED MAPPING SCIENTIST UAS

Cody Condron, Certification #R001UAS
Effective November 3, 2022, expires November 3, 2027

Gabriel Ladd, Certification #UAS039
Effective November 17, 2022, expires November 17, 2027

Josh Kowalski, Certification #UAS040
Effective October 19, 2022, expires October 19, 2027

RECERTIFIED MAPPING SCIENTIST REMOTE SENSING

Chuan-Shin Chong, Certification #R235RS
Effective May 19, 2022, expires May 19, 2027

RECERTIFIED MAPPING SCIENTIST GIS/LIS

Robert E. Davis, Certification #R292GS
Effective September 27, 2022, September 27, 2027

Stephen Ellis, Certification #R258GS
Effective October 19, 2022, expires October 19, 2027

RECERTIFIED MAPPING SCIENTIST UAS

Zachary Radel, Certification #R009UAS
Effective November 3, 2022, expires November 3, 2027

Stefan Claesson, Certification #R003UAS
Effective November 3, 2022, expires November 3, 2027

ASPRS Certification validates your professional practice and experience. It differentiates you from others in the profession. For more information on the ASPRS Certification program: contact **certification@asprs.org,** visit **https://www.asprs.org/general/asprs-certification-program.html.**

& Grids & Datums

Democratic Republic of the Congo

BY Clifford J. Mugnier, CP, CMS, FASPRS

The Grids & Datums column has completed an exploration of every country on the Earth. For those who did not get to enjoy this world tour the first time, *PE&RS* is reprinting prior articles from the column. This month's article on the Democratic Republic of the Congo was originally printed in 2005 but contains updates to their coordinate system since then.

The Democratic Republic of the Congo (Kinshasa), formerly called Zaire and prior to that, the Belgian Congo, lies on the equator and has borders with the Republic of Congo (Brazzaville) 2,410 km, the Central African Republic 1,577 km, Sudan 628 km, Uganda 765 km, Rwanda 217 km, Burundi 233 km, Tanzania 459 km, Zambia 1,930 km (*PE&RS*, October 2004), Angola 2,511 km (*PE&RS*, March 2001), and a small coastline on the Atlantic. The central region has an equatorial climate with high temperatures and heavy rainfall, with different climatic cycles in the northern and the southern regions. French is the offcial language, and Christianity is the majority religion. Archaeological evidence of past societies in the Congo are scanty due to the rain forest and tropical climate covering the northern half of the country and much of the Congo River Basin. Equatorial Africa has been inhabited since at least the Middle Stone Age. Late Stone Age cultures flourished in the southern savanna from approximately 10,000 *B.C.* and remained until the arrival of Bantu-speaking peoples during the first millennium *B.C.*

Comprising an area of slightly less than one-fourth of the United States, the country has a 37 km coastline with a 12 nm territorial sea. The terrain is a vast central basin on a low-lying plateau with mountains in the east. The lowest point is the Atlantic Ocean (0 m), and the highest point is Pic Marguerite on Mont Ngaliema or Mount Stanley (5,110 m).

From the Office of the Geographer, U.S. Department of State in International Boundary Study No. 127,

"Initially France established claims in the Congo

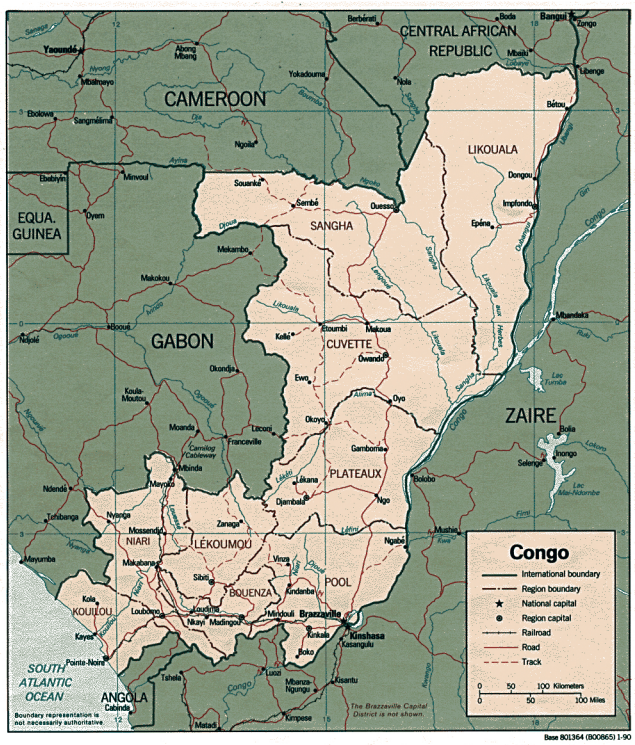

basin through penetration of the territory from bases in Gabon and by treaties with local rulers. In a series of expeditions between 1875 and 1882, Pierre Savorgnan de Brazza, an officer of the French navy, explored much of the territory between the Ogooué and Congo rivers including the Niari valley. In 1880 de Brazza negotiated a treaty with the ruler of the Teke kingdom, which secured part of the north bank of the Congo for France, but because of quiet anchorage, he constructed a station on Kintamo Island near the south bank.

During this period with an expedition from East Africa, the explorer Henry M. Stanley descended the Congo River to its mouth in 1877. King Leopold

Photogrammetric Engineering & Remote Sensing
Vol. 89, No. 1, January 2023, pp. 13-15.
0099-1112/22/13-15

doi: 10.14358/PERS.89.1.13

II of Belgium later retained his services to establish stations and to make treaties with the people of the Congo basin. In 1881 de Brazza met Stanley who was advancing eastward thorough the cataract area of the lower Congo River. Stanley arrived in the vicinity of Stanley Pool (Pool Malebo) on July 27 of the same year and founded Léopoldville on the south bank of the Congo at the site of present-day Kinshasa. Shortly thereafter, the French post on Kintamo Island was moved to the north bank of the Congo, where it became known as Brazzaville. …"

"In the meantime, King Leopold had shown great interest in the development of Africa. He invited explorers, geographers, and philanthropists of various states to a conference on central Africa at Brussels on September 12, 1876. An African International Association was organized at the conference with headquarters at Brussels. It was agreed that branches of the association in various states would be known as national committees, and King Leopold headed the Belgian National Committee.

Following the historic trip of Stanley down the Congo in 1877, King Leopold shifted his primary interests in tropical Africa from the east to the west coast. Therefore, in 1878 another committee was organized under the title of the Committee for Upper Congo Studies, which later was known as the International Association of the Congo. The association was in effect a development company with King Leopold being the principal stockholder, and Stanley was commissioned by the King for service under the International Association of the Congo. Between 1879 and 1882, Stanley established stations and made treaties with numerous African chiefs, many of which were in the upper part of the Congo basin.

Early in 1884 several states recognized the Association as a governing power on the Congo River. In an exchange of notes between France and the Association of the Congo, April-May 1884, France was accorded the right of preemption of preferential right to the region of the Congo and in the valley of Niadi-Quillou (Niara-Kouilou) should the Association of the Congo dispose of its territorial possessions.

The Berlin Conference of 1884-1885 recognized King Leopold as the sovereign head of state for the International Association of the Congo. On July 1, 1885 the name of the entity was changed to the Congo Free State, which was retained until it became a Belgian colony in 1908. A treaty for the cession of the Congo Free State to Belgium was signed at Brussels on January 9, 1895, and submitted to the Belgian Chamber of Deputies for approval shortly thereafter; however, it was withdrawn without any formal action being taken. An arrangement made between Belgium and France relative to the French right of preemption of a Belgian colony of the Congo was signed at Paris on February 5, 1895, but it was not ratified in consequence of the withdrawal of the treaty of cession. A second treaty for the cession of the Congo Free State to Belgium was signed on November 28, 1907, and approved by a Belgian Law of October 18, 1908. The treaty of cession was followed by an arrangement between Belgium and France governing the French preferential right to the Belgian Congo on December 23, 1908."

The first geodetic surveys in the Congo were part of the 1911-1914 boundary survey between Northern Rhodesia (now Zambia) and the southern Congolese province of Katanga. The fundamental (origin) point of the Katanga Triangulation is Station "A" of the Tshinsenda baseline (in Zambia) [Chain I], where: $\Phi_o = 12^o\ 20'\ 31.508''$ S and $\Lambda_o = 28^o\ 01'\ 02.465''$ E. The altitude of the point was 1,331.31 m, as determined by trigonometric leveling from the 30th Arc triangulation performed in 1912. The ellipsoid of reference used by the Belgians for the computation of the triangulation in Katanga Province was the Clarke 1866 where: a = 6,378,206.4 m, and b = 6,356,583.8 m. They also referenced the Clarke 1866 Tables as published by the U.S. Coast & Geodetic Survey. In 1954, *Comité Spécial du Katanga, Les Travaux Géodésiques du Service Géographique et Géologique* was published. The Tshinsenda Baseline [Chain I], was measured in 1912 with a length of 4,152.9912 m with the final value being adjusted with the 1923 base at Nyanza, both surveyed by the Katanga-Rhodesia Boundary Commission. The deflection of the vertical was constrained to zero at point "A." Subsequent geodetic survey connections to the Katanga triangulation by the Arc 1950 Datum provided a couple of common points. I computed the transformation from the Katanga Datum of 1912 to the Arc 1950 Datum as: ΔX = +44 m, ΔY = +46 m, ΔZ = +34 m, and I would guess that for southern Katanga these parameters are good to ±25 m. The projection adopted for the general map of Katanga was the Lambert Conical Orthomorphic with two standard parallels at $\varphi_N = 6^o\ 30'$ S and $\varphi_S = 11^o\ 30'$ S and a central meridian, $\lambda_o = 26^o$ E. However, the reason why such emphasis was placed on the province to begin with was the presence of large deposits of copper ore. With mining property values being high, a cadastral coordinate system was implemented at the same time such that a Gauss-Krüger Transverse Mercator grid was defined with a central meridian, $\lambda_o = 26^o$ E and a False Northing Latitude of Origin = 9° S and the Scale Factor at Origin = 0.9998.

The classical triangulation of Katanga required a number of baselines to be measured in order to provide a uniform reference scale to the datum. Those baselines, in addition to the 1912 Tshinsenda distance included: Kitanga

(1922) [Chain II], 3,695.0250 m, Mutene (1922)[Chain III], 1,554.9333 m, Nyanza (1923) [Chain XI], 4,881.8892 m, Kilambo (1929) [Chain VI], 6,601.2811 m, Pweto (1929) [Chain IX], 5,018.0550 m, Bululwe (1923) [Chain VIII], 10,516.9679 m, Gandajika (1947) [Chain XIII], 12,955.3016 m, and Kita Mulambo (1951) [Chain XIV], 9,187.7147 m.

An interesting "faux pas" in geodetic lore is the "Gan Datum" of the Congo. The Gandajika baseline was noticed by someone in the DMA and was confused with the Maldives Island of "Gan." As a result, the actual datum transformation for the island of Gan was incorrectly attributed to the Katanga region of Congo (Kinshasa), which has since been rectified. There is no "Gan Datum" in the Congo. I wonder what is left of the true Indian Ocean Gan Datum after the catastrophic tsunami of December 26, 2004!

The published relation between Arc 1950 Datum and WGS84 Datum in the Congo (Kinshasa) by the NGA is as follows: $\Delta X = -169$ m± 25 m, $\Delta Y = -19$m ± 25 m, $\Delta Z = -278$ m ± 25m, and this solution was based on 2 points in 1991. The current grid system used for the People's Republic of the Congo (Kinshasa) is the UTM.

Thanks to Melita Kennedy of ESRI for prodding me for answers on the legendary "Gandajika Datum," to John W. Hager for the answers on the history of the same legend, and to Mal Jones of Perth, Australia for the source material on the triangulation of Katanga. I am informed that a GPS Survey of the Congo (Kinshasa) is currently in the planning stages by private concerns.

Democratic Republic of the Congo (Kinshasa) Update

In 2009, the Kinshasa government published a law delimiting the maritime area of the Democratic Republic of the Congo. (https://www.un.org/depts/los/LEGISLATIONANDTREATIES/PDFFILES/cod_2009_law09.pdf) "On the basis, in particular, of article 9, paragraph 1, of the Constitution of 18 February 2006 which asserts the permanent sovereignty of the Democratic Republic of the Congo over its maritime areas, and on the basis of the relevant provisions of the United Nations Convention on the Law of the Sea of 1982, the present law establishes the maritime borders and enshrines the country's fundamental right to those maritime areas." The charts used for the development of the defining points are navigation charts which presumably are cast on the Normal Mercator projection, and therefore by definition the straight lines are ellipsoidal loxodromes on the WGS84 Datum.

The enumeration of the various points were computed in compliance with International Laws of the Seas (LOTS) using public-domain software written by Teledyne Geospatial. The software is called "CARIS" and is apparently available from: https://www.teledynecaris.com/en/products/easy-view/.

This column was previously published in *PE&RS*.

Look for

ASPRS Ten-Year Industry Remote Sensing Industry Forecast Highlights

in future *PE&RS* issues

- ASPRS Ten-Year Industry Remote Sensing Industry Forecast Survey continues and builds on the practice started in the late 1990s to understand the trends and directions of the industry
- ASPRS established the 10-year forecast with the civil government and its broad-based remote sensing membership
- Your remote sensing inputs are very important in shaping the future
  - To document remote sensing needs and trends
  - To drive current and future requirements and funding
- Take the survey today: **https://calval.cr.usgs.gov/apps/asprs_survey**
- Publication and online financial sponsors will be acknowledged in the publication
- Any questions, support, or sponsor requests can be provided to: **PDAD email, divisiondirectorspdad@asprs.org**

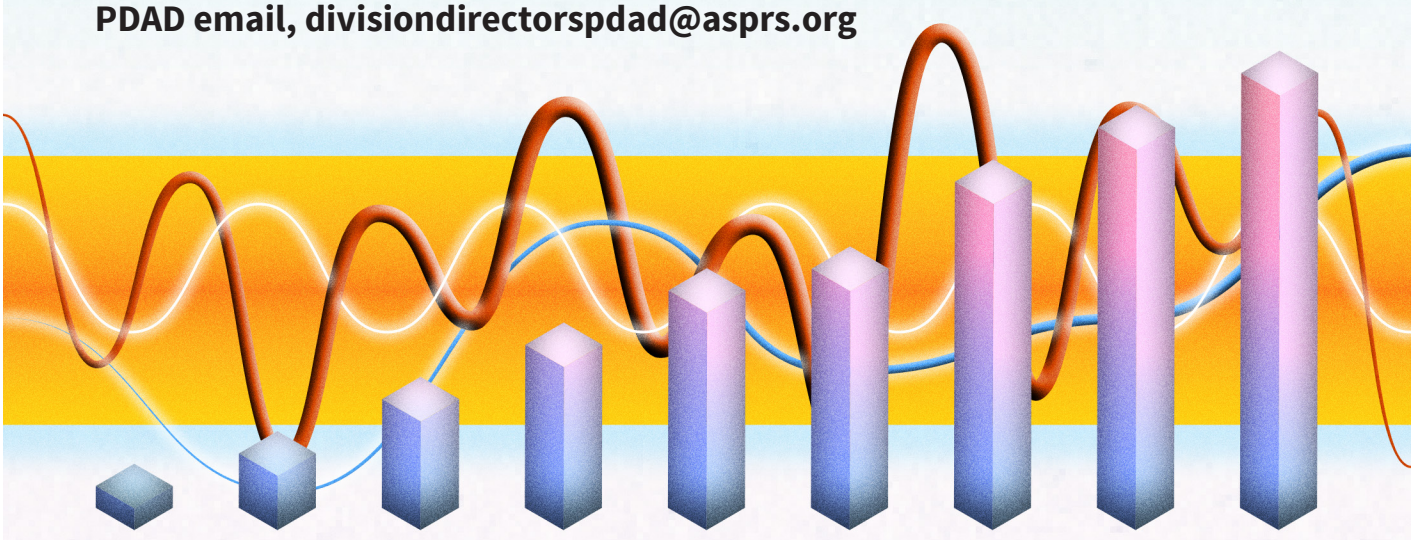

asprs THE IMAGING & GEOSPATIAL INFORMATION SOCIETY

ANNOUNCING THE 2023 ASPRS ELECTION RESULTS

Join us at the Installation of Officers on Wednesday, February 16 at 8:00 AM MST at Geo Week 2023!

Amr Abd-Elrahman,
Vice President

Matt Elious,
Assistant Director,
Professional Practice
Division

Ravi Soneja,
Assistant Director, Primary
Data Acquisition Division

Indu Jeyachandran
Assistant Director, Remote
Sensing Applications
Division

Demetrio Zourarakis,
Chair, Region Officers
Council

Hope Morgan,
Chair, Technical Division
Directors Council

Oscar Duran,
Chair, Student Advisory Council

Youssef Kaddoura,
Chair, Early-Career Professionals Council

continued on page 18

Results of the 2023 National Election

• Vice President	Amr Abd-Elrahman	
• Professional Practice Division	Matt Elious	Assistant Director
• Primary Data Acquisition Division	Ravi Soneja	Assistant Director
• Remote Sensing Applications Division	Indu Jeyachandran	Assistant Director

Results of Council Elections

• Region Officers Council	Demetrio Zourarakis	Chair
• Technical Division Directors Council	Hope Morgan	Chair
• Student Advisory Council	Oscar Duran	Chair
• Early-Career Professionals Council	Youssef Kaddoura	Chair

2023 ASPRS Board of Directors

• President	Lorraine Amenda	Term: February 2023 – February 2024
• President-Elect	Bandana Kar	Term: February 2023 – February 2024
• Vice President	Amr Abd-Elrahman	Term: February 2023 – February 2024
• Immediate Past President	Chris Parrish	Term: February 2023 – February 2024
• Student Advisory Council	Oscar Duran	Term: February 2023 – February 2024
• Early Career Professional Council	Youssef Kaddoura	Term: February 2023 – February 2024
• Committee Chairs Council	David Stolarz	Term: February 2022 – February 2024
• Sustaining Members Council	Ryan Bowe	Term: February 2022 – February 2024
• Region Officers Council	Demetrio Zourarakis	Term: February 2023 – February 2025
• Technical Division Directors Council	Hope Morgan	Term: February 2023 – February 2025
• Secretary	Harold Rempel	Appointed
• Treasurer	John McCombs	Appointed
• Executive Director	Karen Schuckman	Appointed

NEW ASPRS MEMBERS

ASPRS would like to welcome the following new members!

Babatunde Aderibigbe
Faiza Ahmed
Opeyemi Emmanuel Alabi
Gunjan Barua
Rebecca Bosworth
Emily M. Brown
Namrata Chatterjee
Janelle Chojnacki
Nathan Drew Comin
Jacob Darrah
Ellen Claudeth Delgado
Liubov Dumarevskaya
Mason Dupre
Bethany N. Ekiss
Gregory Jones Ellsworth
Prof. Peng Fu
Benjamin Hampton
Morgan Harbin
Ngozi Gloria Johnson, PhD
Timothy A. Johnston
Nivedita Priyadarshini Kamaraj
Megan Karczewski
Yunus Kaya, PhD
Minho Kim
Douglas Peter King
Matthew Kratzer
Kelly J. Kriel
David Jonathan Kuxhausen
Wenhao Liu
Ying Lu
Claudia Luna
Mark Martin
Anuska Narayanan
Prof. Uriel Perez
Scott Pieknik
Mashoukur Rahaman
Minoarimanana Ny Aina Rakotoarivony
Alexys Herleym Rodriguez Avellaneda
Batuhan Sariturk
Michael Sentman
Douglas R. Sherrill
Steve Shin
Rakibul Shogib
Hunsoo Song
Jane Southworth, PhD
Ji Won Suh
Scott Vannetta
Casey White
Mimi White
Michael Zarlengo
Jaqueline Zdebski
Adam Zyla

FOR MORE INFORMATION ON ASPRS MEMBERSHIP, VISIT
HTTP://WWW.ASPRS.ORG/JOIN-NOW

Exploring the Addition of Airborne Lidar-DEM and Derived TPI for Urban Land Cover and Land Use Classification and Mapping

Clement E. Akumu and Sam Dennis

Abstract

The classification and mapping accuracy of urban land cover and land use has always been a critical topic and several auxiliary data have been used to improve the classification accuracy. However, to the best of our knowledge, there is limited knowledge of the addition of airborne Light Detection and Ranging (lidar)-Digital Elevation Model (DEM) and Topographic Position Index (TPI) for urban land cover and land use classification and mapping. The aim of this study was to explore the addition of airborne lidar-DEM and derived TPI to reflect data of Landsat Operational Land Imager (OLI) in improving the classification accuracy of urban land cover and land use mapping. Specifically, this study explored the mapping accuracies of urban land cover and land use classifications derived using: 1) standalone Landsat OLI satellite data; 2) Landsat OLI with acquired airborne lidar-DEM; 3) Landsat OLI with TPI; and 4) Landsat OLI with airborne lidar-DEM and derived TPI. The results showed that the addition of airborne lidar-DEM and TPI yielded the best overall urban land cover and land use classification accuracy of about 88%. The findings in this study demonstrated that both lidar-DEM and TPI had a positive impact in improving urban land cover and land use classification.

Introduction

Land cover generally refers to the physical characteristics of the Earth's surface, captured in the distribution of vegetation, soil, water, and other physical features of the Earth, whereas land use is the way in which land has been used by humans and their habitat, usually with an emphasis on the functional role of land for economic activities (Liping *et al.* 2018; McConnell 2015). The understanding of urban land cover and land use is relevant to help project future change in land cover. Furthermore, it provides a pathway to understand the effects of different land management options and feedback to the environment to better manage land resources. Urban land cover and land use maps are generally used to support landscape analyses in the areas of natural and resource management, biodiversity conservation, hydrology and climate modeling, environmental protection, and urban planning (Akumu *et al.* 2018; Parent *et al.* 2015; Yu *et al.* 2014).

Urban land cover and land use information can be easily derived from airborne and satellite data. However, data from Landsat satellite series have been used in more than 40% of research publications relating to land cover classification (Yu *et al.* 2014). The spectral information of satellite remotely sensed data such as Landsat Operational Land Imager (OLI) makes it possible to extract land cover and land use information. This is because different land cover and land use types interact differently with the electromagnetic radiation from sunlight. However, because of the limitation that causes many individual, remotely sensed images to either have high spatial resolution or high spectral resolution, there is a need to explore multi-source data to improve land cover and land use classification.

With the advent and development of airborne Light Detection and Ranging (lidar) data in recent years, there is a need to explore the potential of airborne lidar products and derived topographic metrics such as Digital Elevation Model (DEM) and Topographic Position Index (TPI) in urban land cover and land use classification and mapping. Airborne lidar is a laser probing and scanning technique for bathymetric and topographic applications (Yan *et al.* 2015). It transmits pulses of laser light toward the ground using a scanner mirror. Some of this energy is scattered back towards the aircraft and recorded by the receiving unit. Onboard Global Positioning System and inertial measurement unit document the location X, Y, and elevation Z at the instant the laser pulse is sent and received. Hence, airborne lidar data provides three-dimensional records of the features on the Earth's surface. With a cloud of laser range measurements used to calculate the three-dimensional coordinates of a survey area, a DEM can be effectively generated from airborne lidar data (Sharma *et al.* 2021; Stular *et al.* 2021). Furthermore, the DEM can be used to derive topographic attributes including topographic position index by analyzing change in elevation values within a neighborhood size window. A TPI reflects the difference in elevation between a particular cell and all cells in a neighborhood window (Weiss 2001) A positive value of TPI implies the cell is higher than its surroundings, whereas a negative value infers it is lower than its surroundings. TPI values near zero imply flat areas where the slope is near zero or mid-slope areas (Jenness *et al.* 2013). Hence, TPI compares the elevation of each pixel in a digital elevation model to the mean elevation of the neighborhood and defines landform position class of each pixel. It could be used to delineate landforms such as valleys, plains, and ridges with associated land cover categories.

In recent studies, airborne lidar data have shown some potential in delineating land cover and land use information when used alone or integrated with other multispectral data (Arroyo *et al.* 2010; Im *et al.* 2008; Koetz *et al.* 2008; Miliaresis and Kokkas 2007). For example, Singh *et al.* (2012) explored the integration of airborne lidar structural and intensity surface models with Landsat Thematic Mapper (TM) in urban land cover and land use mapping. They found that the integration of canopy height and digital surface model with Landsat TM increased the total mapping accuracy by about 32% compared to standalone airborne lidar data. Likewise, the mapping accuracy increased by 8% compared to Landsat TM alone at 30 m spatial resolution. Olmanson and Bauer (2017) integrated airborne lidar-DEM with canopy height and Landsat satellite data to map and monitor land cover change between 1990 and 2010. They found about 2% increase in overall land cover classification accuracy when airborne lidar-DEM and canopy height was integrated with Landsat satellite data compared to using Landsat satellite data alone. Furthermore, Matasci *et al.* (2018) combined reflectance data from Landsat TM and Enhanced Thematic

Department of Agricultural and Environmental Sciences, College of Agriculture, Tennessee State University, Nashville, Tenn. 37209 (aclemen1@tnstate.edu).

Contributed by Petra Helmholz, May 27, 2021 (sent for review October 5 2021; reviewed by Fanar M. Abed, Yousif Mousa).

Photogrammetric Engineering & Remote Sensing
Vol. 89, No. 1, January 2023, pp. 19–26.
0099-1112/22/19–26

doi: 10.14358/PERS.21-00029R2

Mapper Plus (ETM+) with airborne lidar-derived measurements of forest vertical structure (lidar plots) to predict Canadian boreal forest cover. They found an improved prediction of forest cover when airborne lidar was integrated with Landsat derived reflectance products relative to Landsat satellite data alone.

Although, airborne lidar and satellite data have been integrated in recent land cover and land use classification, there is limited knowledge of the integration of Landsat OLI with airborne lidar-DEM and derived TPI for urban land cover and land use classification and mapping. The addition of airborne lidar-DEM and derived TPI could improve the overall detection and classification accuracy of urban land cover and land use maps. This is because land cover and land use change occur along topographic gradients and landform position (Birhane *et al.* 2019; Liu *et al.* 2020). For example, forests are commonly found upland on dry soils, whereas wetlands are formed in low lying and depressional areas with wet soils. Bare ground is commonly found on high elevation mountain tops, whereas water bodies accumulate downslopes in valleys. Therefore, there is a need to explore the addition of terrain components such as elevation and landform position in land cover classification and mapping. These could help extract different types of features on the landscape that will otherwise not detected with spectral information alone.

The aim of this study is to explore the addition of airborne lidar-DEM and derived TPI to reflectance data from Landsat OLI in improving the classification accuracy of urban land cover and land use mapping. Specifically, the urban land cover and land use classification and mapping will be performed using 1) Standalone Landsat OLI satellite data; 2) Landsat OLI with acquired airborne lidar-DEM; 3) Landsat OLI with TPI; and 4) Landsat OLI with airborne lidar-DEM and derived TPI. These four combination approaches of Airborne lidar-DEM, TPI, and Landsat OLI have been selected because they provide an opportunity to understand the independent and combined contributions of elevation and landform position in delineating land cover and land use types with spectral information.

Materials and Methods

Study Area

The study area is Davidson County, Tennessee and located around latitude 35°58′15″ to 36°22′49″ N and longitude 86°36′45″ to 86°54′43″ W. (Figure 1). It is an urban county that consists of the city Nashville and surrounding suburbs with population of about 678 889 in 2015 (United States Census Bureau 2018). Davidson County is the second largest County in Tennessee by population and among the counties in the United States with rapid growth (United States Census Bureau 2018; Sellers 2018).

Geology and Hydrology

The topography of Davidson County consists of a combination of gentle and highland terrains (Akumu *et al.* 2018; Hodges *et al.* 2018). The highlands usually have acidic soils that are heavily leached, whereas the surrounding central basin is underlain by Ordovician limestone and has alkaline soils (Mitsch *et al.* 2009). Both the gentle and highland terrains are occasionally cut across by major rivers including the Cumberland River, which flows southwards in the county (Mitsch *et al.* 2009). There are reservoirs that have been developed around the Cumberland River to manage flooding during periods of high rainfall. Many streams in the region have also been redirected to support agricultural irrigation activities (Meador 1996).

Climate

The region experiences a modest climatic condition with cool winters and warm summers (Hodges *et al.* 2018). The mean annual temperature of the area is about 78 °F (26 °C) in summer and around 41 °F (5 °C) in winter. The yearly precipitation is generally about 51 inches (1300 mm) and the precipitation is usually distributed uniformly throughout the seasons (Hodges *et al.* 2018). The month of May usually receives the maximum amount of precipitation with average of around 5.51 inches, whereas the month October receives the minimum amount of precipitation with monthly average of approximately 3.03 inches (United States Climate Data 2018).

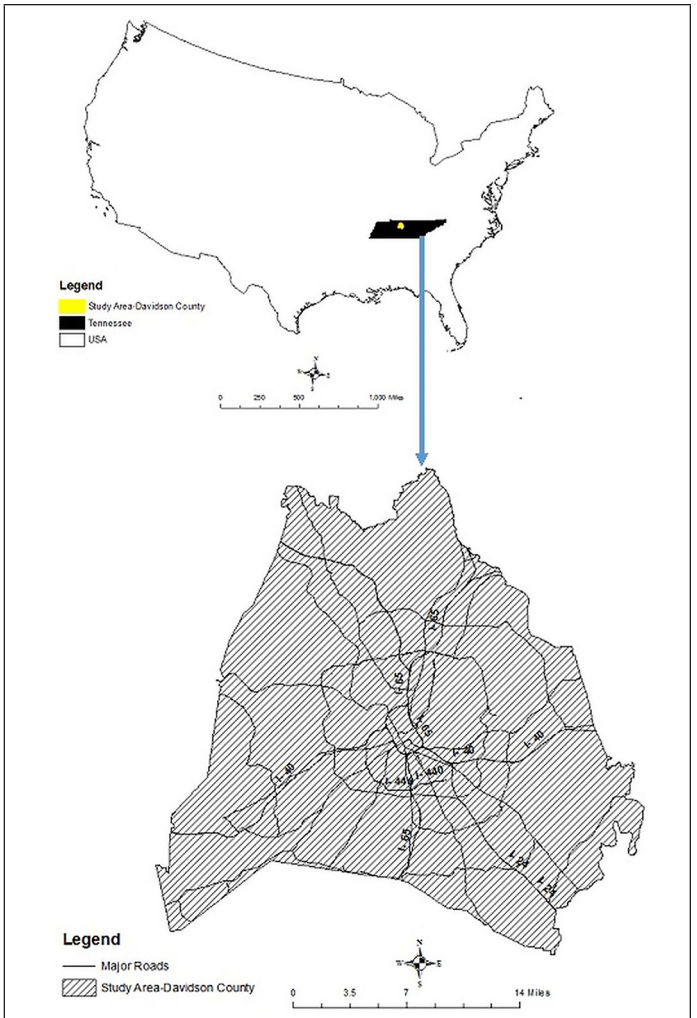

Figure 1. Study area—Davidson County in Tennessee, United States.

Methodology

The methodology involved the classification and mapping of urban land cover and land use categories using Landsat OLI satellite data alone and with addition of airborne lidar-DEM and derived TPI (Figure 2). The Landsat OLI satellite data and airborne lidar-DEM were acquired, preprocessed and used in the urban land cover and land use classification and mapping (Figure 2). The urban land cover and land use classification was performed using the following data sets: 1) standalone Landsat OLI satellite data; 2) Landsat OLI with acquired airborne lidar-DEM; 3) Landsat OLI with acquired lidar-DEM derived TPI; and 4) Landsat OLI with acquired airborne lidar-DEM and derived TPI. Validation and accuracy assessments were performed on the classified urban land cover and use maps generated from the different classification methods (Figure 2). The use of groundthruthing and Google Earth Pro information was used to validate the classified urban land cover and land use map categories.

Landsat OLI Satellite Data

A cloud-free Landsat OLI scene covering Davidson County with acquisition data of June 2016 was downloaded from the United States Geological Society Science Data repository. The cloud-free Landsat OLI scene was downloaded as a Level-1 image for preprocessing.

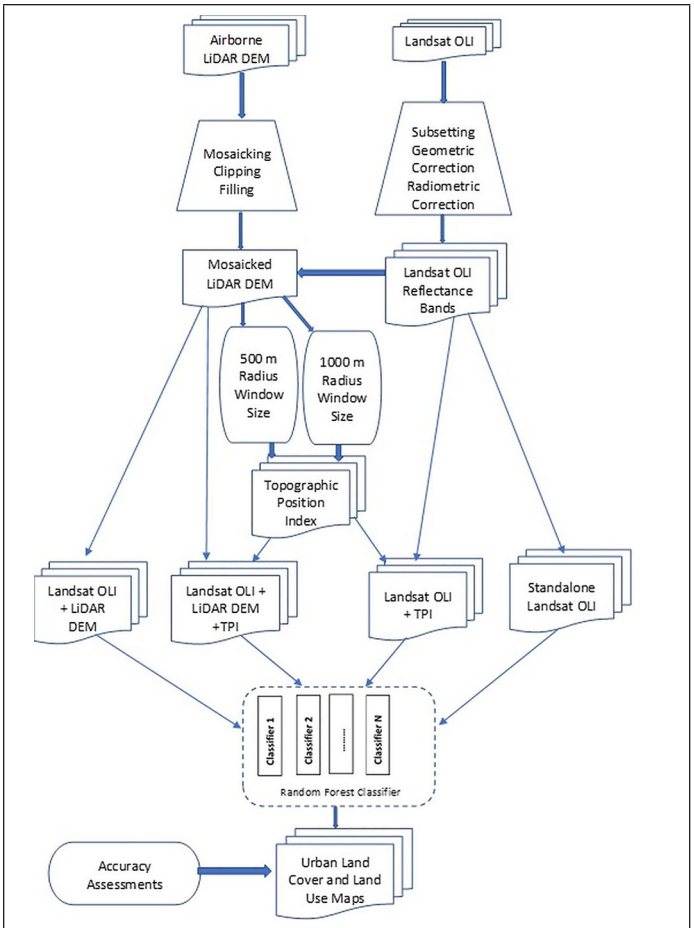

Figure 2. A schematic representation of the methodology.

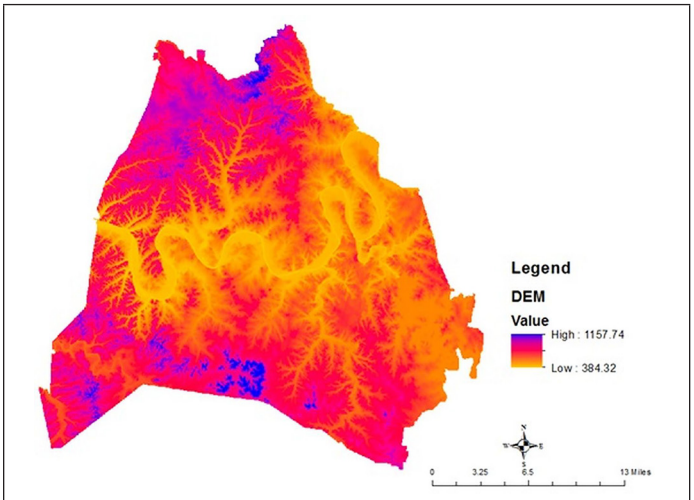

Figure 3. Mosaicked airborne Light Detection and Ranging-Digital Elevation Model (lidar-DEM) for Davidson County.

The preprocessing of the Landsat OLI satellite data involved subsetting, geometric correction, and radiometric correction. The geometric correction was carried out using greater than 50 ground control points derived from field and orthophotos with a root-mean-square value of lower than 1 pixel. The radiometric calibration was carried out by the conversion of digital number to at-surface reflectance. The Landsat OLI scene was converted from digital numbers to at-surface reflectance by using reflectance rescaling coefficients (Equation 1) derived from National Aeronautics and Space Administration (2018).

$$\rho\lambda' = M_p Q_{cal} + A_p \quad (1)$$

where:

$\rho\lambda'$ = Top of Atmosphere (TOA) planetary reflectance without correction for solar angle

M_p = Band-specific multiplicative rescaling factor (Reflectance_Mult_Band_x, where x is the band number)

A_p = Band-specific additive rescaling factor (Reflectance_Add_Band_x where x is the band number)

Q_{cal} = digital numbers

The band-specific multiplicative rescaling factor (Reflectance_Mult_Band_x), and additive rescaling factor (Reflectance_Add_Band_x) were obtained in the header file of the imagery.

Furthermore, the correction of TOA planetary reflectance for sun angle was performed using Equation 2 (National Aeronautics and Space Administration 2018).

$$\rho\lambda = \rho\lambda'/sin(\theta_{SE}) \quad (2)$$

where:

$\rho\lambda$ = TOA planetary reflectance corrected for sun angle

$\rho\lambda'$ = TOA planetary reflectance without correction for solar angle

θ_{SE} = Local sun elevation angle in degrees provided in the metadata (*Sun_Elevation*)

Airborne Lidar-DEM Data

The acquired airborne lidar-DEM data was downloaded from Tennessee Geographic Information System clearinghouse as individual tiles. The individual tiles were mosaicked, resampled to a 30 m DEM and used in this study (Figure 3). The DEM was generated from lidar point cloud data collected for Davidson County in Spring of 2016. The lidar data was collected at a nominal pulse spacing of 0.7 meter. A 2.5 ft hydro-flattened Raster DEM was created by interpolation using probable ground returns in conjunction with hydro breaklines as well as bridge breaklines.

Topographic Position Index Data

The TPI data was derived from the 30 m airborne lidar-DEM using two circular neighborhood windows. The TPI was generated using 500 m radius and 1000 m radius neighborhood windows (Figures 4 and 5). The TPI was created using two circular neighborhood sizes to explore and delineate topographic position at varied scales.

The TPI was computed using Equation 3 (Weiss 2001).

$$\text{TPI}\langle scalefactor\rangle = \text{int}((\text{dem} - \text{focalmean}(\text{dem}, \text{annulus}, irad, orad)) + 0.5 \quad (3)$$

where: *scalefactor* = outer radius in map units

irad = inner radius of annulus in cells

orad = outer radius of annulus in cells

The Landsat OLI satellite data was used as standalone data set in the classification and mapping of urban land cover and land use in Davison County. The reflectance visible and infrared spectral bands of Landsat OLI were used in the urban land cover and land use classification. Furthermore, the airborne lidar-DEM and derived 500 m radius TPI and 1000 m radius TPI were added to the reflectance Landsat OLI satellite data as separate bands and used in the urban land cover and land use classification.

Supervised classification was performed to classify urban land cover and land use in Davidson County. The supervised classification was carried out using the following data sets: 1) standalone Landsat OLI satellite data; 2) Landsat OLI with airborne lidar-DEM; 3) Landsat OLI with TPI; and 4) Landsat OLI with airborne lidar-DEM and derived TPI. Digitized polygons of urban land cover and land use categories derived from Google Earth Pro were used as training data in the supervised classification. This is because Google Earth Pro provided updated high spatial resolution images of land cover categories and digitizing capabilities for training data acquisition. The training data for each land cover and land use class used in the supervised classification had at least 50 pixels. The supervised classification was performed using a machine-learning Random Forest classification algorithm (Breiman

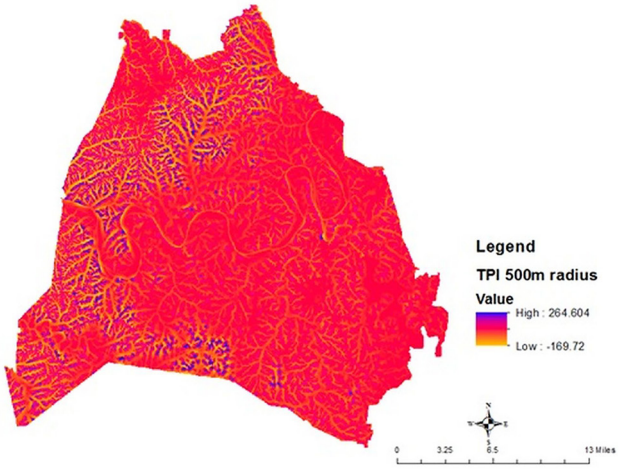

Figure 4. Topographic Position Index derived from airborne Light Detection and Ranging-Digital Elevation Model (lidar-DEM) using 500 m radius neighborhood size.

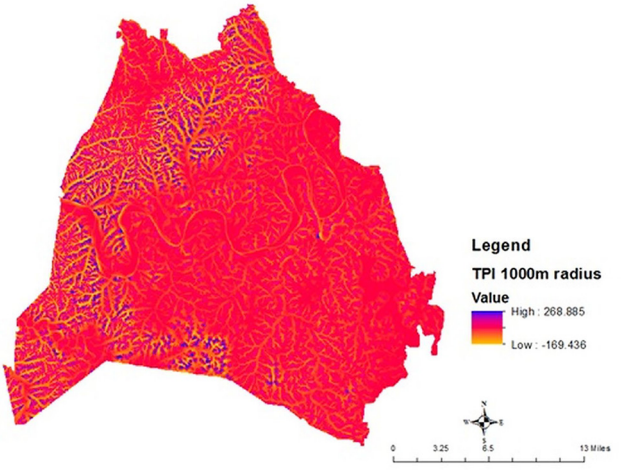

Figure 5. Topographic Position Index derived from airborne Light Detection and Ranging-Digital Elevation Model (lidar-DEM) using 1000 m radius neighborhood size.

2001). It is an ensemble classification algorithm that produces multiple decision trees using a randomly selected subset of training samples and variables (Belgiu and Dragut 2016). It is expressed using Equation 4 (Breiman 2001).

$$\{DT(x, \theta_k)\}_{k=1}^{T} \quad (4)$$

where x is the input vector, and θ_k represents a random vector, which is sampled independently but with the same distribution as the previous $\theta_k, \ldots, \theta_{k-1}$. T bootstrap samples are initially derived from the training data. A no-pruned classification and regression tree (CART) is drawn from each bootstrap sample β where only one of M randomly selected feature is chosen for the split at each node of CART (Breiman 2001; Magidi *et al.* 2021). Each of the decision tree casts a unit vote for the most popular class to classify an input vector (Breiman 1999).The number of features used at each node to generate a tree and the number of trees to be grown are two user-defined parameters that are required to generate a random forest classifier.

The number of trees and training samples in the Random Forest classification prediction model were selected through a resampling-based procedure to search for optimal tuning parameters. The optimal settings were selected based on the mean overall accuracy across five-fold cross validation, repeated twice (Costa *et al.* 2018; Sharma *et al.* 2017). The default number of training samples was set at 5000 and the number of trees was set at 10.

The urban land cover and land use classification maps generated were validated to examine how well the classified land cover and land use categories represented land cover and land use classes on the ground. The validation effort was performed by randomly selecting one thousand and two hundred (1200) polygons from each classified urban land cover and land use map and overlaying them to groundthruthing field and Google Earth data. The 1200 polygons used in validation were different from the polygons used as training data. The overall classification accuracy was computed for each classified urban land cover and land use map by dividing the total correct (i.e., the sum of the major diagonal in the error matrix table) by the total number of pixels in the error matrix table (Mather and Koch 2011). The kappa coefficient was also measured as described by Mather and Koch (2011). The urban land cover and land use classification maps were later exported into Geographic Information System for extent analyses.

Results and Discussion

The classified urban land cover and land use classes represented agriculture, bare land, developed/built-up areas, forest, grassland, shrubland, water, and wetland (Figures 6–9). The urban land cover and land use categories were successfully classified when Landsat OLI was used alone and with the addition of airborne lidar-DEM and derived TPI. The distribution of agriculture, bare land, developed/built-up areas, forest, grassland, shrubland, water, and wetland were similar when Landsat OLI was used alone and with the addition of airborne lidar-DEM and derived TPI in the classification. There was intense forest cover in the western parts of the study area relative to the eastern parts. Furthermore, the developed/built-up areas were found mostly in the central parts of the study area. In addition, there was less detection of grassland, bare land, and wetland relative to agriculture, developed/built-up, forest, and shrubland.

In the standalone Landsat OLI classification method, the area covered by agriculture was about 27 786 ha, bare land was around 3383 ha, developed/built-up area was approximately 17 974 ha, forest was about 36 818 ha, grassland was around 1944 ha, shrubland was approximately 42 062 ha, water was about 6845 ha, and wetland was around 196 ha (Table 1).

When airborne lidar-DEM was added to the classification, the area covered by agriculture was about 26 478 ha, bare land was around 3531 ha, developed/built-up area was approximately 17 697 ha, forest was about 37 068 ha, grassland was around 1967 ha, shrubland was approximately 42 299 ha, water was about 6868 ha, and wetland was around 210 ha (Table 1).

In the classification method in which Landsat OLI was integrated with TPI to classify and map urban land cover and land use categories, agriculture occupied about 28 185 ha, bare land around 2709 ha, developed/ built-up areas approximately 16 562 ha, forest about 39 788 ha, grassland around 1239 ha, shrubland approximately 41 926 ha, water about 6369 ha, and wetland around 229 ha (Table 1).

Furthermore, when acquired airborne lidar-DEM and derived TPI were added to the classification, the area of agriculture was about 26 380 ha, bare land was around 2841 ha, developed/built-up area was approximately 18 670 ha, forest was about 37 689 ha, grassland was around 2102 ha, shrubland was approximately 41 280 ha, water was about 6454 ha, and wetland was around 592 ha (Table 1). The area covered by wetland increased by about 180% when lidar-DEM and derived TPI were added to the classification relative to standalone Landsat OLI. This is possibly because wetlands are generally associated with elevation and landform positions such as flat plains and valleys. The addition of landform position and elevation data in the classification likely improved the landform characterization for wetland extraction and delineation.

The overall mapping accuracy was about 81% and kappa coefficient of 0.78 when standalone Landsat OLI satellite data set was used in the

urban land clover and land use classification (Table 2). In the urban land cover and land use classification method with standalone Landsat OLI, the user's accuracy was maximum (98%) for water and minimum (68%) for shrubland. Similarly, water had the highest (100%) producer's accuracy and wetland had the lowest (66.4%) producer's accuracy (Table 2).

When Landsat OLI was integrated with airborne lidar-DEM and used in the urban land cover and land use classification, the overall

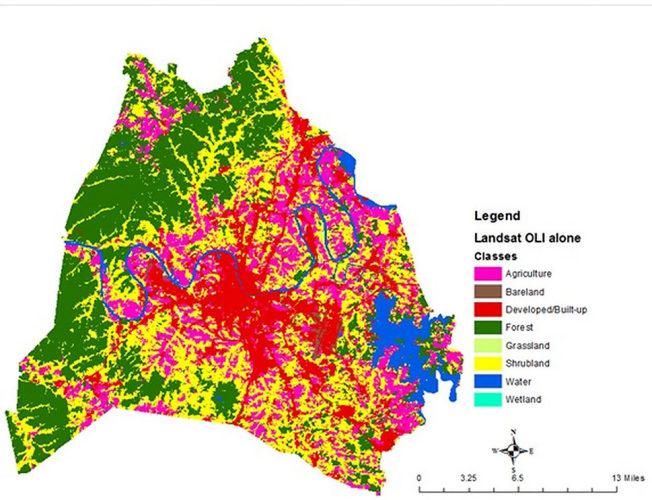

Figure 6. The urban land cover and land use classification derived from standalone Landsat Operational Land Imager (OLI) satellite data.

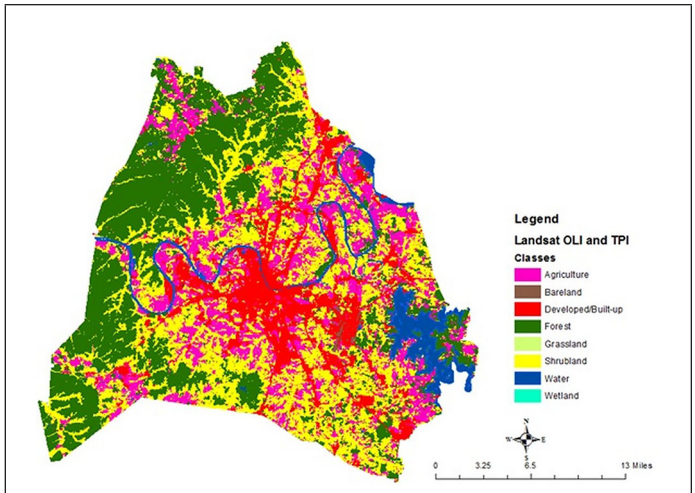

Figure 8. The urban land cover and land use classification derived from Landsat Operational Land Imager (OLI) satellite data and Topographic Position Index (TPI).

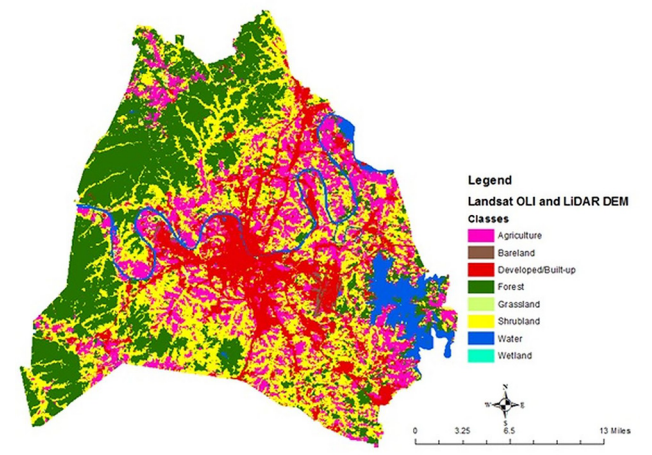

Figure 7. The urban land cover and land use classification derived from Landsat Operational Land Imager (OLI) satellite data and airborne Light Detection and Ranging-Digital Elevation Model (lidar-DEM).

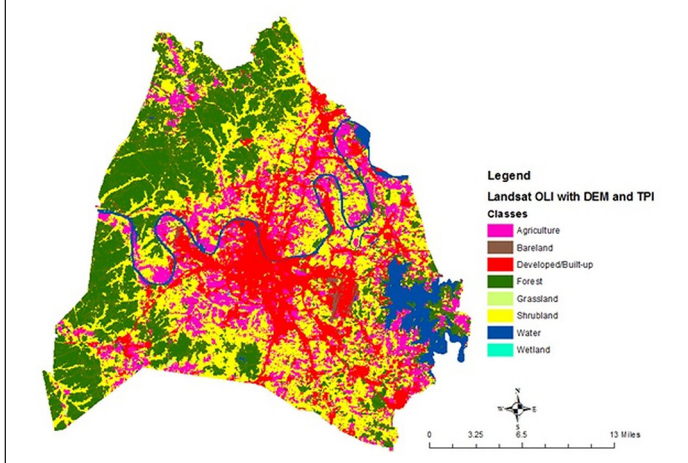

Figure 9. The urban land cover and land use classification derived from Landsat Operational Land Imager (OLI) satellite data with airborne Light Detection and Ranging-Digital Elevation Model (lidar-DEM) and derived Topographic Position Index (TPI).

Table 1. The urban land cover and land use classes and cover derived from the addition of airborne lidar-DEM and derived TPI to Landsat OLI satellite data.

	Landsat OLI Alone		**Landsat OLI and Lidar-DEM**		**Landsat OLI and TPI**		**Landsat OLI with Lidar-DEM and TPI**	
Urban Land Cover and Land Use Classes	Area Cover (ha)	% Cover	Area Cover (ha)	% Cover	Area Cover (ha)	% Cover	Area Cover (ha)	% Cover
Agriculture	27 786	20.3	26 478	19.5	28 185	20.6	26 380	19.4
Bare Land	3383	2.5	3531	2.6	2709	2.0	2841	2.1
Developed/Built-Up	17 974	13.1	17 697	13.0	16 562	12.1	18 670	13.7
Forest	36 818	26.9	37 068	27.2	39 788	29.0	37 689	27.7
Grassland	1944	1.4	1967	1.4	1239	0.9	2102	1.5
Shrubland	42 062	30.7	42 299	31.1	41 926	30.6	41 280	30.4
Water	6845	5.0	6868	5.0	6369	4.6	6454	4.7
Wetland	196	0.1	210	0.2	229	0.2	592	0.4

Lidar-DEM = Light Detection and Ranging-Digital Elevation Model; TPI = Topographic Position Index; Landsat OLI = Operational Land Imager.

mapping accuracy was around 83% and kappa coefficient was about 0.80 (Table 3). The overall mapping accuracy increased by about 2% when airborne lidar-DEM was added to Landsat OLI in the urban land cover and land use classification relative to standalone Landsat OLI. Similarly, other studies have found a stronger performance of adding DEM to Landsat satellite data in land cover and land use classification (Olmanson and Bauer 2017; Sang *et al.* 2021; Singh *et al.* 2012). The user's accuracy among land cover and land use categories in this classification method was highest (98%) for water and lowest (69%) for grassland. Likewise, the producer's accuracy was maximum (100%) for water and minimum (69.7%) for wetland. The mean user's accuracy among all urban land cover and land use categories increased by about 2% when airborne lidar-DEM was added to Landsat OLI in the classification relative to standalone Landsat OLI. Both bare land and shrubland had the maximum gain (3%) in user's accuracy whereas, and water had the minimum gain (0%) in user's accuracy. In contrast, wetland had the highest gain (3%) in producer's accuracy and water had the lowest gain in producer's accuracy when lidar-DEM was added to the classification. This implies the addition DEM data was useful to better characterize bare land and shrubland.

In the urban land cover and land use classification method in which TPI was added to Landsat OLI satellite data, the overall mapping accuracy was about 86% and kappa coefficient of approximately 0.84 (Table 4). The overall urban land cover and land use classification accuracy improved by about 6% when TPI was added to Landsat OLI reflectance scene relative to standalone Landsat OLI satellite data. The

Table 2. Error matrix table of the urban land cover and land use classification derived using standalone Landsat Operational Land Imager satellite data.

Classes	Agriculture	Bare Land	Developed/ Built-Up	Forest	Grassland	Shrub Land	Water	Wetland	Total	User's accuracy (%)	Producer's accuracy (%)	Overall accuracy (%)	Kappa
Reference													
Agriculture	174	5	0	3	6	10	0	2	200	87	83.3		
Bare Land	3	81	8	0	3	0	0	5	100	81	86.2		
Developed/ Built-Up	0	5	185	0	10	0	0	0	200	92.5	95.9		
Forest	2	0	0	148	0	40	0	10	200	74	79.1		
Grassland	22	2	0	0	69	4	0	3	100	69	71.9		
Shrubland	8	0	0	30	6	136	0	20	200	68	68.7		
Water	0	0	0	0	0	0	98	2	100	98	100.0		
Wetland	0	1	0	6	2	8	0	83	100	83	66.4		
Total	209	94	193	187	96	198	98	125	1200				
Overall and Kappa												81	0.78

Table 3. Error matrix table of the urban land cover and land use classification derived using Landsat Operational Land Imager satellite data and airborne Light Detection and Ranging-Digital Elevation Model (lidar-DEM).

Classes	Agriculture	Bare Land	Developed/ Built-Up	Forest	Grassland	Shrub Land	Water	Wetland	Total	User's accuracy (%)	Producer's accuracy (%)	Overall accuracy (%)	Kappa
Reference													
Agriculture	176	5	0	3	4	10	0	2	200	88	85.0		
Bare Land	3	84	5	0	3	0	0	5	100	84	86.6		
Developed/ Built-Up	0	5	185	0	10	0	0	0	200	92.5	97.4		
Forest	0	0	0	151	0	40	0	9	200	75.5	79.5		
Grassland	22	2	0	0	69	4	0	3	100	69	73.4		
Shrubland	6	0	0	30	6	142	0	16	200	71	70.3		
Water	0	0	0	0	0	0	98	2	100	98	100.0		
Wetland	0	1	0	6	2	6	0	85	100	85	69.7		
Total	207	97	190	190	94	202	98	122	1200				
Overall and Kappa												83	0.80

Table 4. Error matrix table of the urban land cover and land use classification derived using Landsat Operational Land Imager satellite data and TPI.

Classes	Agriculture	Bare Land	Developed/ Built-Up	Forest	Grassland	Shrub Land	Water	Wetland	Total	User's accuracy (%)	Producer's accuracy (%)	Overall accuracy (%)	Kappa
Reference													
Agriculture	179	2	0	3	4	10	0	2	200	89.5	85.2		
Bare Land	3	84	5	0	3	0	0	5	100	84	87.5		
Developed/ Built-Up	0	7	183	0	10	0	0	0	200	91.5	97.3		
Forest	0	0	0	174	0	20	0	6	200	87	85.7		
Grassland	22	2	0	0	69	4	0	3	100	69	73.4		
Shrubland	6	0	0	20	6	156	0	12	200	78	80.4		
Water	0	0	0	0	0	0	98	2	100	98	100.0		
Wetland	0	1	0	6	2	4	0	87	100	87	74.4		
Total	210	96	188	203	94	194	98	117	1200				
Overall and Kappa												86	0.84

Table 5. Error matrix table of the urban land cover and land use classification derived using Landsat OLI satellite data with airborne lidar-DEM and derived Topographic Position Index (TPI).

Classes	Agriculture	Bare Land	Developed/ Built-Up	Forest	Grassland	Shrub Land	Water	Wetland	Total	User's accuracy (%)	Producer's accuracy (%)	Overall accuracy (%)	Kappa
Reference													
Agriculture	177	2	0	3	6	10	0	2	200	88.5	86.3		
Bare Land	3	84	5	0	3	0	0	5	100	84	91.3		
Developed/ Built-Up	0	4	190	0	6	0	0	0	200	95	97.4		
Forest	0	0	0	174	0	20	0	6	200	87	86.6		
Grassland	19	2	0	0	74	2	0	3	100	74	76.3		
Shrubland	6	0	0	20	6	162	0	6	200	81	83.5		
Water	0	0	0	0	0	0	98	2	100	98	100.0		
Wetland	0	0	0	4	2	0	0	94	100	94	79.7		
Total	205	92	195	201	97	194	98	118	1200				
Overall and Kappa												88	0.86

addition of TPI successfully delineated the land cover and land use types more accurately thus making a novel contribution. This confirms the proposition in this study that the addition of TPI will likely improve the extraction of land cover and land use features. The user's accuracy in this classification method was maximum (98%) for water and minimum (69%) for grassland. Likewise, the producer's accuracy of this classification method in which TPI was added to Landsat OLI reflectance scene was highest (100%) for water and lowest (73.4%) for grassland (Table 4). The mean user's accuracy among all urban land cover and land use categories also increased by about 5% when TPI was added to Landsat OLI satellite data relative to standalone Landsat OLI. Forest had the maximum gain (13%) in user's accuracy, whereas water had the minimum gain (0%) in user's accuracy. In contrast, shrubland had the highest gain (12%) in producer's accuracy and water had the lowest gain in producer's accuracy when TPI was added to the classification. This implies the addition TPI data was useful to better characterize forest.

In the classification method in which airborne lidar-DEM and derived TPI were added to the classification, the overall urban land cover and land use classification accuracy was approximately 88% and kappa coefficient was about 0.86 (Table 5). The overall mapping accuracy of urban land cover and land use classification increased by about 9% when airborne lidar-DEM and derived TPI were added to the classification relative to standalone Landsat OLI satellite data. Similarly, the mean user's accuracy among all urban land cover and land use categories also increased by around 8% when airborne lidar-DEM and derived TPI were added to the classification relative to standalone Landsat OLI satellite data. Both forest and shrubland had the most gain (13%) in user's accuracy, whereas water had the least gain (0%) in user's accuracy. Similarly, shrubland had the maximum gain (15%) in producer's accuracy and water had the minimum gain in producer's accuracy when lidar-DEM and TPI were added to the classification. This implies the addition of lidar-DEM and TPI were useful to better characterize forest and shrubland. This classification method in which airborne lidar-DEM and derived TPI were added to the classification yielded the best overall accuracy. In contrast, the use of standalone Landsat OLI produced the weakest accuracy results of urban land cover and land use classification and mapping. The addition of elevation and landform position data from airborne lidar-DEM and derived TPI respectively helped to better classify the land cover and land use categories more accurately thus making a novel contribution. This further confirms the suggestion in this study that the addition of lidar-DEM and TPI will likely improve the detection and delineation of land cover and land use features. Compared to other studies that have examined the addition of TPI and Landsat TM in wetland mapping (Sun *et al.* 2020; Hribljan *et al.* 2017), this study has further explored the addition of DEM and TPI in mapping urban land cover and land use categories.

Although lidar-DEM and TPI contributed significantly in improving the classification of urban land cover and land use categories, these variables are inherently scale dependent. For example, this study was carried out with a resampled 30 m DEM for a several kilometers scale of Davidson County, Tennessee. In addition, the TPI was generated at 500 m radius and 1000 m radius window sizes for a several kilometers scale of Davidson County. Changes in the window sizes of TPI as well as DEM spatial resolution will likely affect the urban land cover and land use classifications. This is because for example, a flat plain detected in a small window size TPI is likely a valley in a large window size TPI. The variability in TPI window sizes, DEM spatial resolutions and their effect on land cover and land use classifications are areas of further research.

Conclusion

This study has successfully explored the addition of airborne lidar-DEM and derived TPI in urban land cover and land use classification and mapping. The urban land cover and land use categories derived from the classifications were agriculture, bare land, developed/built-up, forest, grassland, shrubland, water, and wetland. This study found that the addition of airborne lidar-DEM and derived TPI improved the overall accuracy of urban land cover and land use classification by around 6% relative to standalone Landsat OLI satellite data. This confirms the suggestion in this study that the addition of landform position and elevation related variables will likely improve the extraction and delineation of land cover and land use categories. When lidar-DEM and TPI were added to the classification, the user's accuracies of both forest and shrubland increased by about 13%, and the user's accuracy of wetland increased by around 11%. This implies the addition lidar-DEM and TPI were useful to better characterize forest, shrubland, and wetland. However, the addition of lidar-DEM and TPI were not useful to better characterize the land cover water because it had no change in user's accuracy.

Although both DEM and TPI have been found relevant in improving the classification and mapping of urban land cover and land use categories, they are characteristically scale dependent. A change in the spatial resolution of the DEM and neighborhood sizes of the TPI will likely affect the detection and mapping accuracies of the land cover and land use classifications.

However, to attain the best urban land cover and land use prediction and mapping, the addition of airborne lidar-DEM and derived TPI in the classification is relevant.

Acknowledgments

Many thanks to United States Department of Agriculture (USDA) for providing support through Evans Allen funding program.

References

Akumu, C. E., S. Dennis and C. Reddy. 2018. Land cover land use mapping and change detection analysis using geographic information system and remote sensing. *International Journal of Human Capital in Urban Management* 3(3):167–178.

Arroyo, L. A., K. Johansen, J. Armston and S. Phinn. 2010. Integration of LiDAR and QuickBird imagery for mapping riparian biophysical parameters and land cover types in Australian tropical savannas. *Forest Ecology and Management* 259(3):598–606.

Belgiu, M. and L. Dragut. 2016. Random forest in remote sensing: A review of applications and future directions. *ISPRS Journal of Photogrammetry and Remote Sensing* 114:24–31.

Birhane, E., H. Ashfare, A. A. Fenta, H. Hishe, M. A. Gebremedhin, H. G. Wahed and N. Solomon. 2019. Land use land cover changes along topographic gradients in Hugumburda national forest priority area, Northern Ethiopia. *Remote Sensing Applications: Society and Environment* 13:61–68.

Breiman, L. 1999. *Random Forests—Random Features. Technical Report 567*. Berkeley, Calif.: Statistics Department, University of California, Berkeley. <ftp://ftp.stat.berkeley.edu/pub/users/breiman>.

Breiman, L. 2001. Random forests. *Machine Learning* 45:5–32.

Costa, H., D. Almeida, F. Vala, F. Marcelino and M. Caetano. 2018. Land cover mapping from remotely sensed and auxiliary data for harmonized official statistics. *International Journal of Geo-Information* 7(157). https://doi.org/10.3390/ijgi7040157.

Hodges, J. A., R. J. Norrell and M. H. Sarah. 2018. *Tennessee.* Chicago, Ill.: Encyclopedia Britannica, Inc.

Hribljan, J. A., E. Suarez, L. Bourgeau-Chavez, S. Endres, E. A. Lilleskov, S. Chimbolema, C. Wayson, E. Serocki and R. A. Chimner. 2017. Multidate, multisensor remote sensing reveals high density of carbon-rich mountain peatlands in the paramo of Ecuador. *Global Change Biology* 23:5412–5425.

Im, J., J. R. Jensen and M. E. Hodgson. 2008. Object-based land cover classification using high-posting-density LiDAR data. *GIScience and Remote Sensing* 45(2):209–228.

Jenness, J., B. Brost and P. Beier. 2013. *Land Facet Corridor Designer.* USDA Forest Service Rocky Mountain Research Station, McIntire-Stennis Cooperative Forestry Program, Arizona Board of Forest Research.

Koetz, B., F. Morsdorf, S. van der Linden, T. Curt and B. Allgöwer. 2008. Multi-source land cover classification for forest fire management based on imaging spectrometry and LiDAR data. *Forest Ecology and Management* 256 (3):263–271.

Liping, C., S. Yujun and S. Saeed. 2018. Monitoring and predicting land use and land cover changes using remote sensing and GIS techniques—A case study of a hilly area, Jiangle, China. *PLoSONE* 13(7):e0200493.

Liu, C., W. Li, H. Zhou, H. Yan and P. Xue. 2020. Land use/land cover changes and their driving factors in the northeastern Tibetan Plateau based on geographical detectors and Google Earth engine: A case study in Gannan prefecture. *Remote Sensing* 12:3139.

Magidi, J., L. Nhamo, S. Mpandeli and T. Mabhaudhi. 2021. Application of the random forest classifier to map irrigated areas using Google Earth engine. *Remote Sensing* 13(876). https://doi.org/10.3390/rs13050876.

Matasci, G., T. Hermosilla, M. A. Wulder, J. C. White, N. C. Coops, G. W. Hobart and H.S.J. Zald. 2018. Large-area mapping of Canadian boreal forest cover, height, biomass and other structural attributes using Landsat composites and lidar plots. *Remote Sensing of Environment* 209:90–106.

Mather, P. M. and M. Koch. 2011. *Computer Processing of Remotely-Sensed Images: An Introduction.* Chichester, England: John Wiley and Sons.

McConnell, W. J. 2015. Land change: The merger of land cover and land use dynamics A2. In *International Encyclopedia of the Social & Behavioral Sciences*, edited by J. D. Wright. Oxford: Elsevier.

Meador, M. R. 1996. Tennessee wetland resources. In *National Water Summary on Wetland Resources*, edited by J. D. Fretwell, J. S. Williams, and P. J. Redman. Reston, Va.: U.S. Geological Survey Water-Supply Paper 2425.

Miliaresis, G. and N. Kokkas. 2007. Segmentation and object-based classification for the extraction of the building class from LIDAR DEMs. *Computers & Geosciences* 33(8):1076–1087.

Mitsch, W. J., J. G. Gosselink, L. Zhang and C. J. Anderson. 2009. *Wetland Ecosystems.* Hoboken, N.J.: Wiley.

National Aeronautics and Space Administration. 2018. *Landsat 8 Science Data Users Handbook.* Washington, DC: National Aeronautics and Space Administration, United States Geological Society.

Olmanson, L. G. and M. E. Bauer. 2017. Land cover classification of the Lake of the Woods/Rainy River Basin by object-based image analysis of Landsat and lidar data. *Lake and Reservoir Management* 33(4):335–346.

Parent, J. R., J. C. Volin and D. L. Civco. 2015. A fully-automated approach to land cover mapping with airborne LiDAR and high resolution multispectral imagery in a forested suburban landscape. *ISPRS Journal of Photogrammetry and Remote Sensing* 104:18–29.

Sang, X., Q. Guo, X. Wu, T. Xie, C. He, J. Zang, Y. Qiao, H. Wu and Y. Li. 2021. The effect of DEM on the land use/cover classification accuracy of Landsat OLI images. *Journal of Indian Society of Remote Sensing* 49:1507–1518.

Sellers, J. B. 2018. *Nashville is One of the Fastest Growing U.S. Cities.* Crossville, Tenn.: Crossville Chronicle.

Sharma, M., R. DevGarg, V. Badenko, A. Fedotov, L. Min and A. Yao. 2021. Potential of airborne LiDAR data for terrain parameters extraction. *Quaternary International* 575–576:317–327.

Sharma, R. C., K. Hara and H. Hirayama. 2017. A machine learning and cross-validation approach for the discrimination of vegetation physiognomic types using satellite based multispectral and multitemporal data. *Hindawi Scientific.* https://doi.org/10.1155/2017/9806479.

Singh, K. K., J. B. Vogler, D. A. Shoemaker and R. K. Meentemeyer. 2012. LiDAR-Landsat data fusion for large-area assessment of urban land cover: Balancing spatial resolution, data volume and mapping accuracy. *ISPRS Journal of Photogrammetry and Remote Sensing* 74:110–121.

Stular, B., E. Lozić and S. Eichert. 2021. Airborne LiDAR-derived digital elevation model for archaeology. *Remote Sensing* 13(9):1855.

Sun, S., Y. Zhang, Z. Song, B. Chen, Y. Zhang, W. Yuan, C. Chen, W. Chen, X. Ran and Y. Wang. 2020. Mapping coastal wetlands of the Bohai Rim at a spatial resolution of 10 m using multiple open-access satellite data and terrain indices. *Remote Sensing* 12:4114.

United States Census Bureau. 2018. *Davidson County, Tennessee.* Washington, DC: U.S. Department of Commerce.

United States Climate Data. 2018. *Climate Nashville-Tennessee.* College Park, Md.: Your Weather Service-World Climate.

Weiss, A. 2001. *Topographic Position and Landforms Analysis.* San Diego, Calif.: ESRI User Conference. <http://www.jennessent.com/arcview/TPI_Weiss_poster.htm>.

Yan, W. Y., A. Shaker and N. El-Ashmawy. 2015. Urban land cover classification using airborne LiDAR data: A review. *Remote Sensing of Environment* 158:295–310.

Yu, L., L. Liang, J. Wang, Y. Zhao, Q. Cheng, L. Hu and S. Liu. 2014. Meta-discoveries from a synthesis of satellite-based land-cover mapping research. *International Journal of Remote Sensing* 35(13):4573–4588.

A Machine Learning Method for Building Height Estimation Based on Sentinel-2 Bi-Temporal Images

Zhigang Deng, Xiwei Fan, and Jian Chen

Abstract

Building height information is essential for many applications such as urban planning and population density estimation. The building shadow length varies according to seasons, which is shown as different digital number values in multi-temporal images. Thus, the bi-temporal satellite remote sensing images of Sentinel-2 are used to estimate the buildings height in this study. An area of 15 km × 15 km in Beijing, China is taken as the study area. By preprocessing the data, the remaining pixels are split into two parts: 70% as the training data set and the rest as the testing data set. Then, one classification model and three regression models are proposed with using Random Forest (RF) method. Based on the testing data, it shows that the accuracy rate of the classification model has reached 98.4% with the kappa coefficient of 0.93. And the regression models' root-mean-square error (RMSE) is 0.61 floor for 1–6 floors group, 0.41 floor for 7–12 floor group, and 0.98 floor for above 12 floor group. The final RMSE is 1.62 floor with RF models. In general, this study shows the feasibility of using satellite mid-resolution optical image to estimate the building height and provides an important reference for regional building height estimation in the future.

Introduction

With the rapid development of urbanization, more than half of the world's population lives in cities (Manning 2011). In China, the Seventh National Census data shows that the urbanization rate of the permanent population has reached 63.89% in 2020, an increase of 14.21% from 2010. Moreover, the urbanization process of the permanent population at the developing country such as China has accelerated in the past 10 years. With the continuous progress of urbanization, the cities tend to become taller beside grow larger. Thus, we not only need to obtain two-dimensional information of the city areas, but also the three-dimensional (3D) spatial information. Apart from this, building height information is related to the urban heat island effect (Li *et al.* 2022; Wang *et al.* 2020), city climate at the local scale (Cao *et al.* 2021), population distribution at the spatial and temporal dimensions (Alahmadi *et al.* 2013; Leichtle *et al.* 2019), and so on. More importantly, it is also a key reference for urban functional zone planning and disaster emergency rescue.

Compared with the traditional field investment method, the remote sensing technology is a more efficient way to acquire building height information at large scales. To acquire buildings height based on remote sensing data, one typical group of methods is using the geometric relationship between building height and the corresponding shadow cast on ground in very-high-resolution (VHR) optical images (Cheng *et al.* 2007; Shao *et al.* 2011; Wang *et al.* 2014). However, in actual applications, those methods were restricted due to the overlapping of shadows from different buildings, and the complex shapes of the buildings, and topographic relief, etc. (Biljecki *et al.* 2017). In addition, the relatively high cost of VHR optical images is also limiting the popularization of those method. Especially for most developing countries, where buildings updated more frequently, low cost, or open access remote sensing images are more practical (Gong *et al.* 2011; Li *et al.* 2016). With the development of interferometric synthetic aperture radar (InSAR) technology, the digital surface model (DSM) data can be acquired based on satellite InSAR data. Then the building height information is extracted based on the mask algorithm on DSM (Dubois *et al.* 2016; Gamba *et al.* 2000; Stilla *et al.* 2003; Wegner *et al.* 2014). However, the noise characteristics (Stilla *et al.* 2003) and the signal is easily affected (Thiele *et al.* 2007) in InSAR technology.

In addition to the traditional visible and synthetic aperture radar (SAR) satellite remote sensing images, some new method, such as photogrammetric method based on stereo image pairs, light detection and ranging (lidar) data acquired on manned or unmanned airborne platforms were used to determine the building height and construct the 3D model of city areas. The vertical or slant view images commonly acquired by drone with a relatively high overlap rate can be used to obtain city scale 3D models based on some photogrammetric software (Martinez-Carricondo *et al.* 2020; Svennevig *et al.* 2015; Trekin *et al.* 2020). While the lidar instrument uses the principle of laser ranging to obtain the 3D coordinates, reflectivity and texture information of the building surface is used to construct the building's 3D model (Ergun 2007; Yu *et al.* 2018; Zhu and Ma 2014). Using these technical, it is possible to obtain building height information with a high accuracy, but the processing of images takes a long time, and it is difficult to reconstruct the building height at regional or global scale using airborne remote sensing data.

Apart from the data sources, with the development of machine learning technique in recent years, some Artificial Neural Networks (ANN), Random Forests (RF), and Support Vector Machines (SVM) have been widely used for building height estimation. For example, based on the dual-polarization information index in the Sentinel-1 SAR data (Torres *et al.* 2012), and Li *et al.* (2020) used the RF method to study the height of buildings at 500 m resolution in seven major cities in the United States. Further, Frantza *et al.* (2021) combined *Sentinel-1A/B* and *Sentinel-2A/B* time series to map building heights for entire Germany based on SVM and RF models. Recently, deep learning made major advances in solving problems in many domains (LeCun *et al.* 2015). In building height extraction, Cao *et al.* (2021) propose a multispectral, multi-view, and multi-task deep network (called M^3Net) for

Zhigang Deng and Xiwei Fan are with Key Laboratory of Seismic and Volcanic Hazards, China Earthquake Administration, Beijing 100029, China (Corresponding author: Fanxiwei@ies.ac.cn).

Zhigang Deng and Xiwei Fan are also with the Institute of Geology, China Earthquake Administration, Beijing 100029, China.

Zhigang Deng and Jian Chen are with the School of Engineering and Technology, China University of Geosciences Beijing, Beijing 100083, China.

Contributed by Ahmed Abd El-Latif, February 18, 2022 (sent for review July 18, 2022; reviewed by Bruno Vallet, Salman Ahmadi).

Photogrammetric Engineering & Remote Sensing
Vol. 89, No. 1, January 2023, pp. 27–36.
0099-1112/22/27–36

doi: 10.14358/PERS.22-00054R2

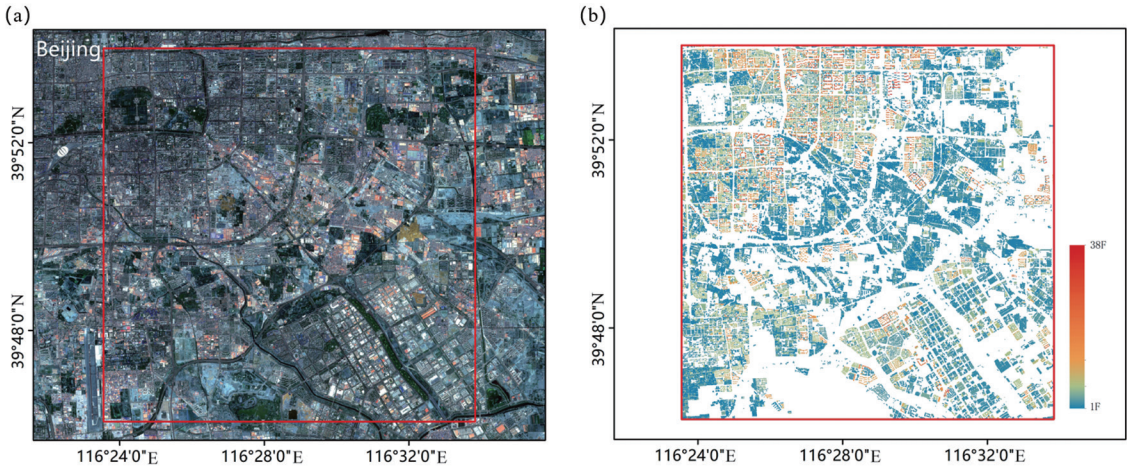

Figure 1. Red, green, blue (RGB) image of the study area (a) and corresponding building height map in spatial resolution of 10 m (b).

building height estimation, where ZY-3 multispectral and multi-view images are fused in a multi-task learning framework.

Note that the machine learning models of SVM or RF require fewer samples for model training compared with deep learning models. Considering the mid-resolution satellite images have the advantages of easier access compared with VHR images and have a globe coverage compared with local coverage of airborne data; this study tries to use RF model to estimate the building height based on the mid-resolution satellite images of *Sentinel-2*. The paper is structured as follows: In the next section, a description of the study area and data used in this study is provided. The data preprocessing and RF model construction are given in the "Method" section. The results are presented in the "Results" section. The "Discussion" section discusses the results, and the last section contains the conclusions of this study.

Study Area and Data

Study Area

Our region of interest is in the southeast of Beijing, China, covering an area of approximately 15 × 15 km^2. The study area is between 39°43′–39°54′N, 116°23′–116°34′E. The region of interest is shown in the red rectangle of Figure 1a, and the corresponding buildings' floors of the study area from reference data are shown in Figure 1b.

As the *Sentinel-2* multispectral instrument (MSI) image with a spatial resolution of 10 m is used in this study, 1460 × 1457 pixels are acquired in the study area. The study area contains all the major building structure types, such as brick and wood structure buildings with one floor, unreinforced brick and concrete structure building in multi-floors with the maximum of seven floors, and the high-raised reinforced concrete structure or steel structure buildings. As the buildings with nearly all common height range are included, this part of Beijing is selected as the study area. Figure 2 is the histogram of building height of the study area. It shows that about 89.06% of the area is covered by 1–6 floor buildings, 5.55% covered by 7–12 floor buildings, and the rest is over 12 floors. The buildings with floor number less than six account for a vast majority, which is consistent with actual conditions.

Data

Actual Building Height Data

An open access building height data of Beijing (https://data.yunshudu.com/detail.html?id=10051) is taken as reference to construct the machine learning model in this study. The height information of 297 221 buildings is saved in "shp" format. To match with the satellite images used in this study, the actual building height data in vector format is converted into raster with a spatial resolution of 10 m. Note that some of the buildings in original vector format may only occupy part of the 10 × 10m pixel area. The pixels are taken as buildings with occupy more than half of the 10 × 10 area. At the same time of conversion, the height value of the pixel used in the study are called "maximun_combined_area", which means that buildings with the largest area in the pixel determine the attributes assigned to the pixel. It can ensure that the building outlines and the determined building pixels are consistent to the greatest extent.

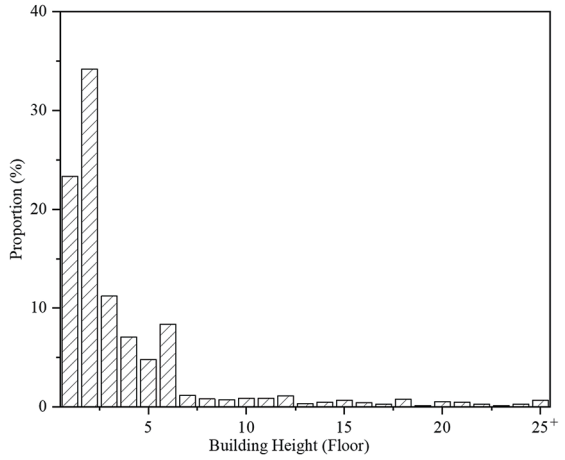

Figure 2. Histogram of building height (floor) of the study area.

After that, 708 646 pixels with the value of corresponding floors are acquired and are used for further analysis. Note that, due to the building height data used in this study are saved in floors, the raster building heights calculated based on RF model are also given in floors.

Satellite Images

Generally, there are two types of widely used open access satellite optical remote sensing images with a spatial resolution of tens of meters: Landsat/TM series and *Sentinel-2*/MSI. Considering the advantages in the revisit period, spatial and radiometric resolution of *Sentinel-2* data compared with Landsat series such as Landsat-8, the *Sentinel-2* is selected in this study.

The *Sentinel-2* constellation includes two identical satellites 2A and 2B operating in sun-synchronous orbit, with a five-day revisit period at the Equator and an even shorter time toward the poles (Drusch *et al.* 2012). *Sentinel-2* MSI has 13 bands from 0.44 μm to 2.19 μm: four visible and near-infrared (NIR) bands at 10 m, six bands at 20 m, and three bands at 60 m spatial resolutions, respectively (ESA 2015). *Sentinel-2* MSI has broad application prospects for land use and land cover classification (Wang *et al.* 2016), ground vegetation monitoring or identification (Transon *et al.* 2018), surface water information extraction (van der Meer *et al.* 2014; Xu 2007), geological disaster surveying and mapping (Lu *et al.* 2019; Lu *et al.* 2021), urban land

cover classification (Qiu *et al.* 2020a) or human settlement extent mapping (Qiu *et al.* 2020b).

To estimate the building height, two *Sentinel-2* MSI images with the acquisition dates close to winter solstice and summer solstice, respectively, and have a low cloud coverage are selected. Since the actual building height data is acquired in 2017, two *Sentinel-2* Level 1C products acquired on 4 June (L1C_T50TMK_A010182_20170604T030632) and 24 December (L1C_T50TMK_A013085_20171224T031230) in 2017 with cloud coverage less than 10% are downloaded from the ESA API Hub (https://scihub.copernicus.eu/).

Method

Theoretical Background

For the ground pixels of urban area close to buildings, the corresponding digital number (DN) values observed by remote sensors can be different in different solar zenith angles. Namely, during the summertime with a relatively higher solar zenith angle, the DN values can be larger as less shade is cast on the ground, compared with winter in a lower solar zenith angles. As the *Sentinel-2* is observing the same location at nearly the same local time in approximately vertical view condition, the DN values differences may be detected by MSI images acquired at different days of the year. Once the DN values difference is larger than the radiometric resolutions of MSI, this method can be used for buildings height extraction.

The formula shows the relationship between building height, solar zenith angle and shadow length:

$$L = H \bullet \tan(\theta) \tag{1}$$

where L is the length of the building shadow, H is the building height, and θ is the solar zenith angle. The solar zenith angle on the winter solstice (December 21st) is about 26° while 73° on the summer solstice (June 21st) for the study area. As the difference of the solar zenith angle is the largest near the winter solstice and the summer solstice, the coverage of the shadows has the largest difference, and the corresponding image DN values differs greatly. Thus, the *Sentinel-2* images close to winter solstice and summer solstice are used in this study.

To study the DN values' difference between winter and summer images, the mean, minimum, and maximum of DN values in B7 of no-vegetation pixels (based on the quality-scene-classification file after atmospheric correction) in the study area are shown in Table 1. In addition, the solar zenith and azimuth angles of the corresponding images of 4 June 2017 and 24 December 2017 are also shown in Table 1. The difference between the means of summer and winter images' DN values is approximately 860. And there are also significant differences between summer and winter images' minimum and maximum values. As there are obvious differences of DN values between winter and summer *Sentinel-2* MSI images at the same location as Table 1 shows and the MSI images are saved in 12-bit with an absolute radiometric uncertainty of about 3% (https://sentinels.copernicus.eu/web/sentinel/technical-guides/sentinel-2-msi/performance), the DN values of those two images are applied to estimate the buildings' height in this study.

Image Preprocess

As the DN values of the urban pixels in bi-temporal images of winter and summer are used to estimate the building heights, the influences of atmosphere need to be eliminated. The solar irradiance can be abstracted and scattered in the path from top of atmosphere to the ground, as well as in the reflectance path. These can significantly change the DN values. As the bi-temporal images of winter and summer may have entirely different atmosphere properties such as water vapor content and aerosols, the atmosphere correction process of MSI images is necessary.

Note that the L1C products have been orthorectified and geometrically corrected; we used the code of Sen2Cor (Mueller-Wilm 2020) to carry out atmospheric correction based on L1C to acquire the corresponding L2A product, namely the bottom-of-atmospheric reflectance products. In addition, the aerosol of thickness, water vapor, and scene classification obtained after atmospheric correction are also acquired to extract the effective pixel.

Besides the influences of aerosol, the clouds can block the ground in the satellite field of view and cast shadows on the ground. The snow can also change the DN values of actual urban land surface. Thus, based on those supplement outputs of the atmospheric correction process, all the pixels in a 130 m box with the cloud pixel as the center are deleted. This side length was chosen as a compromise to capture the most shadows (at least 80% of the building pixels are effective data) while not losing too much spatial detail. After that, 17.67% pixels of the total samples of the study area is taken as clouds, cloud shadows, ice, and snow; and all are eliminated according to the quality-scene-classification file. Namely, the rest of the 574 350 pixels are taken as available pixels and finally used for model construction.

After the L2A level data is produced, the resolution of each band of MSI needs to be unified. The six bands of 20 m resolution are resampled into 10 m with the nearest neighbor sample method. As we try to estimate the building height with a spatial resolution of 10 m, the six bands with the resolution of 60 m are not considered in this study.

Features Extraction

Spectral Indexes

Six spectral indexes are considered in this study for RF model construction: Normalized Difference Built-Up Index (NDBI) (Zha *et al.* 2003) is chosen due to its sensitivity to urban area; Normalized Difference Vegetation Index (NDVI) (Tucker 1978) and Tasseled Cap Greenness (TCG) are account for urban vegetation. The Tasseled Cap Brightness (TCB) to capture brightness gradients of roofing materials, the modified Normalized Difference Water Index (mNDWI) (Xu 2007) and the Tasseled Cap Wetness (TCW) (Crist 1985; Shi and Xu 2019) are account for water intermingled within the building pixels with an area of 10 m.

Based on the 10 bands of MSI with a spatial resolution of 10 m after a resample, those six spectral indexes are calculated according to Table 2. After combing the MSI 10 bands and six spectral indexes based on the bi-temporal winter and summer images, we can get a collection of 32 ((10 + 6) · 2) spectral-temporal features for the model construction.

Mathematical Morphology Indexes

Mathematical morphology is an image analysis subject based on lattice theory and topology. It's not only the basic theory of optical image processing (Goutsias *et al.* 2000), but also a method to obtain spatial information within a certain range (Dalla Mura *et al.* 2010). By choosing the size and shape of the structural element, we can construct

Table 1. Statistical values of summer and winter *Sentinel-2* multispectral instrument (MSI) B7 images at the study area.

Imaging Time	Solar Zenith Angle	Solar Azimuth Angle	DN_{mean} Value	DN_{min} Value	DN_{max} Value
20170604	67.57°	136°	2765	963	5051
20171224	25.22°	165°	1906	576	4194

Table 2. Formulas of six spectral indexes.

Spectral Indexes	Formula
NDBI	$R_{NDBI} = (B11 - B8)/(B11 + B8)$
mNDWI	$R_{mNDWI} = (B3 - B11)/(B3 + B11)$
NDVI	$R_{NDVI} = (B8 - B4)/(B8 + B4)$
TCB	$TCB = 0.3510 \cdot B2 + 0.3813 \cdot B3 + 0.3437 \cdot B4 + 0.7196 \cdot B8 + 0.2396 \cdot B11 + 0.1949 \cdot B12$
TCG	$TCG = -0.3599 \cdot B2 - 0.3533 \cdot B3 - 0.4737 \cdot B4 + 0.6633 \cdot B8 + 0.0087 \cdot B11 - 0.2856 \cdot B12$
TCW	$TCW = 0.2578 \cdot B2 + 0.2305 \cdot B3 + 0.0883 \cdot B4 + 0.1071 \cdot B8 - 0.7611 \cdot B11 - 0.5308 \cdot B12$

NDBI = Normalized Difference Built-Up Index; mNDWI = modified Normalized Difference Water Index; NDVI = Normalized Difference Vegetation Index; TCB = Tasseled Cap Brightness; TCG = Tasseled Cap Greenness; TCW = Tasseled Cap Wetness.

morphological operations that are sensitive to specific shapes. Therefore, we computed erosion, dilation, opening, closing, morphological gradient, top hat, and black hat (Mesev 2001) using a square structuring element with a 130 m area based on the 10 bands and the six spectral indexes in bi-temporal images. After that we produces a total of 32 × 7 = 224 features.

The mathematical morphology used in this study contains four basic operations (erosion, dilation, opening, closing) and three derivative operations (morphological gradient, top hat, and black hat). These transforms for one dimensional (1D) signals are addressed as follows (Dong *et al.* 2011).

Let $f(n)$ be the original 1D discrete signal, which is the function over a domain F = (0, 1, 2, …, N – 1). And let g(n) be the SE, which is the discrete function over a domain G = (0, 1, 2, …, M – 1) (N < M). The above operations' formulas were defined in Table 3.

Table 3. Formulas of seven mathematical morphology indexes.

Morphology Indices	Formula[a]
Dilation	$(f \oplus g)(n) = \max[f(n-m) + g(m)]$
Erosion	$(f \Theta g)(n) = \min[f(n+m) - g(m)]$
Opening	$(f \circ g)(n) = (f \Theta g \oplus g)(n)$
Closing	$(f \bullet g)(n) = (f \oplus g \Theta g)(n)$
Morphological Gradient	$MG(f(n)) = (f \oplus g)(n) - (f \Theta g)(n)$
Top Hat	$TH(f(n)) = f(n) - (f \circ g)(n)$
Black Hat	$BH(f(n)) = (f \bullet g)(n) - (f \circ g)(n)$

[a] $\oplus$, Θ, $\circ$ and $\bullet$ denote the operators for dilation, erosion, opening, and closing, respectively.

Gray Level Co-Occurrence Matrix

Gray level co-occurrence matrix (GLCM) refers to a common method of describing image texture by studying the spatial correlation characteristics of gray (Haralick 1973). To be consistent with calculation of the morphological features, the window size of 130 m is also considered in the GLCM calculation. In addition, the offset includes four directions (0°, 45°, 90°, 135°) with an offset of *D*. The following eight texture features calculated based on GLCM are selected: Mean, Variance, Homogeneity, Contrast, Dissimilarity, Entropy, Angular Second Moment, and Correlation. The calculation equation of those eight features used in this study can refer to Chen and Yang (2012).

Note that, once considering all the input features of those four directions and eight texture features, there is a redundancy situation. Therefore, in the case of the same amount of data, the RF is used to choose the direction and offset with the lowest RMSE. After comparing with other values of offset and directions, it shows that the GLCM features with an offset of 1 and in the direction of 90° have a largest correlation coefficient with the building height. From the head files of *Sentinel-2* MSI, it can be seen that the solar azimuth angles are 135° and 165°, respectively, of the winter and summer images, when the *Sentinel-2* observing the study area of Beijing. Thus, the offset direction of 90° is used in this study. Therefore, the eight texture feature values with the direction of 90° and offset of (–1, 0) are used in RF model construction. Therefore, the total number of features generated by this process is 32 × 8 = 256.

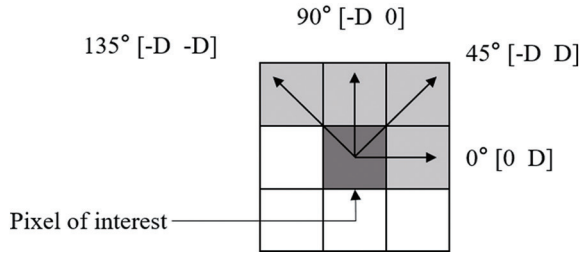

Figure 3. The theory of gray level co-occurrence matrix.

Effects of Different Input Features

As mentioned above, a total of 10 MSI bands and six spectral indexes were selected, and seven morphological characteristics and eight secondary statistics of GLCM were studied. With gradual increases, the types of input features in the RF model with a leaf number of 1, the corresponding Out-of-Bag (O-O-B) RMSE between predicted building floors and reference building floors with respect to the number of grown trees are shown in the Figure 4.

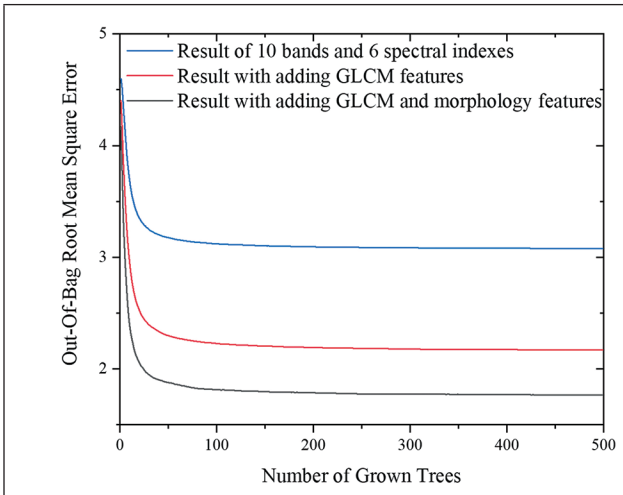

Figure 4. Out-of-Bag (O-O-B) root-mean-square error (RMSE) with respective to tree numbers using different types of input features. GLCM = gray level co-occurrence matrix.

It can be seen the RF model's RMSE is much larger than other results with only using 10 MSI bands and six spectral indexes, reaching the 3.08 floor. The reason is it only considers the building pixels and does not take into account the change characteristics within a certain range of the surrounding area. With the addition of the GLCM features, the changes of building pixels in the specific direction of the building are fully considered, so that the accuracy of the model has been greatly improved with the RMSE reduced to the 2.17 floor. Finally, the RMSE of the RF model is reduced to the 1.75 floor (without feature and parameter selection) with the combination of spectral, GLCM, and morphological features. It means that the morphological characteristics have increased the accuracy of the model and reflected the spatial characteristics of the building pixels.

Machine Learning Modeling

There are some representative machine learning methods such as RF, SVM, and ANN used for remote sensing model construction with a property accuracy. Compared with other methods, the RF model have been proven advance in recognition accuracy, stability, robustness to features, and not easily influenced by environmental noise. Furthermore, the user-friendly parameters in RF offer great convenience for practical application (Han *et al.* 2018). Thus, the machine learning model of RF is used in this study to construct the building height estimation model. It should be noted that the classification and regression models of RF have been applied in this study.

Feature and Parameter Selection

To objectively evaluate the performance of the RF model proposed in this study, the O-O-B prediction results is used in the feature and parameter selection process. Then, the predicted building height and reference building height are used to calculate the coefficient of determination (R^2) and RMSE.

In RF model construction, the numbers of leaves and decision trees can significantly influence the regression accuracy and need to be determined. In this study, the number of decision trees is increased from 50 to 1000 at intervals of 50, and the number of leaves is selected as 1, 5, 10, 20, 50, and 100, respectively. Finally, the optimal parameters of

RF were determined, with the tree numbers of 500 and leave numbers of 1, corresponding to minimum RMSE in O-O-B prediction results.

In addition, there are totally 512 features acquired by the previous steps, which is too much for RF model construction because the "Hughes phenomenon" (Hughes 1968). Thus, to reduce the dimensions of the input features, all the 512 features are ranked in decent order according to the corresponding importance in RF model. At the same time, the number of features is increased from 1 to 512 at intervals of 10 for improving computing efficiency. Figure 5 shows the R^2 and RMSE between the predicted building height and reference building height versus different numbers of input features. It shows that the RF models using the first 371 features have the lowest RMSE between reference building floors and predicted floors. Thus, those features are used for model construction with the rest features are discarded.

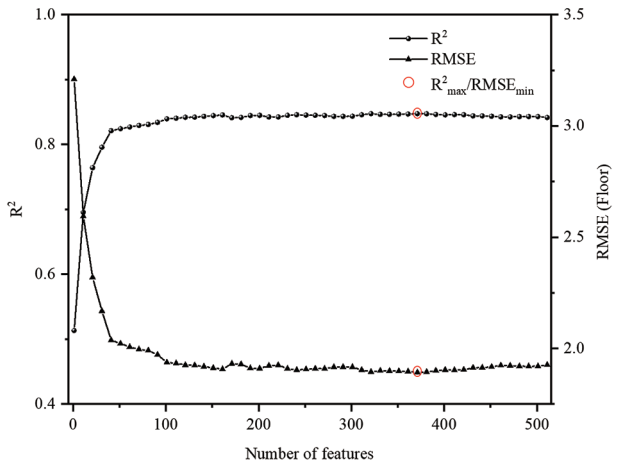

Figure 5. The relation of R^2 and root-mean-square error (RMSE) with the number of input features.

Model Construction

Based on the parameters selected in the previous section, the RF model for building height estimation is constructed. The basic principle and construction process are shown as follows:

(1) All the 574 350 effective samples selected in previous step are divide into two data sets, with 70% as the training data set and rest 30% as the testing data set. Then, the training data set are split into three sub-groups of Group-1, Group-2, and Group-3, respectively, according to the actual floors of 1–6 floors, 7–12 floors, and over 12 floors.

(2) Four RF models are construed based on different input corresponding training-data set samples. The first RF classification model (RF_c) is constructed using all training data set; and the rest three RF regression models (RF_r) of $RF_{1\text{-}6}$, $RF_{7\text{-}12}$, and $RF_{>12}$ are constructed based on training data set of Group-1, Group-2, and Group-3, respectively.

(3) The height of the testing data set samples is firstly estimated based on the constructed RF_c model. Then, all the testing samples are classified into three sub-groups according to the prediction results.

(4) Based on the corresponding groups' RF regression models, the prediction results are taken as the final estimation result of the testing data set samples. For example, once a sample pixel of actual four floors is estimated in Group-1 by RF_c. The prediction result of regression model $RF_{1\text{-}6}$ is taken as the final result of this sample pixel.

(5) The differences between training-data set' actual floors and the RF_c–RF_r models prediction result is taken as the estimation error of the model proposed in this study.

To make a robust estimation of the proposed model, the upward process of steps (1)–(5) is repeated 10 times. After that, the mean of those 10 times' result is taken as the final result in this study. The procedure for the estimation of the building height is shown in Figure 6.

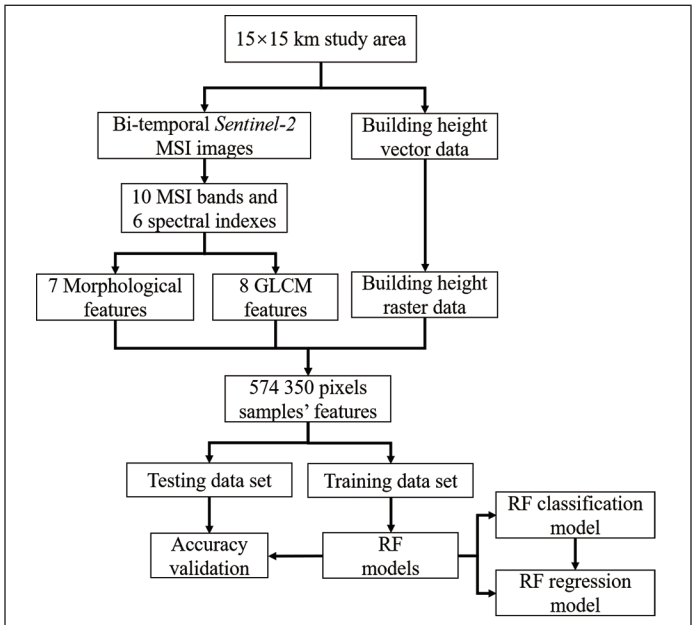

Figure 6. Procedure for the estimation of the building height. MSI = multispectral instrument; GLCM = gray level co-occurrence matrix; RF = random forest.

Result

Estimation Accuracy

The RF Classification Model Accuracy

With all the training samples input into the RF classification model of RFc, the classification accuracy of the three sub-groups is evaluated. Table 4 is the confusion matrix of the three groups of testing data set's classification result based on RF classification model. It can be seen that the three groups of data have the high accuracy with the user's accuracy and producer's accuracy all larger than 88%. The overall accuracy is 98.4% with a Kappa Coefficient of 0.93. It indicates that the classification model can accurately classify the samples into the corresponding sub-groups.

Table 4. The confusion matrix of testing data set's classification result.

	1–6 Floors	7–12 Floors	>12 Floors	Total	User's Accuracy
1–6 floors	**149851**	135	283	150269	99.72%
7–12 floors	1198	**9657**	104	10959	88.12%
>12 floors	985	27	**10065**	11077	90.86%
Total	152034	9819	10452	172305	
Producer's Accuracy	98.56%	98.35%	96.30%		
Overall Accuracy	98.41%			Kappa Coefficient	0.93

In the confusion matrix, the bold font represents the predicted value equals the actual value, reflecting the accuracy of the classification results.

Figure 7 is the proportion of the reference value, predicted value, and the RF classification accuracy of the three groups in testing data set. The proportion of each group of testing data set is similar to the proportion in the entire study area: Group-1 occupies the main part, and the Group-2 and Group-3 have similar samples amount, accounting for about 6%, respectively. Among them, due to the large number

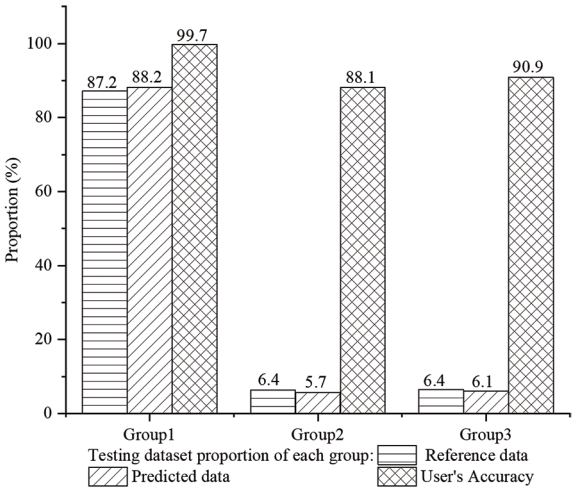

Figure 7. The proportion of the reference value, predicted value, and the Random Forest (RF) classification accuracy of the three groups in testing data set.

of samples in the Group-1 and the height difference is five floors; the accuracy rate is as high as 99.7%. Due to the small proportion of Groups-2 and -3 in the training and testing data data sets, the classification accuracy of these two groups is not as high as that of Group-1.

The RF Regression Models Accuracy

As all the samples in training data set are classified into three groups according to the corresponding floor numbers, the relationship between RF regression models predicted building floors, and the corresponding reference floors of Group-1, Group-2, and Group-3 are shown in Figure 8a–c, respectively. It can be seen from testing data distribution that there are good test results in three groups, and the RMSE is 0.61 floor for $RF_{1\text{-}6}$, 0.41 floor for $RF_{7\text{-}12}$, and 0.98 floor for $RF_{>12}$, all results are less than 1.00 floor. The heat map is mainly distributed along the one-to-one line. But in the third group, buildings below 30 floors are evenly distributed along both sides of one-to-one line, but for buildings greater than 30 floors, the prediction error is relatively large. In addition, due to the lack of data of the 33rd, 34th, and 36th floor buildings, there are no data for those floors in the heat map Figure 8c.

Finally, we combine the constructed RFc classification model and the three regression models to frame the heat map relationship between the testing data set' reference height and the predicted height in Figure 9. It shows that after the calculation of the RF_c and RF_r models, the relationship between predicted value and reference value is closer to one-to-one line with the RMSE of 1.62 floor. These results corroborate the effectiveness of the proposed method for building height estimation. In addition, compared with the RMSE of 1.75 floor shown in Figure 4, the prediction accuracy is improved after feature and parameter selection.

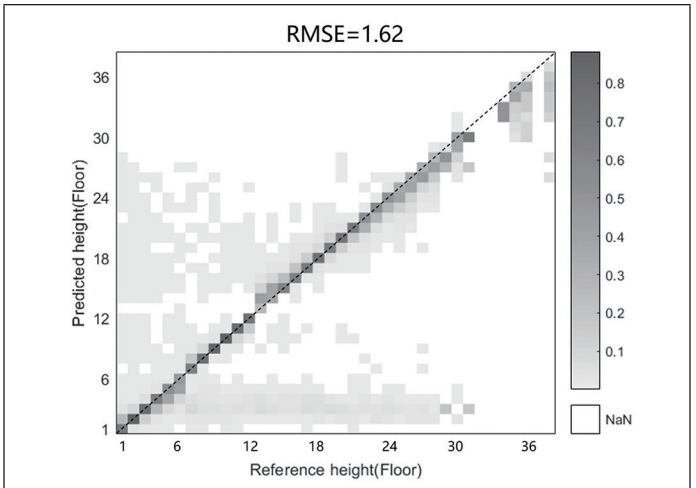

Figure 9. The results of combination use of RFc and RFr models. RMSE = root-mean-square error.

Actual Applications

Based on the RF models proposed in this study, we can acquire the estimated buildings height of the study area. Namely, the 30% testing data set prediction results of those three groups of RF models. Figure 10a is the reference building height image of the study area, Figure 10b is the predicted building height image of the same area, and Figure 10c is the difference between 10b and 10a. Figure 10c shows that there are few building pixels with large error value. The conditions with larger errors mainly due to the predicted values generated by classification model of RF_c classify the samples into wrong sub-groups. Especially for the buildings over 12 floors, the error is greater. Figure 10d is the histogram of the samples in Figure 10c. It can be seen that the error between the predicted floors and the reference floors in the study area is mostly below five floors, and the samples with absolute value of prediction errors less than one floor accounts for 95.39% of the total samples.

In order to further verify the rationality of the method proposed in this paper, we selected three 2 km × 2 km rectangular areas of I, II, and III in the study area, which are shown in the yellow rectangle in Figure 11.

It can be seen from Figure 11 that for the three selected areas, the predicted building height of the pixel is relatively consistent with the reference value, and only a few pixels have obvious errors. Figure 11 shows that different regions have different characteristics: Region I contains a total of 16 187 building pixels, and the proportions of the three groups of buildings are 65.32%, 8.07%, and 26.60%, respectively. The buildings over 12 floors take a larger proportion in Region I than in the overall study area. About 73.97% building pixels are accurately estimated (namely the predicted value is the same as the reference value after rounding; for example, the reference value is three floors, and the predicted value is also three floors), and the regional overall RMSE = 2.79 floor. Region II contains a total of 17 809 building

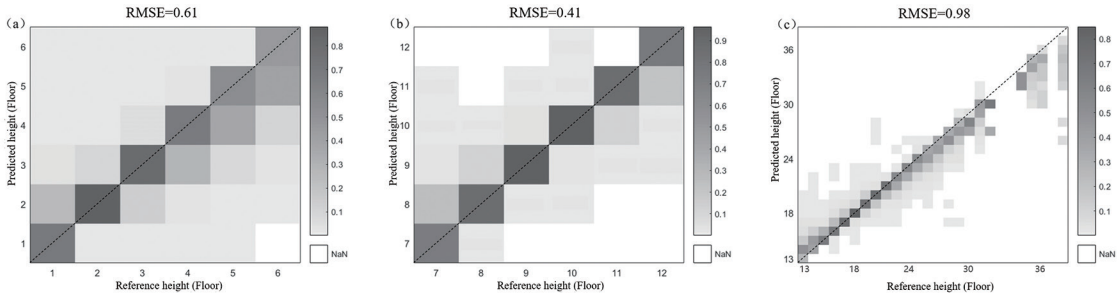

Figure 8. Three Random Forest (RF) regression models' prediction results. (a) 1–6 floors group (b) 7–12 floors group, and (c) higher than 12 floors group. RMSE = root-mean-square error.

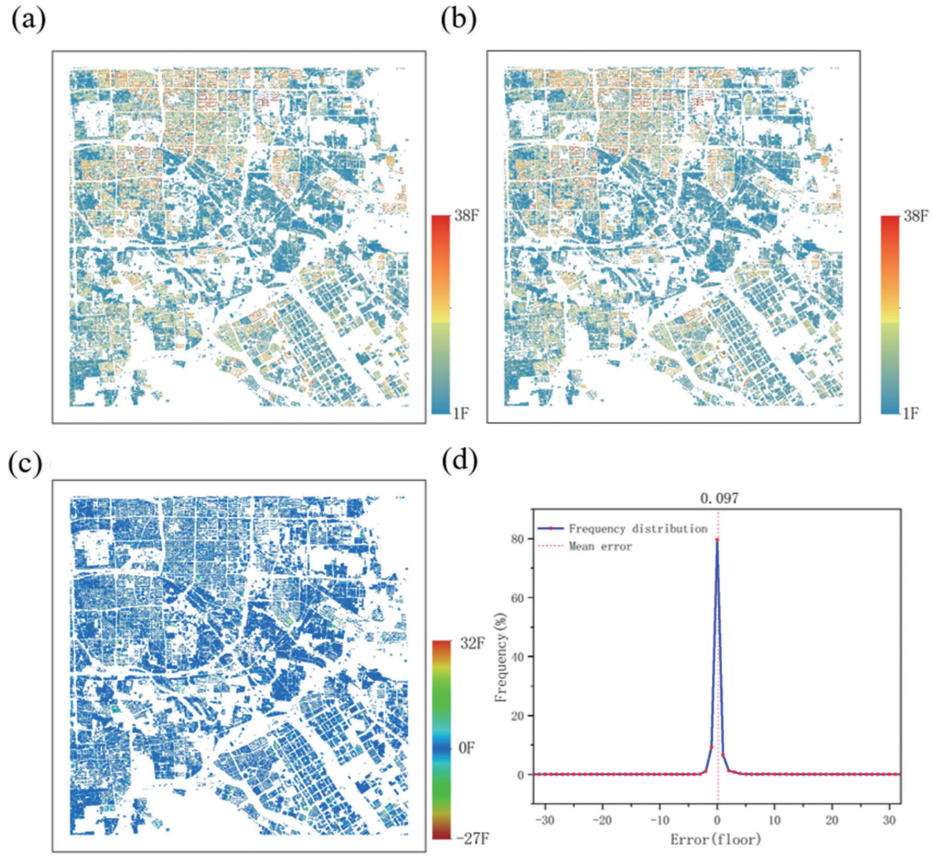

Figure 10. (a) Reference building height image of the study area; (b) predicted building height image; (c) the difference between (b) and (a); (d) histogram of (c).

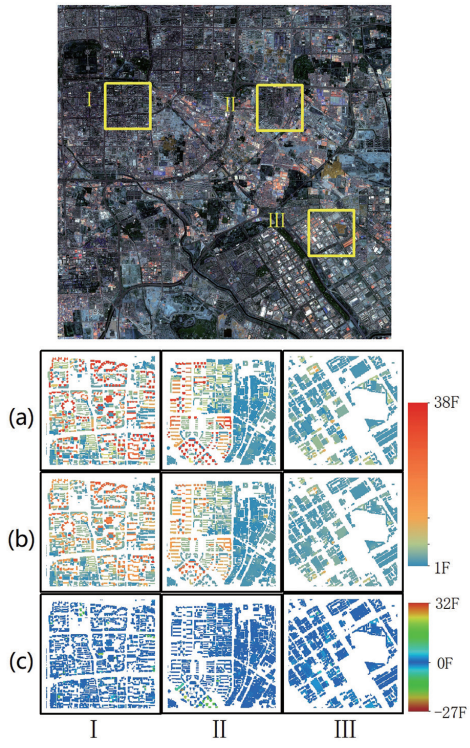

Figure 11. The locations of three 2 km × 2 km areas. (a) Reference building height image, (b) predicted building height image, and (c) the deviation between (b) and (a).

pixels, and the proportions of the three types of buildings are 83.23%, 6.62%, and 10.15%, respectively. There is a clear boundary between low-rise buildings and high-rise buildings. About 80.54% building pixels are accurately estimated, and the regional overall RMSE = 2.34 floor. Region III contains a total of 15 014 building pixels, and the proportions of the three types of buildings are 96.20%, 3.30%, and 0%, respectively, all buildings are below 12 floors. About 67.78% building pixels are accurately estimated, and the regional overall RMSE = 1.09 floor. On the whole, the overall regression effect of the data is good, indicating that the RF building height estimation used has a certain degree of accuracy.

Figure 12 shows the number of samples with respect to building floors for reference data and RF model predicted results. It can be seen that the predicted height has a similar distribution to the reference height. In addition, because one-floor buildings' shadow gap is small between the two seasons, the number of predicted one-floor building is less than the number of predicted one-floor building.

Discussion

Analysis of Using Different Input Data

Comparison with Only Using Single Temporal Image

Note that the bi-temporal *Sentinel-2* MSI images close to winter solstice and summer solstice are used in this study to predict the building height. For comparison, the RF models of only using winter solstice and summer solstice image is also constructed similar as the bi-temporal model. Figure 13 is the O-O-B RMSE with respect to a different number of trees in the RF model for using a winter image, summer image, and bi-temporal images, respectively. It shows that the RF-model constructed with single summer image perform worst, the maximum RMSE is 1.86 floor, while the bi-temporal image performs best, the RMSE is the minimum 1.75 floor (without feature and parameter selection in

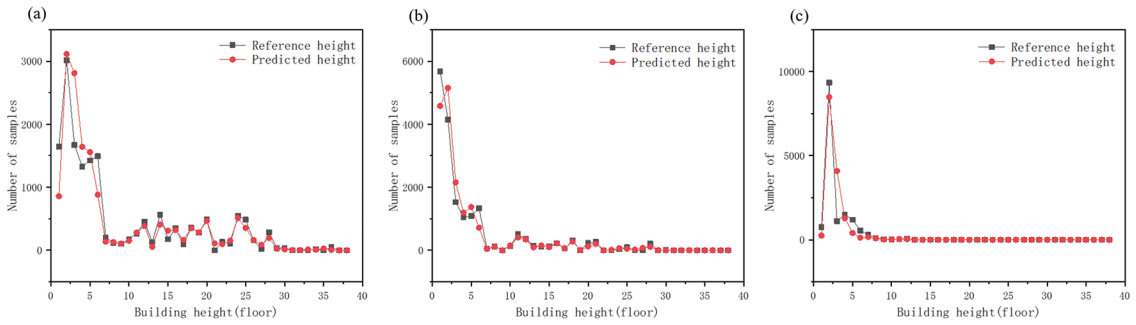

Figure 12. Comparison of reference and predicted building height of three 2 km × 2 km region I, II, and III.

the "Feature and Parameter Selection" section). Thus the bi-temporal images are finally used to predict the building height in this study.

Comparison with Not Removing Cloud Pixels

Note that the *Sentinel-2* images after cloud mask are used in this study. As comparison, the RF model of using original images, namely after atmospheric correction but without remove cloud pixels, are also constructed. Figure 14 shows the O-O-B RMSE versus number of trees using the data with and without cloud removal operation. The RMSE is 2.14 without the cloud removal, which is much larger than the RMSE of 1.75 using cloud removed data. It indicates that the cloud removal is useful to improve the prediction accuracy of the constructed RF model.

Note that the optical images are inevitably affected by clouds and cloud shadows (Li *et al.* 2019; Zhu *et al.* 2015); it was hard to acquire the clear sky images on the winter solstice and summer solstice simultaneously. To avoid the influences of clouds, the *Sentinel-2* images close to the winter solstice and summer solstice can be used in this study. In addition, after performing cloud mask processing based on the quality-scene-classification file, the 130 m × 130 m square (matching 13 × 13 pixels) with the cloud as the center is removed. Therefore, is also very important to select the cloud coverage in the effective data in the study area and we need to balance between the cloud coverage, the size of structural element, and the amount of data during the model establishment.

Transferability of the Method for Other Regions

With regard to the transferability of our building height estimation method, there are some points need to be declared. The solar zenith and azimuth angles are different for the different location as the *Sentinel-2* observe. Thus, the shadow length is different for different locations in bi-temporal images. This can induce some uncertainties in building height estimation, as the model trained based on high latitudes data used for some low latitude areas. In addition, the gray level change characteristics of GLCM can be calculated in four directions. Only the 90° direction is selected in this study due to the regional characteristics of Beijing (north of the Tropic of Cancer). Different countries and regions should select optimal direction according to the actual correlation coefficient.

Besides that, the building outlines are used to extract building pixels before RF model construction. In actual applications, besides the *Sentinel-2* optical images, the building outlines in vector format such as Open Street Map or building layers in raster format such as Global Human Settlement Layer (Martino *et al.* 2016) are necessary to extract building pixels before height prediction. As long as the above-mentioned aspects are taken into account during the model training, the building height estimation method using bi-temporal MSI images can be used for other areas.

Note that the height information at the individual building scale is indeed more useful for many applications such as real property rights registration and cadastral surveying. But the building height products with different spatial resolutions have different applications. For example, this product in 10 m resolution is useful for population density estimation in 100 m or 1 km or seismic risk estimation at large areas. What is more important is that the height information at individual building scale is not available for some remote or underdeveloped regions. The height information produced by the method proposed in this study can be an efficient and cost-effective substitute of individual building scale height products.

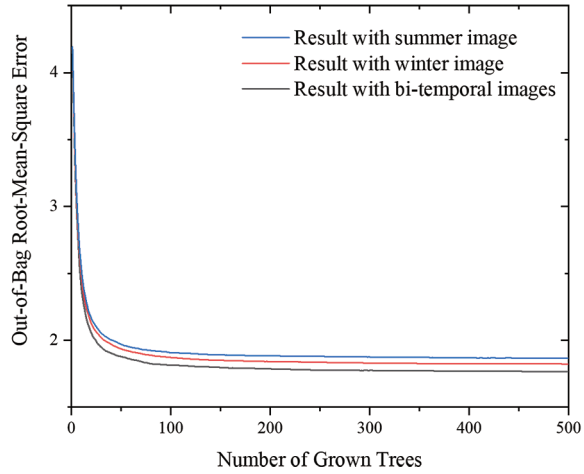

Figure 13. Out-of-Bag (O-O-B) root-mean-square error (RMSE) with respect to different number of trees of using single and bi-temporal images.

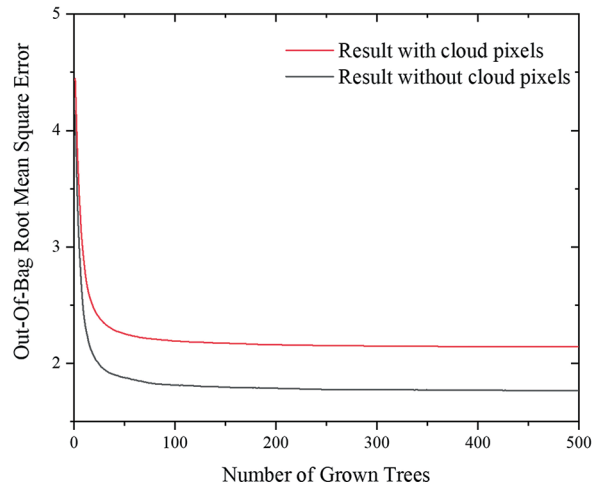

Figure 14. Out-of-Bag (O-O-B) root-mean-square error (RMSE) versus different number of trees with and without cloud removal.

Prediction Accuracy of High-Rise Buildings

This study selects the building pixels within the 15 km × 15 km area of Beijing in 2017. After comparing the predicted building height and

the reference value, it shows that the prediction accuracy of high-rise buildings (taller than 12 floors) is lower than the low-rise buildings (less than 12 floors). The possible reasons are as follows: (1) It may be that the ground interval between high-rise buildings are too small, inducing shadows cover other building pixels or overlap between shadows. (2) We only studied the features within 60 m in each direction of building pixels when performing feature extraction of morphology and GLCM, but actual high-rise building shadows may far exceed this range in winter in Beijing. (3) In the process of model training, the samples of over 12 floors in the study area were insufficient compared with less than 12 floor conditions, resulting in the training was unstable.

Note that for some actual applications such as seismic risk analysis, the building height data produces by the method proposed in this study is sufficient to correctly classify the building into the corresponding sub-groups. Namely, the RMSE of high-rise buildings of about the 1.62 floor is sufficient for the estimation of seismic vulnerability of buildings. However, to map the height of buildings across the country, we should select as many high-rise building samples as possible, such as Shanghai and Shenzhen, to improve the prediction accuracy of the proposed model.

It should be noted that the reference building height data used in this study is the number of building floors, not meters. The floor height of buildings in China is around 2.8 m, with different buildings commonly having different heights. This can induce some uncertainty in floor number estimation using the bi-temporal image-based method. Thus, the RMSE can be further reduced as more accurate reference data of building height data become available.

Conclusions

The building height information is a very important parameter for many applications, such as urban planning and population density estimation. There are some typical methods to estimate buildings height: the building shadow-based method using very-high-resolution optical images; the photogrammetry method based on stereo image pairs or InSAR images to extract the digital elevation model and building height; and the lidar data-based method acquired from drones. However, those methods discussed above rely on data that are difficult and expensive to acquire or that can only be used for a limited area. Considering the mid-resolution satellite data have the advantages of being easier to access compared with VHR images and have a global coverage compared with the local coverage of airborne data, this study tries to estimate the building height based on the mid-resolution satellite images of *Sentinel-2*.

The region of 15 km × 15 km in central Beijing, China is taken as the study area. Based on the bi-temporal optical images, the spectral features, mathematical morphology indexes, and the gray level co-occurrence matrix are all considered. The widely used random forest model is used to estimate buildings height. To explore the feasibility of the building height estimation using *Sentinel-2* images, the samples of the study area are randomly split into two parts: 70% as the training data set and the rest 30% as the testing data set.

A classification model is proposed based on the RF model, classifying all the buildings into three sub-groups: 1–6 floors, 7–12 floors, and above 12 floors. Then three RF regression models are proposed to predict the corresponding building height. Based on the test data, it shows that the overall accuracy rate of the RF classification model has reached 98.4% and the kappa coefficient is 0.93. The RF regression models' RMSE is 0.61 floor for 1–6 floors group, 0.41 floor for 7–12 floor group, and 0.98 floor for above 12 floors group. The final results show that the bi-temporal *Sentinel-2* images have good accuracy in predicting the height of buildings with the RMSE of the 1.62 floor for all effective data. This result shows that this method has great potential for large-scale building mapping and regional large-scale disaster assessment.

Acknowledgments

This work was jointly supported by the Director Fund of Institute of Geology, China Earthquake Administration (No. IGCEA2106), National Natural Science Foundation of China (Grant No. 42071337), and National Key R&D Program of China (No. 2018YFC1504403 and No. 2018YFC1504503).

References

Alahmadi, M., P. Atkinson and D. Martin. 2013. Estimating the spatial distribution of the population of Riyadh, Saudi Arabia using remotely sensed built land cover and height data. *Computers, Environment and Urban Systems* 41:167–176.

Biljecki, F., H. Ledoux and J. Stoter. 2017. Generating 3D city models without elevation data. *Computers, Environment and Urban Systems* 64:1–18.

Cao, Q., Q. Luan, Y. Liu and R. Wang. 2021. The effects of 2D and 3D building morphology on urban environments: A multi-scale analysis in the Beijing metropolitan region. *Building and Environment* 192:107635.

Cao, Y. and X. Huang. 2021. A deep learning method for building height estimation using high-resolution multi-view imagery over urban areas: A case study of 42 Chinese cities. *Remote Sensing of Environment* 264:112590.

Chen, Y. and F. Y. Yang. 2012. Analysis of image texture features based on gray level co-occurrence matrix. *Applied Mechanics & Materials* 204–208:4746–4750.

Cheng, F. and K. H. Thiel. 2007. Delimiting the building heights in a city from the shadow in a panchromatic SPOT-image—Part 1. Test of forty-two buildings. *International Journal of Remote Sensing* 16(3):409–415.

Crist, E. P. 1985. A Tm tasseled cap equivalent transformation for reflectance factor data. *Remote Sensing of Environment* 17(3):301–306.

Dalla Mura, M., J. A. Benediktsson, B. Waske and L. Bruzzone. 2010. Morphological attribute profiles for the analysis of very high resolution images. *IEEE Transactions on Geoscience and Remote Sensing* 48(10):3747–3762.

Dong, Y., M. Liao, X. Zhang and F. Wang. 2011. Faults diagnosis of rolling element bearings based on modified morphological method. *Mechanical Systems & Signal Processing* 25(4):1276–1286.

Drusch, M., U. Del Bello, S. Carlier, O. Colin, V. Fernandez, F. Gascon, B. Hoersch, C. Isola, P. Laberinti, P. Martimort, A. Meygret, F. Spoto, O. Sy, F. Marchese and P. Bargellini. 2012. Sentinel-2: ESA's optical high-resolution mission for GMES operational services. *Remote Sensing of Environment* 120:25–36.

Dubois, C., A. Thiele and S. Hinz. 2016. Building detection and building parameter retrieval in InSAR phase images. *ISPRS Journal of Photogrammetry and Remote Sensing* 114:228–241.

Ergun, B. 2007. Creating A 3D urban model by terrestrial laser scanners and photogrammetry techniques: A case study on the historical peninsula of Istanbul. *Proceedings Society of Photo-Optical Instrumentation Engineers (SPIE) Conference Series 6618*:66180H. https://doi.org/10.1117/12.720988.

European Space Agency (ESA). 2015. *Sentinel-2_User_Handbook*, 1–64. Paris: ESA.

Frantz, D., F. Schug, A. Okujeni, C. Navacchi, W. Wagner, V. Sebastian, and P. Hostert, 2021. National-scale mapping of building height using Sentinel-1 and Sentinel-2 time series. *Remote Sensing of Environment: An Interdisciplinary Journal* 252. https://doi.org/10.1016/j.rse.2020.112128

Gamba, P., B. Houshmand and M. Saccani. 2000. Detection and extraction of buildings from interferometric SAR data. *IEEE Transactions on Geoscience and Remote Sensing* 38(1):611–618.

Gong, P., Z. Li, H. Huang, G. Sun and L. Wang. 2011. ICESat GLAS data for urban environment monitoring. *IEEE Transactions on Geoscience and Remote Sensing* 49(3):1158–1172.

Han, T., D. Jiang, Q. Zhao, L. Wang and K. Yin. 2018. Comparison of random forest, artificial neural networks and support vector machine for intelligent diagnosis of rotating machinery. *Transactions of the Institute of Measurement and Control* 40(8). https://doi.org/10.1177/0142331217708242.

Haralick, R. M. 1973. Textural features for image classification. *IEEE Transactions on Systems, Man and Cybernetics* SMC(3):610–621.

Hughes, G. F. 1968. On the mean accuracy of statistical pattern recognizers. *IEEE Transactions on Information Theory* 14(1):55–63.

LeCun, Y., Y. Bengio and G. Hinton. 2015. Deep learning. *Nature* 521(7553):436–444.

Leichtle, T., T. Lakes, X. X. Zhu and H. Taubenböck. 2019. Has Dongying developed to a ghost city?—Evidence from multi-temporal population estimation based on VHR remote sensing and census counts. *Computers, Environment and Urban Systems* 78:101372.

Li, H., Y. Zhou, G. Jia, K. Zhao and J. Dong. 2022. Quantifying the response of surface urban heat island to urbanization using the annual temperature cycle model. *Geoscience Frontiers* 13:101141.

Li, X., L. Wang, Q. Cheng, P. Wu, W. Gan and L. Fang. 2019. Cloud removal in remote sensing images using nonnegative matrix factorization and error correction. *ISPRS Journal of Photogrammetry and Remote Sensing* 148:103-113.

Li, X. and P. Gong. 2016. Urban growth models: Progress and perspective. *Science Bulletin* 61(21):1637–1650.

Li, X., Y. Zhou, P. Gong, K. C. Seto and N. Clinton. 2020. Developing a method to estimate building height from Sentinel-1 data. *Remote Sensing of Environment* 240:111705.

Lu, P., W. Shi, Q. Wang, Z. Li, Y. Qin and X. Fan. 2021. Co-seismic landslide mapping using Sentinel-2 10-m fused NIR narrow, red-edge, and SWIR bands. *Landslides* 18(6):2017–2037.

Lu, P., Y. Qin, Z. Li, A. C. Mondini and N. Casagli. 2019. Landslide mapping from multi-sensor data through improved change detection-based Markov random field. *Remote Sensing of Environment* 231:111235.

Manning, W. J. 2011. Urban environment: defining its nature and problems and developing strategies to overcome obstacles to sustainability and quality of life. *Environ Pollutution* 159(8–9):1963–1964. https://doi.org/10.1016/j.envpol.2011.04.002.

Martinez-Carricondo, P., F. Carvajal-Ramirez, L. Yero-Paneque and F. Aguera-Vega. 2020. Combination of nadiral and oblique UAV photogrammetry and HBIM for the virtual reconstruction of cultural heritage. Case study of Cortijo del Fraile in Nijar, Almeria (Spain). *Building Research and Information* 48(2):140–159.

Martino, P., C. Christina, J. Andreea, F. Aneta, S. Vasileios and S. Pierre. 2016. Assessment of the added-value of Sentinel-2 for detecting built-up areas. *Remote Sensing* 8(4):299.

Mesev, V. 2001. Morphological image analysis: Principles and applications. *Environment and Planning B-Planning & Design* 28(5):800–801.

Goutsias, J.I., L.M. Vincent and D.S Bloomberg, *Mathematical Morphology and its Applications to Image and Signal Processing,* Proceedings of the Computational Imaging and Vision, 2000.

Mueller-Wilm, U. 2020. *Sen2Cor Configuration and User Manual*. Paris: European Space Agency.

Qiu, C., L. Mou, M. Schmitt and X.X. Zhu. 2020a. Fusing multiseasonal Sentinel-2 imagery for urban land cover classification with multibranch residual convolutional neural networks. *IEEE Geoscience and Remote Sensing Letters* PP(99):1–5.

Qiu, C., M. Schmitt, C. Geiss, T. K. Chen and X. X. Zhu. 2020b. A framework for large-scale mapping of human settlement extent from Sentinel-2 images via fully convolutional neural networks. *ISPRS Journal of Photogrammetry and Remote Sensing* 163(May):152–170.

Shao, Y., G. N. Taff and S. J. Walsh. 2011. Shadow detection and building-height estimation using IKONOS data. *International Journal of Remote Sensing* 32(22):6929–6944.

Shi, T. and H. Xu. 2019. Derivation of tasseled cap transformation coefficients for Sentinel-2 MSI at-sensor reflectance data. *IEEE Journal of Selected Topics in Applied Earth Observations and Remote Sensing* 12(10):4038–4048.

Stilla, U., U. Soergel and U. Thoennessen. 2003. Potential and limits of InSAR data for building reconstruction in built-up areas. *ISPRS Journal of Photogrammetry and Remote Sensing* 58(1–2):113–123.

Svennevig, K., P. Guarnieri and L. Stemmerik. 2015. From oblique photogrammetry to a 3D model—Structural modeling of Kilen, eastern North Greenland. *Computers & Geosciences* 83:120–126.

Thiele, A., E. Cadario, K. Schulz, U. Thonnessen and U. Soergel. 2007. Building recognition from multi-aspect high-resolution InSAR data in urban areas. *IEEE Transactions on Geoscience and Remote Sensing* 45(11):3583–3593.

Torres, R., P. Snoeij, D. Geudtner, D. Bibby, M. Davidson, E. Attema, P. Potin, B. Rommen, N. Floury, M. Brown, I. N. Traver, P. Deghaye, B. Duesmann, B. Rosich, N. Miranda, C. Bruno, M. L'Abbate, R. Croci, A. Pietropaolo, M. Huchler and F. Rostan. 2012. GMES Sentinel-1 mission. *Remote Sensing of Environment* 120:9–24.

Transon, J., R. d'Andrimont, A. Maugnard and P. Defourny. 2018. Survey of hyperspectral Earth observation applications from space in the Sentinel-2 context. *Remote Sensing* 10(3):157.

Trekin, A. N., V. Y. Ignatiev and P. Y. Yakubovskii. 2020. Deep neural networks for determining the parameters of buildings from single-shot satellite imagery. *Journal of Computer and Systems Sciences International* 59(5):755–767.

Tucker, C. J. 1978. Red and photographic infrared linear combinations for monitoring vegetation. *Remote Sensing and Environment* 8(2):127–150.

van der Meer, F. D., H.M.A. van der Werff and F.J.A. van Ruitenbeek. 2014. Potential of ESA's Sentinel-2 for geological applications. *Remote Sensing of Environment* 148:124–133.

Wang, J., Y. Wang, T. Wang, S. Liu, H. Wang, T. Dong and Y. Wang. 2020. 1.34 μ m Q-switched Nd:YVO_4 laser based on Perovskite film saturable absorber. *IEEE Photonics Technology Letters* 32(1):3–6.

Wang, Q., W. Shi, Z. Li and P. M. Atkinson. 2016. Fusion of Sentinel-2 images. *Remote Sensing of Environment* 187:241–252.

Wang, X. Q., X. M. Yu and F. L. Ling. 2014. Building heights estimation using Zy3 Data—A case study of Shanghai, China. *Proceedings 2014 IEEE International Geoscience and Remote Sensing Symposium (IGARSS)*, held in Quebec City, Canada, 13–18 July 2014, 1749–1752.

Wegner, J. D., J. R. Ziehn and U. Soergel. 2014. Combining high-resolution optical and InSAR features for height estimation of buildings with flat roofs. *IEEE Transactions on Geoscience and Remote Sensing* 52(9):5840–5854.

Xu, H. 2007. Modification of normalised difference water index (NDWI) to enhance open water features in remotely sensed imagery. *International Journal of Remote Sensing* 27(14):3025–3033.

Yu, Z., H. Li, F. Ba and Z. Wang. 2018. 3D city model construction based on a consumer-grade UAV. *Remote Sensing for Land & Resources* 30(2):67–72.

Zha, Y., J. Gao and S. Ni. 2003. Use of normalized difference built-up index in automatically mapping urban areas from TM imagery. *International Journal of Remote Sensing* 24(3):583–594.

Zhu, Q. and Y. Ma. 2014. Application and research of building modeling based on 3D laser scanner. *Geography and Geo-Information Science* 30(6):31–35.

Zhu, Z., S. Wang and C. E. Woodcock. 2015. Improvement and expansion of the Fmask algorithm: Cloud, cloud shadow, and snow detection for Landsats 4–7, 8, and Sentinel 2 images. *Remote Sensing of Environment* 159:269–277.

Generation of High-Resolution Orthomosaics from Historical Aerial Photographs Using Structure-from-Motion and Lidar Data

Ji Won Suh and William Ouimet

Abstract

This study presents a method to generate historical orthomosaics using Structure-from-Motion (SfM) photogrammetry, historical aerial photographs, and lidar data, and then analyzes the horizontal accuracy and factors that can affect the quality of historical orthoimagery products made with these approaches. Two sets of historical aerial photographs (1934 and 1951) were analyzed, focused on the town of Woodstock in Connecticut, U.S.A. Ground control points (GCPs) for georeferencing were obtained by overlaying multiple data sets, including lidar elevation data and derivative hillshades, and recent orthoimagery. Root-Mean-Square Error values of check points (CPs) for 1934 and 1951 orthomosaics without extreme outliers are 0.83 m and 1.37 m, respectively. Results indicate that orthomosaics can be used for standard mapping and geographic information systems (GIS) work according to the ASPRS 1990 accuracy standard. In addition, results emphasize that three main factors can affect the horizontal accuracy of orthomosaics: (1) types of CPs, (2) the number of tied photos, and (3) terrain.

Introduction

Land use land cover (LULC) change plays a fundamental role in recording the impact of human activities on earth surface processes and understanding these impacts is one of the grand challenges in environmental science today (National Research Council 2001). Satellite-based data such as Landsat have been widely used to understand LULC in the field of remote sensing (Leh *et al.* 2013; Verbesselt *et al.* 2012; Zhu *et al.* 2016, 2020; Zhu and Woodcock 2014), but are limited in terms of temporal scope (Landsat first launched in 1972) and spatial resolution (with the best available pixel resolution being 15–30 m between the 1970s and early 2000s). To understand historical LULC changes prior to the satellite era and at much higher spatial resolution, historical aerial photography has long been considered an important source of data, adding multiple new time intervals in the study of land use activity in forestry, ecology, urban planning, cultural resources, and geomorphology related studies (Kadmon and Harari-Kremer 1999; Llena *et al.* 2018; Mallinis *et al.* 2011; Nita *et al.* 2018; Rocchini *et al.* 2006; Sevara 2013; Verhoeven *et al.* 2012; Zomeni *et al.* 2008).

Unlike modern remote sensing imagery derived from airplanes, unmanned aerial vehicles (UAV) or satellites, a number of issues need to be taken into account when using historical aerial photographs. These include: (1) low data accessibility, (2) no georeferencing, (3) time-consuming work for mosaicking fragmented aerial photograph campaigns and scaling up the spatial extent, (4) poor information for aligning or calibrating individual aerial photograph such as camera position, flight altitude, yaw, pitch, and roll (Fox and Cziferszky 2008; Frankl *et al.* 2015), (5) no ground control points (GCPs), which are crucial in removing inherent radial distortion and tilt for georeferencing (Bolstad 1992; Wolf *et al.* 2014), and (6) low image quality due to digital scanning. These problems have generally restricted the application of modern photogrammetric techniques when dealing with historical data (Lingua *et al.* 2009; Turner *et al.* 2012; Weng *et al.* 2013). In addition, they can attenuate errors associated with automated image processing in photogrammetric software such as Agisoft Metashape and Pix4Dmapper when it comes to the shortage of metadata or increasing the number of photos stitched.

Despite these challenges, a number of studies have been conducted to orthorectify historical aerial photographs and reconstruct historical digital elevation models (hDEM) based on photogrammetric techniques such as Structure-from-Motion (SfM). The historical aerial photography considered in these studies ranges from the 1930s (Fox and Cziferszky 2008; Frankl *et al.* 2015; Geyman *et al.* 2022) to the 1990s (Arnaud *et al.* 2015) and most of the research has been concentrated on images from the 1950s onward (Comiti *et al.* 2011; Gennaretti *et al.* 2011; Gomez 2014; Kadmon and Harari-Kremer 1999; Llena *et al.* 2018; Marignani *et al.* 2008; Maurer and Rupper 2015; Nebiker *et al.* 2014; Rocchini *et al.* 2006). To overcome the lack of external information of historical data, creating GCPs from reference data such as DEMs is essential during SfM processing. Depending on the spatial resolution of reference data, the quality of output orthomosaics or DEMs varies. The quality of orthomosaics has been evaluated by root-mean-square error (RMSE) and the RMSE results with coarse reference data (e.g., ~10–40 m) ranges from 5 m to 15 m (Baker *et al.* 1995; Gennaretti *et al.* 2011; Marignani *et al.* 2008; Rocchini *et al.* 2006).

The advent of Light Detection and Ranging (lidar) data and high-resolution DEMs (e.g., 1 m) can lead to increasing the accuracy of historical orthomosaics and hDEMs given that lidar derivatives such as hillshades allow for visualizing of small-scale features and greater potential for choosing GCP with accurate coordinates and elevation values. To date, however, the application of high-resolution topographic data from lidar in SfM photogrammetry processing has been focused on assessing vertical accuracy of hDEM products (Child *et al.* 2021; Nebiker *et al.* 2014) rather than extracting GCPs for the orthomosaic. One of reasons for this is that high-resolution historical imagery needs high-resolution topographic data as a reference to build orthomosaics with less horizontal error. Furthermore, there is a lack of research focused on expanding the spatial extent of orthophotos made from high-resolution historical aerial photos (i.e., less than 1:20 000 scale, less than 1m pixel resolution) and lidar data. This is because a large number of historical photos need to be aligned and orthomosaicked to cover larger spatial extent, in contrast to the aforementioned previous studies that use less than 40 photos. In other words, the paucity of such studies underlines the need for an improved methodological approach. Lidar data and its derivatives provide an opportunity to fill in the gap between the low resolution of reference topographic data (e.g., 30 m DEMs) and the resolution of input from historical imagery (e.g., 1 m) (Llena *et al.* 2018).

Ji Won Suh and William Ouimet are with the Department of Geography, University of Connecticut, Storrs, CT 06269 (ji.suh@uconn.edu).

William Ouimet is also with the Department of Earth Sciences, University of Connecticut, Storrs, CT 06269.

Contributed by Dorota Iwaszczuk, March 17, 2022 (sent for review May 6, 2022; reviewed by Michael Cramer).

Photogrammetric Engineering & Remote Sensing
Vol. 89, No. 1, January 2023, pp. 37–46.
0099-1112/22/37–46

doi: 10.14358/PERS.22-00063R2

The goal of this paper is to present the generation of high-resolution historical orthomosaic over a broad area using SfM photogrammetry combined with GCPs from lidar derivatives. Our objectives are to (1) provide a method to build high-resolution historical orthomosaics by using 1934 and 1951 black and white aerial photographs focused on the town of Woodstock, Connecticut, United States; (2) evaluate the horizontal accuracy of orthomosaics based on RMSE values for overall assessment and residual error to understand spatial distribution of errors, and (3) analyze factors that can affect the quality of these historical orthophotos by comparing orthomosaics from 1934 and 1951.

Data and Methods

Study Area

This study was conducted focusing on the town of Woodstock in northeastern Connecticut. In order to cover the entirety of Woodstock, our study area is a rectangle and includes adjacent towns described in Figure 1. To be specific, Figure 1B shows the DEM ranging from 64 m to 335 m and topography in the west part comprised mainly of hilly uplands with mixed coniferous-deciduous forests and agricultural lands. On the other hand, the east part consists of lowland used for agricultural lands as well as mixed forests and muddy brook which flows south into Roseland lake. Distributed over the entire study area are stone walls, stacked around agricultural lands that indicate an anthropogenic legacy of English-style agriculture during the 17th to 20th centuries (Cronon 1983; Thorson 2002) (Figure 1C and 1D). They are easily detected in a hillshade map derived from lidar in open area and deciduous forest (Johnson and Ouimet 2014, 2016).

Data

Collected data for this study can be divided into two sets in terms of usages: to produce historical orthomosaics and to create GCPs (Table 1). In particular, the first data set includes high-resolution black and white air photos of 1934 and 1951 provided from the Connecticut State Library (1934, 1951). For 1934, 141 air photos (spatial scale 1:12 000) were used for an orthomosaic covering about 264 Km² area. The

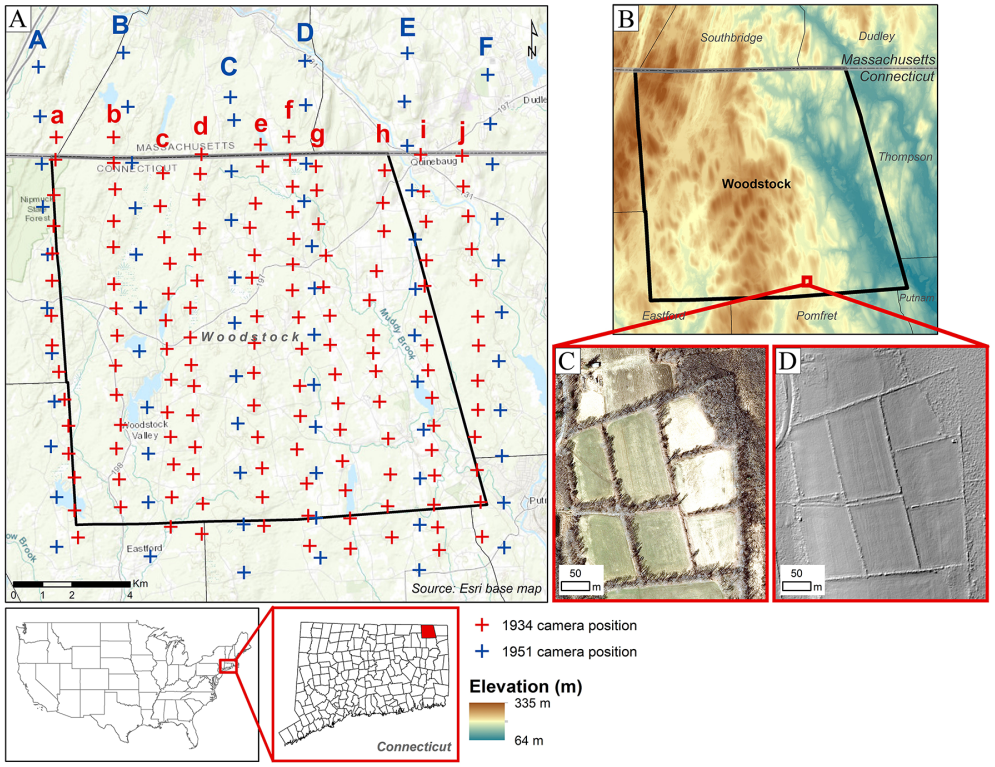

Figure 1. Map of the study area. (A) study area with camera positions of 1934 and 1951 aerial photographs (ESRI, 2012). Lower case and upper case refer to 1934 and 1951 north-south flight paths, respectively; (B) Digital Elevation Model ranging from 64 m to 335 m; (C) an example of stone walls with 2012 leaf-off orthophoto (CT ECO 2012); (D) an example of stone walls with a hillshade map derived from lidar.

Table 1. List of maps and aerial photographs used for this study.

Data Usage	Data Type	Year	Date	Resolution/Map Scale	# of Images (Covering Area)	Source
Historical orthomosaics	A/BW	1934	April 1934	1:12 000	141 (264 Km²)	Connecticut State Library[1]
	A/BW	1951	5 September 1951 13 October 1951 25 November 1951 27 November 1951	1:20 000	68 (380 Km²)	Connecticut State Library[2]
Reference data	A/O/C	2012		0.3 m		CT ECO
	A/O/C	2016		0.07 m		CT ECO
	DEM	2016		1 m		CT ECO
	Hillshade	2016		1 m		2016 DEM

A: aerial photographs; O: ortho-rectified aerial photographs; BW: black and white; C: color. CT ECO = Connecticut Environmental Conditions Online; DEM = digital elevation model.

[1] Connecticut State Library, 1934 Aerial Surveys, Record Group 089:011, Department of Transportation, State Archives.

[2] Connecticut State Library, 1951 Aerial Surveys, Record Group 089:011b, Department of Transportation, State Archives.

vertical photography was taken in April 1934 (note that specific dates were not available) by Fairchild Aerial Survey Corporation using a K-3 aerial survey camera with a 241.3 mm focal length. The survey flights were flown at an altitude of around 3500 m. The overlap rate between two images were approximately 50%. This historical photography was digital-scanned as a 1270 dots-per-inch in 2006. On the other hand, 68 air photos of 1951 (spatial scale 1:20 000) were used covering about 380 Km². Robinson Aerial Surveys took 1951 imagery on the following dates: 5 September 1951, 13 October 1951, 25 November 1951, and 27 November 1951. Unlike 1934 photography, detailed information about survey and scanning process for 1951 was not available. Regarding the number of photos of 1934 and 1951, each 1934 photo covers small extent compared to 1951 photo so that the more photos of 1934 were collected.

As reference data to create GCPs, the second data set includes recent orthophotos (2012 and 2016), DEM derived from 2016 lidar, and a hillshade map produced from lidar DEM. First, 2012 and 2016 high-resolution orthophotos were streamed from Connecticut Environmental Conditions Online (CT ECO) image services in ArcGIS Desktop 10.5 (CRCoG 2016; CT ECO 2012). The spatial resolution of 2012 and 2016 orthoimagery is 0.3 m and 0.07 m, respectively (Table 1). Next, high-resolution DEM from lidar is used to get elevation values of GCPs with fewer errors. Lastly, lidar DEM is also a source to produce a hillshade map that is able to detect surface features such as stone walls (Johnson and Ouimet 2014), which ensures the horizontal position of target locations.

A Workflow for Generating Historical Orthomosaics

In order to build 1934 and 1951 historical orthomosaics and conduct horizontal accuracy assessment, we provided a workflow from steps 1 through 11 by using Agisoft Metashape 1.6 and ArcGIS Desktop 10.5, described in Figure 2. Agisoft LLC (2019) provides a general workflow to build an orthomosaic or DEMs and a number of studies have followed it (Ajayi *et al.* 2017; Midgley and Tonkin 2017; Nita *et al.* 2018; Riquelme *et al.* 2019). However, it needs to be improved for applications involving historical data in order to overcome a lack of photo information and build high-quality georeferenced orthophotos that can be used for mapping and GIS purposes. A workflow consists of three general stages, (1) preprocessing (steps 1 and 2), (2) georeferencing and orthomosaicking (steps 3 to 10), and (3) horizontal accuracy assessment (step 11). Details on each step will be addressed in the following sub-sections: "Pre-Processing Stage (Steps 1 to 2)", "Photo-Alignment/Orthomosaicking Stage (Steps 3 to 10)", and "Horizontal Accuracy Assessment Stage (Step 11)". The data were processed with Intel Xeon CPU E5-2687W v3 at 3.10 GHz with 10-core, 128 GB RAM, 20 processors, AMD FirePro W7100 graphics card, and operating on Windows 10 64-bit.

Pre-Processing Stage (Steps 1 to 2)

As a preprocessing stage, input historical photos were masked (step 1) to eliminate unnecessary information such as frame and letters and then the image quality of these photos was estimated (step 2) based on the sharpness value of images that Agisoft image quality tool provides (Agisoft LLC 2019). A blurry image can reduce an orthophoto quality at the final step so images below 0.5 sharpness value out of 1.0 were discarded during the orthomosaicking process (step 10 in Figure 2). The quality test result of 1934 air photos ranges from 0.47 to 0.66 and two photos below the 0.5 quality threshold were disabled. Figure 3 represents an image quality comparison between 0.47 (A) and 0.66 (B) snapped in the same spatial extent. On the other hand, all 1951 air photos were used since they meet the requirement by ranging between 0.74 and 0.88.

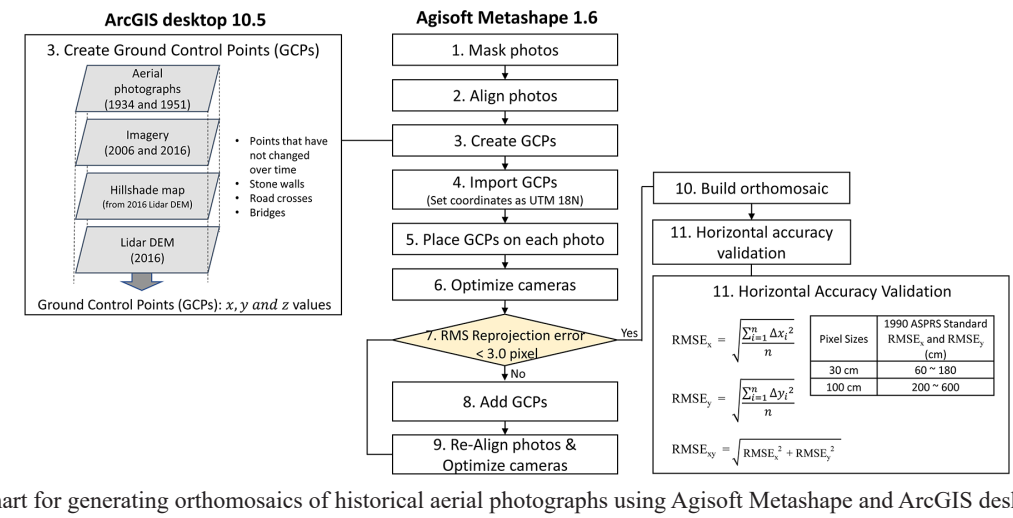

Figure 2. A flowchart for generating orthomosaics of historical aerial photographs using Agisoft Metashape and ArcGIS desktop. DEM = digital elevation model; RMSE = root-mean-square error.

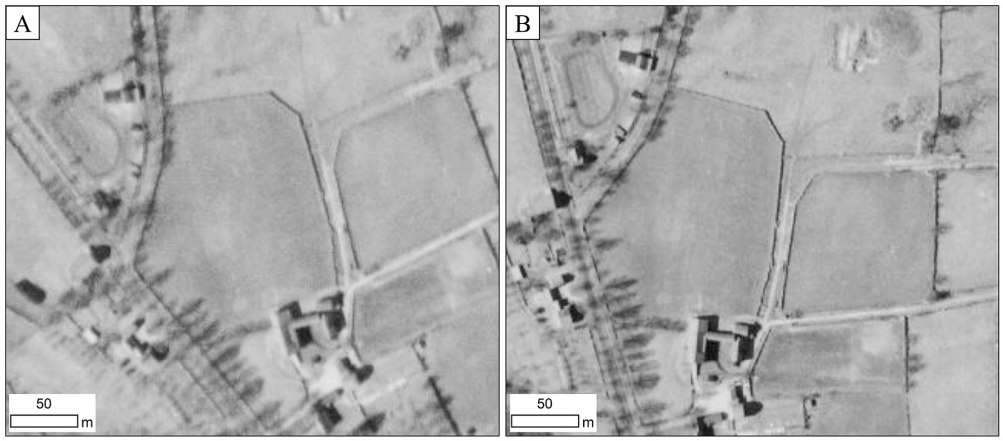

Figure 3. An image quality comparison between 0.50 (A) and 0.61 (B) snapped from 1934 air photos in the same spatial extent. 1934 Aerial Surveys, State Archives Record Group 089:011, State Archives, Connecticut State Library.

Photo-Alignment/Orthomosaicking Stage (Steps 3 to 10)

In this stage, photo-alignment (step 3) was conducted with high accuracy and the generic pair preselection option in Agisoft Metashape. The key point limit and tie point limit was set as 100 000 and 8000, respectively. Given that no information about camera position is used during the photo-alignment process, GCPs with northing, easting, and elevation values should be placed on photos to better alignment as well as georeferencing.

However, there are no GCPs available for historical data, so we defined GCPs (step 4) by selecting points that have not changed over time in a comparison of historical air photos, recent orthophotos, and lidar hillshade maps. Three aspects were taken into account when selecting GCPs. First, the priority of point selection was set considering frequency and stability of features through time. Therefore, stone walls were the first priority since they existed in the entire study area and were relatively stationary features pre-1934. Then it is followed by road crosses or edges, fixed structures (e.g., bridge, dam, etc.), and the attributes of natural landscape (e.g., creek crosses) (Figure 4). However, the attributes of natural landscape such as creek crosses can be relatively easily changed over time so it was only considered for GCP selection when the rest of potential features (e.g., stone walls, road crosses or edges, fixed structures) were unavailable.

The second aspect was the distribution of GCPs. Given that GCPs with three-dimensional (3D) coordinates strongly control error behavior (Wolf *et al.* 2014), the optimal distribution of GCPs is a point on each corner and additional points uniformly and densely distributed

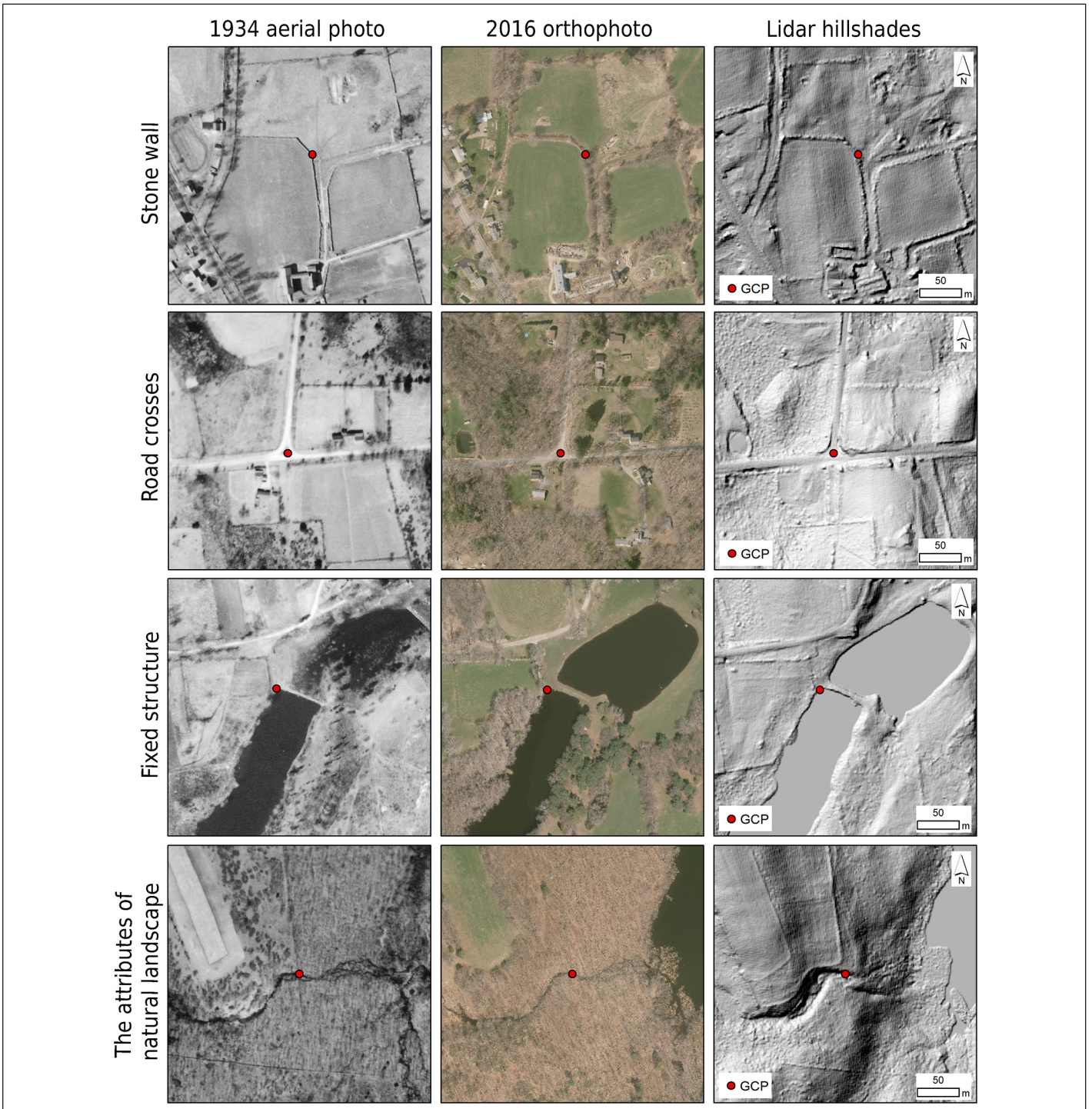

Figure 4. Examples of ground control points (GCPs) on 1934 aerial photo, 2016 orthophoto, and lidar hillshade. 1934 images from 1934 Aerial Surveys, State Archives Record Group 089:011, State Archives, Connecticut State Library.

throughout an image. We tried to place our GCPs as uniformly as possible but were limited by the fact that landscape changes between the images used are often not uniform. When using historical aerial photograph, with 50–90 years between original images and modern lidar and orthophoto data sets, this will likely also be a limitation contributing to error.

The last aspect was the number of photos that each GCP stitched. Each GCP should be located in the place where at least two photos were overlapped. Once GCPs are created at least 1:500 scale level through ArcGIS desktop, northing and easting values were extracted from created GCPs, and elevation values were extracted from lidar DEM (Llena *et al.* 2018) and exported as CSV format, herein we used UTM 18N projection (EPSG: 6347) since measuring horizontal distances was required in accuracy assessment (step 11). After creating GCPs, these GCPs were imported in Agisoft and placed on photos (step 5).

Steps 6 to 9 were repeated until RMS reprojection error was less than 3.0 pixels (see step 7). Camera optimization (step 6) was undertaken using Brown's distortion model (Agisoft LLC 2019) to adjust photo-alignment considering lens distortion. In particular, the following 11 variables were used; focal length (f), principal point offset (c_x and c_y), radial distortion coefficients (K_1, K_2, K_3, and K_4), affinity and skew transformation coefficients (B_1 and B_2), and tangential distortion coefficients (P_1 and P_2). This was an alternative way to overcome a lack of camera calibration information for historical imagery. The quality of photo alignment step is evaluated by RMS reprojection error (in pixel) that is a geometric error associated to the distance between a reconstructed 3D point and an original 3D point detected on the photo. If RMS reprojection error was greater than 3.0 pixel, more GCPs were created and placed on photo. If RMS reprojection error was less than 3.0 pixel, building an orthomosaic (step 10) was conducted. As stated in the description of step 2, images above 0.5 quality threshold were used during an orthomosaicking step and surface parameter was set as 1 m resolution lidar DEM instead of hDEM derived in Metashape due to low resolution of hDEM (e.g., 40 m). Then the orthophoto product was exported and assessed for horizontal accuracy (step 11).

Horizontal Accuracy Assessment Stage (Step 11)

To assess horizontal accuracy of the 1934 and 1951 orthophotos, check points (CPs) were placed on the photo to calculate the residual error of each point and the standard deviation of all residual errors (RMSE). Like GCPs, CPs were typically one of four types: (1) stone walls (SW), (2) road crosses and edges (Rd), (3) natural landscape feature (NL) (e.g., creek crosses), and (4) fixed structures (FS) (e.g., bridge, dam, etc.). In general, RMSE values (i.e., $RMSE_x$, $RMSE_y$, and $RMSE_{xy}$) of CPs are widely used to evaluate the quality of an orthophoto product (American Society for Photogrammetry and Remote Sensing 1990, 2014; Congalton and Green 2009; Tomaštík *et al.* 2019) since they are not used during photo-alignment process. In this study, they are calculated as:

$$\mathrm{RMSE}_x(m) = \sqrt{\frac{\sum_{i=1}^{n}(x_i - \hat{x}_i)}{n}} \quad (1)$$

$$\mathrm{RMSE}_y(m) = \sqrt{\frac{\sum_{i=1}^{n}(y_i - \hat{y}_i)}{n}} \quad (2)$$

$$\mathrm{RMSE}_{xy}(m) = \sqrt{\mathrm{RMSE}_x^{\,2} + \mathrm{RMSE}_y^{\,2}} \quad (3)$$

where:

x_i is the easting value of CPs from a lidar hillshade map; $\hat{x}_i$ is the estimated easting value of CPs in an orthomosaic product; y_i is the northing value of CPs from a lidar hillshade map; and $\hat{y}_i$ is the estimated northing value of CPs in an orthomosaic product.

The results of RMSE values were compared to American Society for Photogrammetry and Remote Sensing (ASPRS) 1990 standard shown in Table 2. Even though the 1990 standard is regarded as a legacy, we used this standard instead of the recent RMSE standard (e.g., less than 1.4 cm * resolution of geospatial data) given that our inputs were 1934 and 1951 historical data.

Table 2. ASPRS 1990 horizontal accuracy standard information including classes, RMSE values, and recommended uses for each class.

	1990 Standard $RMSE_x$ and $RMSE_y$ (m) based on pixel size		
Class	**1934**	**1951**	**Recommended Use**
1	0.6 m	2.0 m	Highest accuracy work
2	1.2 m	4.0 m	Standard mapping and GIS work
3	1.8 m	6.0 m	Visualization

ASPRS = American Society for Photogrammetry and Remote Sensing; RMSE = root-mean-square error; GIS = geographic information systems.

Results

By following all steps provided in the orthomosaicking workflow (Figure 2), two sets of historical orthomosaics were produced. One is 1934 orthoimage (ground resolution: 0.3 m/pixel) mosaicked with 141 photos covering 264 km² and the other is 1951 orthomosaic (ground resolution: 0.9 m/pixel) stitched with 68 photos covering 380 km². To meet RMS reprojection error condition (<3.0 pixel), 237 of GCPs was used for 1934 and 234 of GCPs was used for 1951. During the photo-alignment step, the total number of valid tie points for 1934 was 185 293 out of 474 139 and the RMS reprojection error was 2.93 pixel. After bundle adjustment, the mean residual errors of X, Y, Z, and total three coordinates for 1934 were 1.15 m, 1.26 m, 5.56 m, and 5.82 m, respectively. For 1951, the total number of valid tie points was 221 475 out of 464 127 and the RMS reprojection error of 1951 point cloud was 1.1 pixel. After bundle adjustment, the mean residual errors of X, Y, Z, and total three coordinates were 1.59 m, 1.54, 9.2 m, and 9.46 m. The bundle adjustment result shows that a large residual error in vertical value (Z) occurred compared to horizontal value (X and Y). This result supports the use of high-resolution lidar DEM as a better resource for the orthomosaicking process instead of the hDEM reconstructed from the historical aerial photographs.

Table 3 and Table 4 shows estimated distance and overlap information for the 1934 and 1951 results based on the estimated camera position by Metashape. The range of side overlap slightly changes depending on the north-south flight path; overall, the survey was flown as regular.

Table 3. Distance and overlap information between camera flight paths of 1934 aerial photographs. The lower case refers to the north-south flight path IDs shown in Figure 1.

1934 Camera Paths	**a–b**	**b–c**	**c–d**	**d–e**	**e–f**	**f–g**	**g–h**	**h–i**	**i–j**
Avg. overlap (km)	1.8	1.7	1.1	2.1	1.4	1.1	1.8	1.7	1.6
Max. overlap (km)	2	1.8	1.3	2.2	1.7	1.4	2.3	1.9	1.9
Min. overlap (km)	1.6	1.6	0.9	2	1	0.8	1.4	1.5	1.2
Side overlap (%)	35–47	35–40	54–67	27–35	41–62	51–73	24–55	45–37	41–60
Forward overlap (%)	45–60								

Table 4. Distance and overlap information between camera flight paths of 1951 aerial photographs. The upper case refers to the north-south flight path IDs shown in Figure 1.

1951 Camera Paths	**A–B**	**B–C**	**C–D**	**D–E**	**E–F**
Avg. overlap (km)	3.35	3.66	2.98	3.71	3.98
Min. overlap (km)	2.9	3.15	2.49	3.38	2.83
Max. overlap (km)	3.13	3.37	2.67	3.53	3.05
Side overlap (%)	28–33	21–25	39–40	19–25	29–36
Forward overlap (%)	60–80				

Horizontal accuracy assessment was then conducted to validate the quality of final orthophoto products by using RMSE values. To do this, a total of 287 CPs for the 1934 orthomosaic and 182 CPs for the 1951 orthomosaic were established for the accuracy evaluation. More CPs for the 1934 orthomosaic were required compared to those for the 1951 orthomosaic due to the number of CPs per image. In addition, the 1951 aerial photographs were taken during leaf-on conditions, which led to additional challenges associated with identifying reference objects that have not changed over and were not forested.

Table 5. RMSE results of 1934 and 1951 orthomosaics. *n* is the number of CPs.

	1934	1951
n	287	182
$RMSE_x$ (m)	0.94	1.28
$RMSE_y$ (m)	1.08	1.28
$RMSE_{xy}$ (m)	1.43	1.82
$RMSE_{xy}$ (m) without extreme outliers (>3 m)	0.83 (n = 277)	1.37 (n = 173)

RMSE = root-mean-square error; CPs = check points.

RMSE Results of 1934 and 1951 Orthomosaics

Table 5 shows the RMSE results of the 1934 and 1951 orthomosaics. According to the 1990 ASPRS horizontal accuracy standard (Table 2), the 1934 orthomosaic can be used for standard mapping and GIS work in that the RMSE result without outliers is less than 1.2 m and 1951 orthophoto products can be used for highest accuracy work considering the RMSE without outliers is less than 2.0 m (Table 5). It was found that high-resolution historical orthomosaics can be constructed to town-scale with high accuracy and the orthomosaic procedure can be further applied to expand the spatial scale of study area (i.e., state-scale).

Spatial Pattern of Residual Errors

Figure 5 shows the spatial distribution of residual errors of CPs regarding their location: inside and margin area. Figure 6 shows the residual error boxplots of each CPs for inside area and margin area in both 1934 and 1951 orthophoto results. The results demonstrate that (1) the mean residual errors of 1951 orthophoto are larger than those of 1934 orthoimage and this is caused by spatial resolution differences between two periods, (2) the residual errors from the margin area are larger than those from inside area, and (3) extreme outliers tend to be observed in edge part of the margin area. These results of (2) and (3) supported an edge effect reported in previous studies (Hung *et al.* 2019; Khan and Miklavcic 2019; Nogueira and Roberto 2017). It is partly due to the

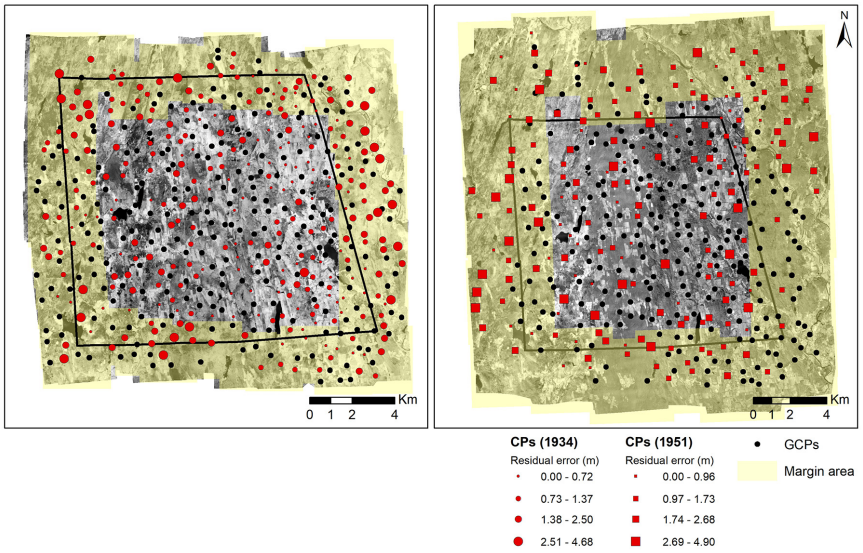

Figure 5. Spatial distribution of residual error from orthomosaic results (A: 1934; B: 1951). CPs = check points; GCPs = ground control points. 1934 Aerial Surveys, State Archives Record Group 089:011, and 1951 Aerial Surveys, State Archives Record Group 089:11b, State Archives, Connecticut State Library.

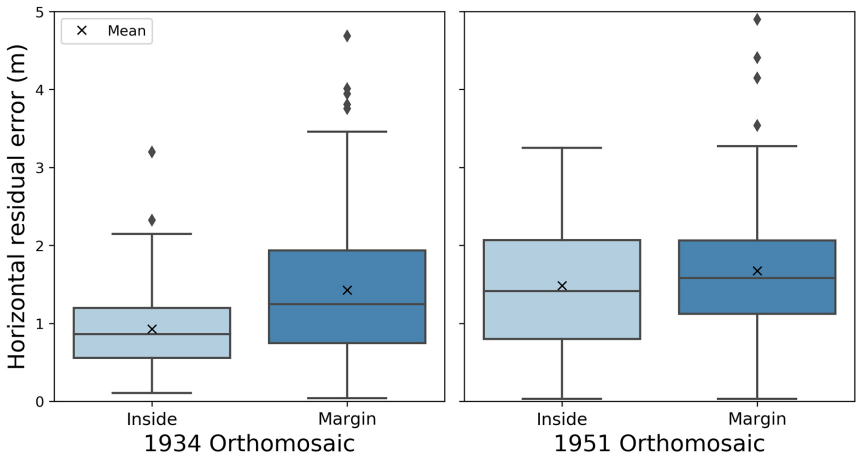

Figure 6. Boxplots of horizontal residual error (m) for inside area and margin area in 1934 (left), 1951 (right). (Ground resolution: 1934 orthomosaic (0.3 m/pixel) and 1951 orthomosaic (0.9 m/pixel)).

fact that the smaller number of key points were extracted and matched from limited images (e.g., two photos) in the margin area.

Discussion

As stated earlier, it was found that the accuracy of a historical orthomosaic can be affected by the spatial resolution of input photos and reference data, and their location (i.e., inside/margin). In other words, the conditions for obtaining high quality of orthomosaics are (1) to use high-resolution input photos (American Society for Photogrammetry and Remote Sensing 2014), (2) to extract reference points from high-resolution reference data such as lidar DEMs and hillshade, and (3) to use additional input photos by buffering a target area at least one flight strip surrounding it to minimize edge effect. However, the results (Figure 5) also demonstrate that a couple of major residual errors occur locally unlike an orthomosaics derived from modern UAV such as a drone. Therefore, we herein discussed additional factors influencing the quality of an orthomosaic from historical aerial photos over a broad area based on a spatial join between CPs' residual errors and map of each factor.

Types of CPs

As aforementioned in section "Horizontal Accuracy Assessment Stage (Step 11)", CPs fall into four types: SW, Rd, NL, and FS. The number of CPs categorized as SW or Rd accounts for ~80% since their locations are relatively easy to be identified between orthomosaic and lidar hillshade and are common landscape features that are static over time.

The occurrence of each CP was the close to the same for each time frame: for the 1934 orthomosaic, the number of CPs categorized as SW accounts for 56%, Rd is 22%, NL is 17%, and FS is 5%; for the 1951 orthomosaic, SW accounts for 53%, Rd is 24%, NL is 19% and FS is 4%. Figure 7 is a boxplot representing the distribution of residual error for each type of CP. CPs of SW and Rd are widely distributed throughout the orthomosaics and tend to show lower residual error compared to NL and FS—although it is difficult to generalize this result because the number of points for each type varies and the accuracy may depend on the location of points (e.g., inside/margin area). In addition, SW and Rd types were easily detectable and more easily delineated on the hillshade maps derived from high-resolution lidar DEM.

The Number of Tied Photos

The number of tied photos was considered as a second factor affecting the quality of orthomosaic because, theoretically, the more photos tied to specific reference points, the higher the accuracy of projected point placement (Agisoft LLC 2019). Figure 8 shows boxplots of CPs' residual errors according to the number of tied photos in 1934 and 1951 orthomosaics. Our results do not completely support the theoretical assumption. In the 1934 orthomosaic, mean residual error tends to decrease as the number of tied photos goes from 1 to 5, but in the 1951 orthomosaic, mean residual error does not decrease as the number of tied photos increases. This is likely due to the fact that it is difficult to place reference points in the exact same location in all photos because some photos have poor sharpness or bad conditions.

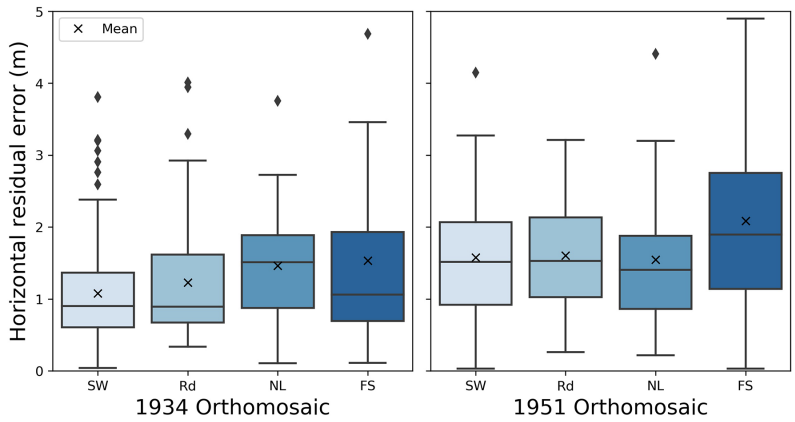

Figure 7. Residual error boxplots of four types of CPs in 1934 (left), 1951 (right). (SW = stone walls, Rd = road crosses or edges, NL = natural landscape features such as creek intersections, FS = fixed structures such as dams or bridges). (Ground resolution: 1934 orthomosaic (0.3 m/pixel) and 1951 orthomosaic (0.9 m/pixel).)

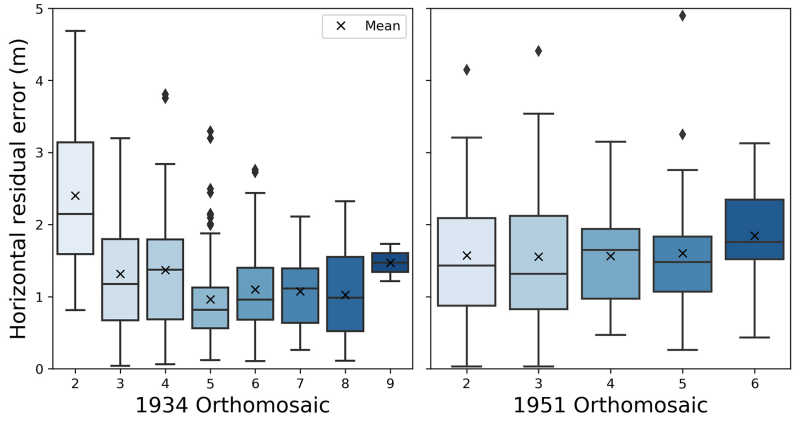

Figure 8. Residual error boxplots as a function of the number of tied photos used in 1934 (left) and 1951 (right). (Ground resolution: 1934 orthomosaic (0.3 m/pixel) and 1951 orthomosaic (0.9 m/pixel).)

Terrain

As the last factor that affects the accuracy of an orthomosaic result, three terrain elements (elevation, relief, and slope) were taken into account (Figure 9). Relief indicates the topographic range in elevation that exists over a specified window; we used a window size of 100 m. Elevation in the study area ranges from 64 m to 335 m, relief ranges from 0 to 71 m, and slope ranges between 0 to 40 degrees. From the perspective of spatial variation, the northwest portion of the study area shows the highest elevation, relief, and slope values. To figure out the relationship between terrain elements and positional accuracy of orthomosaic, each terrain element was reclassified into three classes, which are low (1), medium (2), and high (3) based on natural break and residual error boxplots of terrain conditions were created for both the 1934 and 1951 orthomosaic (Figure 10).

Mean positional residual error of historical orthomosaics increases slightly in areas characterized by higher elevations and higher slope values (Figure 10). One factor contributing to this trend is that fewer GCPs were used in areas with higher elevations and slope values because these areas tend to have high forest cover in our study area, which poses a challenge to identifying GCPs in lidar hillshades and historical aerial photographs. Therefore, it could be the coupling of terrain characteristics with vegetation differences, rather than strictly terrain, that prevents accurate matching of key points in the aerial photos and leads to larger residual errors.

Conclusion

This study presents a methodological procedure for generating high-resolution historical orthomosaic over a broad area using SfM software Agisoft Metashape and ArcGIS desktop, which allows for the incorporation of lidar data. Among 11 steps in the procedure, creating GCPs with lidar data is the most important step in order to align photos and build historical orthomosaics with high horizontal accuracy. We produced two town-scale high-resolution historical orhomosaics from different timeframes (1934 and 1951) that vary in terms of spatial resolution—1934 (0.3 m/pixel) and 1951 (0.9 m/pixel). In terms of

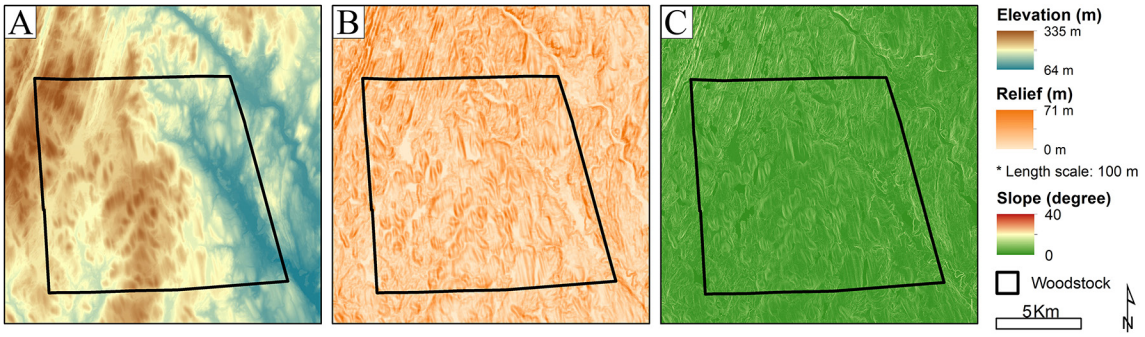

Figure 9. Map of three terrain elements (elevation, relief, and slope) in the study area.(A) elevation map; (B) relief map; (C) slope map.

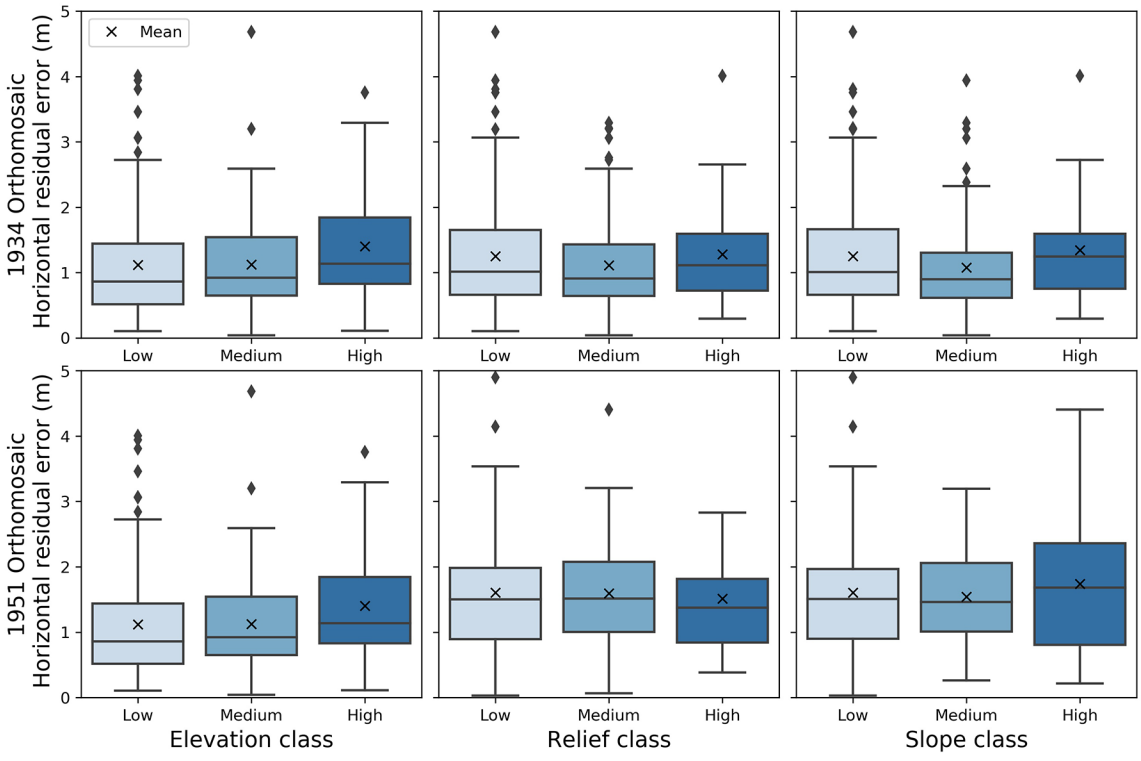

Figure 10. Residual error boxplots of three terrain elements (elevation, relief, and slope) reclassified into low, medium, and high classes based on a natural break. The top row shows the residual error results for the 1934 orthomosaic; the bottom row indicates that of the 1951 orthomosaic.

horizontal accuracy assessment, RMSE values without extreme outliers for both orthomosaics demonstrate they are highly accurate and can be used for standard mapping and GIS work according to 1990 ASPRS horizontal accuracy standard. In addition, the spatial distribution of CP residual errors indicates that an edge effect should be taken into account and enough photos should be included to cover at least one more edge layer larger than study area.

Moreover, we highlight that there are three factors influencing the quality of historical orthomosaics. First, it is important to use CPs not only extracted from high-resolution reference data such as lidar but also selected in terms of being stationary features through time and high frequency across the study area (e.g., stone walls and road crossings). Second, the number of tied photos can increase horizontal accuracy, but more tied photos do not always lead to higher accuracy because external causes such as image quality and stains on images prevent reference points being placed on the exact same locations. Lastly, it was found that the complexity of terrain can also affect the accuracy of orthomosaics.

Limitations to this study include the following: (1) the factors influencing the quality of historical orthomosaics were examined by a spatial join between the map of each factor and a map of CPs' residual errors such that it is not possible to examine the relationships amongst individual factors; (2) there may have been errors associated with orthomosaicking or accuracy assessments results due to digitization and imprecise locations of reference points on both photos and the map; and (3) it can be challenging to apply this method to completely forested areas where, in general, reference points are harder to come by.

Overall, despite these limitations, this contribution provides an important methodological procedure for making high-resolution, historical orthomosaics and for suggesting factors to be considered when applying this method. The procedure presented here can be applied to any study areas where historical aerial photographs and lidar data are available. Future application of this methodology would be to extend beyond the town scale considered here (e.g., 50–200 km²) all to the way to state scale or larger (10 000–100 000 km²), such as the state of Connecticut or the northeastern US in general. In addition to this, the outputs of our procedure can be used in various studies based on time-series analysis since the early to mid-20th century when historical aerial photographs become widely available, like detecting environmental disturbances, land use changes, and anthropogenic impacts. These products can also be used as input data for state-of-the-art deep learning algorithms to do image classification to reconstruct and analyze historical LULC.

Acknowledgments

This work was funded by a National Science Foundation grant BCS-1654462 to W. Ouimet. The authors wish to thank Katharine Johnson and Zhe Zhu for comments on an early draft of this contribution, and an anonymous reviewer for their helpful comments and suggestions.

References

Agisoft LLC. 2019. *Agisoft Metashape User Manual*. <https://www.agisoft.com/pdf/metashape-pro_1_5_en.pdf>.

Ajayi, O. G., A. A. Salubi, A. F. Angbas and M. G. Odigure. 2017. Generation of accurate digital elevation models from UAV acquired low percentage overlapping images. *International Journal of Remote Sensing* 38(8–10):3113–3134.

American Society for Photogrammetry and Remote Sensing. 1990. ASPRS accuracy standards for large-scale maps. *Photogrammetric Engineering & Remote Sensing* 56(7):1068–1070.

American Society for Photogrammetry and Remote Sensing. 2014. ASPRS positional accuracy standards for digital geospatial data, edition 1, version 1.0. *Photogrammetric Engineering & Remote Sensing* 81(3):1–26.

Arnaud, F., H. Piégay, L. Schmitt, A. J. Rollet, V. Ferrier and D. Béal. 2015. Historical geomorphic analysis (1932–2011) of a by-passed river reach in process-based restoration perspectives: the Old Rhine downstream of the Kembs Diversion Dam (France, Germany). *Geomorphology* 236:163–177.

Baker, W. L., J. J. Honaker and P. J. Weisberg. 1995. Using aerial photography and GIS to map the forest-tundra ecotone in Rocky Mountain National Park, Colorado, for global change research. *Photogrammetric Engineering and Remote Sensing* 61(3):313–320.

Bolstad, P. V. 1992. Geometric errors in natural resource GIS data: Tilt and terrain effects in aerial photographs. *Forest Science* 38(2):367–380.

Capitol Region Council of Governments (CRCoG). 2016. 2016 Aerial Imagery. <http://cteco.uconn.edu/data/flight2016/index.htm> Accessed on 29 July 2021.

Child, S. F., L. A. Stearns, L. Girod and H. H. Brecher. 2021. Structure-from-motion photogrammetry of antarctic historical aerial photographs in conjunction with ground control derived from satellite data. *Remote Sensing* 13(1):1–25.

Comiti, F., M. Da Canal, N. Surian, L. Mao, L. Picco and M. A. Lenzi. 2011. Channel adjustments and vegetation cover dynamics in a large gravel bed river over the last 200 years. *Geomorphology* 125(1):147–159.

Congalton, R. G. and K. Green. 2009. The photogrammetric record. In *Assessing the Accuracy of Remotely Sensed Data: Principles and Practices,* 2d ed. Boca Raton, Fla.: CRC Press.

Connecticut State Library. 1934. *1934 Aerial Surveys*. Record Group 089:011. College Park, Md.: Department of Transportation, State Archives.

Connecticut State Library. 1951. *1951 Aerial Surveys*. Record Group 089:011b. College Park, Md.: Department of Transportation, State Archives.

Cronon, W. 1983. *Changes in the Land: Indians, Colonists, and the Ecology of New England*. New York: Hill and Wang.

CT Environmental Conditions Online (CT ECO). 2012. 2012 Aerial Imagery. <http://cteco.uconn.edu/help/info_orthos2012.htm> Accessed on 29 July 2021.

ESRI. 2012. "World Topographic Map". 1:100 000. <http://www.arcgis.com/home/item.html?id=30e5fe3149c34df1ba922e6f5bbf808f> Accessed on 29 July 2021.

Fox, A. J. and A. Cziferszky. 2008. Unlocking the time capsule of historic aerial photography to measure changes in antarctic peninsula glaciers. *Photogrammetric Record* 23(121):51–68.

Frankl, A., V. Seghers, C. Stal, P. De Maeyer, G. Petrie and J. Nyssen. 2015. Using image-based modelling (SfM–MVS) to produce a 1935 orthomosaic of the Ethiopian highlands. *International Journal of Digital Earth* 8(5):421–430.

Gennaretti, F., M. N. Ripa, F. Gobattoni, L. Boccia and R. Pelorosso. 2011. A methodology proposal for land cover change analysis using historical aerial photos. *Journal of Geography and Regional Planning* 4(9):542–556.

Geyman, E. C., W. van Pelt, A. C. Maloof, H. F. Aas and J. Kohler. 2022. Historical glacier change on Svalbard predicts doubling of mass loss by 2100. *Nature* 601.

Gomez, C. 2014. Digital photogrammetry and GIS-based analysis of the bio-geomorphological evolution of Sakurajima Volcano, diachronic analysis from 1947 to 2006. *Journal of Volcanology and Geothermal Research* 280:1–13.

Hung, I.-K., D. Unger, D. Kulhavy and Y. Zhang. 2019. Positional precision analysis of orthomosaics derived from drone captured aerial imagery. *Drones* 3(2):46.

Johnson, K. M. and W. B. Ouimet. 2014. Rediscovering the lost archaeological landscape of southern New England using airborne light detection and ranging (LiDAR). *Journal of Archaeological Science* 43(1):9–20.

Johnson, K. M. and W. B. Ouimet. 2016. Physical properties and spatial controls of stone walls in the northeastern USA: Implications for anthropocene studies of 17th to early 20th century agriculture. *Anthropocene* 15:22–36.

Kadmon, R. and R. Harari-Kremer. 1999. Studying long-term vegetation dynamics using digital processing of historical aerial photographs. *Remote Sensing of Environment* 68:164–176.

Khan, Z. and S. J. Miklavcic. 2019. An automatic field plot extraction method from aerial orthomosaic images. *Frontiers in Plant Science* 10(May):1–13.

Leh, M., S. Bajwa and I. Chaubey. 2013. Impact of land use change on erosion risk: An integrated remote sensing, geographic information system and modeling methodology. *Land Degradation and Development* 421(2011):409–421.

Lingua, A., D. Marenchino and F. Nex. 2009. Performance analysis of the SIFT operator for automatic feature extraction and matching in photogrammetric applications. *Sensors* 9(5):3745–3766.

Llena, M., M. Cavalli, D. Vericat and S. Crema. 2018. Assessing landscape changes associated to anthropic disturbances by means of the application of structure from motion photogrammetry using historical aerial imagery. *Rendiconti Online Societa Geologica Italiana* 46(May):74–81.

Mallinis, G., D. Emmanoloudis, V. Giannakopoulos, F. Maris and N. Koutsias. 2011. Mapping and interpreting historical land cover/land use changes in a natura 2000 site using Earth observational data: The case of Nestos Delta, Greece. *Applied Geography* 31(1):312–320.

Marignani, M., D. Rocchini, D. Torri, A. Chiarucci and S. Maccherini. 2008. Planning restoration in a cultural landscape in Italy using an object-based approach and historical analysis. *Landscape and Urban Planning* 84(1):28–37.

Maurer, J. and S. Rupper. 2015. Tapping into the hexagon spy imagery database: A new automated pipeline for geomorphic change detection. *ISPRS Journal of Photogrammetry and Remote Sensing* 108:113–127.

Midgley, N. G. and T. N. Tonkin. 2017. Reconstruction of former glacier surface topography from archive oblique aerial images. *Geomorphology* 282:18–26.

National Research Council. 2001. Grand challenges in environmental sciences. In *Grand Challenges in Environmental Sciences*. Washington, DC: The National Academies Press.

Nebiker, S., N. Lack and M. Deuber. 2014. Building change detection from historical aerial photographs using dense image matching and object-based image analysis. *Remote Sensing* 6(9):8310–8336.

Nita, M. D., C. Munteanu, G. Gutman, I. V. Abrudan and V. C. Radeloff. 2018. Widespread forest cutting in the aftermath of World War II captured by broad-scale historical corona spy satellite photography. *Remote Sensing of Environment* 204:322–332.

Nogueira, F. C. and L. Roberto. 2017. Accuracy analysis of orthomosaic and DSM produced from sensor aboard UAV. In *XVIII Simpósio Brasileiro de Sensoriamento Remoto—SBSR*, 5515–5522.

Riquelme, A., M. Del Soldato, R. Tomás, M. Cano, L. Jordá Bordehore and S. Moretti. 2019. Digital landform reconstruction using old and recent open access digital aerial photos. *Geomorphology* 329:206–223.

Rocchini, D., G.L.W. Perry, M. Salerno, S. Maccherini and A. Chiarucci. 2006. Landscape change and the dynamics of open formations in a natural reserve. *Landscape and Urban Planning* 77(1–2):167–77.

Sevara, C. 2013. Top secret topographies: Recovering two and three-dimensional archaeological information from historic reconnaissance datasets using image-based modelling techniques. *International Journal of Heritage in the Digital Era* 2(3):395–418.

Thorson, R. M. 2002. *Stone by Stone : The Magnificent History in New England's Stone Walls*. New York, N.Y. : Walker & Company.

Tomaštík, J., M. Mokroš, P. Surový, A. Grznárová and J. Merganič. 2019. UAV RTK/PPK method—An optimal solution for mapping inaccessible forested areas? *Remote Sensing* 11(6):721.

Turner, D., A. Lucieer and C. Watson. 2012. An automated technique for generating georectified mosaics from ultra-high resolution unmanned aerial vehicle (UAV) imagery, based on structure from motion (SFM) point clouds. *Remote Sensing* 4(5):1392–1410.

Verbesselt, J., A. Zeileis and M. Herold. 2012. Near real-time disturbance detection using satellite image time series. *Remote Sensing of Environment* 123:98–108.

Verhoeven, G., M. Doneus, C. Briese and F. Vermeulen. 2012. Mapping by matching: A computer vision-based approach to fast and accurate georeferencing of archaeological aerial photographs. *Journal of Archaeological Science* 39(7):2060–2070.

Weng, J., T. S. Huang and N. Ahuja. 2013. *Motion and Structure from Image Sequences*. Berlin/Heidelberg, Germany: Springer Science & Business Media.

Wolf, P. R., B. A. Dewitt and B. E. Wilkinson. 2014. *Elements of Photogrammetry with Applications in GIS,* 4th ed. Columbus, Ohio: McGraw-Hill Education.

Zhu, Z. and C. E. Woodcock. 2014. Continuous change detection and classification of land cover using all available landsat data. *Remote Sensing of Environment* 144:152–171.

Zhu, Z., Y. Fu, C. E.Woodcock, P. Olofsson, J. E.Vogelmann, C. Holden, M. Wang, S. Dai and Y. Yu. 2016. Including land cover change in analysis of greenness trends using all available Landsat 5, 7, and 8 images: A case study from Guangzhou, China (2000–2014). *Remote Sensing of Environment* 185:243–257.

Zhu, Z., J. Zhang, Z. Yang, A. H. Aljaddani, W. B. Cohen, S. Qiu and C. Zhou. 2020. Continuous monitoring of land disturbance based on Landsat time series. *Remote Sensing of Environment* 238:111116.

Zomeni, M., J. Tzanopoulos and J. D. Pantis. 2008. Historical analysis of landscape change using remote sensing techniques: An explanatory tool for agricultural transformation in Greek rural areas. *Landscape and Urban Planning* 86(1):38–46.

IN-PRESS ARTICLES

Jordan Bowman, Lexie Yang, Orrin Thomas, Jerry Kirk, Andrew Duncan, David Hughes, and Shannon Meade. UAS Edge Computing of Energy Infrastructure Damage Assessment.

Firat Erdem, Nuri Erkin Ocer, Dilek Kucuk Matci, Gordana Kaplan, and Ugur Avdan. Apricot Tree Detection from UAV-Images Using Mask R-CNN and U-Net.

Batuhan Sariturk, Damla Kumbasar, and Dursun Zafer Seker. Comparative Analysis of Different CNN Models for Building Segmentation from Satellite and UAV Images.

Rabi N. Sahoo, Shalini Gakhar, R.G. Rejith, Rajeev Ranjan, Mahesh C. Meena, Abir Dey, Joydeep Mukherjee, Rajkumar Dhakar, Sunny Arya, Anchal Daas, Subhash Babu, Pravin K. Upadhyay, Kapila Sekhawat, Sudhir Kumar, Mahesh Kumar, Viswanathan Chinnusamy, and Manoj Khanna. Unmanned Aerial Vehicle (UAV)–Based Imaging Spectroscopy for Predicting Wheat Leaf Nitrogen.

Yunus Kaya, Halil İbrahim Şenol, Abdurahman Yasin Yiğit, and Murat Yakar. Car Detection from Very High-Resolution UAV Images Using Deep Learning Algorithms.

Xin Jia, Qing Zhu, Xuming Ge, Ruifeng Ma, Daiwei Zhang, and Tao Liu. Robust Guardrail Instantiation and Trajectory Optimization of Complex Highways Based on Mobile Laser Scanning Point Clouds.

Shuanggen Jin, Ayman M.Elameen, Daniel Olago. Identification of drought events in major basins of Africa based on weighted water storage deficit index from GRACE measurements.

Xin Jia, Qing Zhu, Xuming Ge, Ruifeng Ma, Daiwei Zhang, and Tao Liu. Robust Guardrail Instantiation and Trajectory Optimization of Complex Highways Based on Mobile Laser Scanning Point Clouds.

Zhikang Lin, Wei Liu, Yulong Wang, Yan Xu, Chaoyang Niu. Change Detection in SAR Images through Clustering Fusion Algorithm and Deep Neural Networks.

Dan Li, Hanjie Wu, Yujian Wang, Xiaojun Li, Fanqiang Kong, and Qiang Wang. Lightweight Parallel Octave Convolutional Neural Network for Hyperspectral Image Classification.

Tolga Bakirman, Bahadir Kulavuz, and Bulent Bayram. Use of Artificial Intelligence Toward Climate-Neutral Cultural Heritage.

The Cellular Automata Approach in Dynamic Modelling of Land Use Change Detection and Future Simulations Based on Remote Sensing Data in Lahore Pakistan

Muhammad Nasar Ahmad, Zhenfeng Shao, Akib Javed, Fakhrul Islam, Hafiz Haroon Ahmad, and Rana Waqar Aslam

Abstract

Rapid urbanization has become an immense problem in Lahore city, causing various socio-economic and environmental problems. Therefore, it is noteworthy to monitor land use/land cover (LULC) change detection and future LULC patterns in Lahore. The present study focuses on evaluating the current extent and modeling the future LULC developments in Lahore, Pakistan. Therefore, the semi-automatic classification model has been applied for the classification of Landsat satellite imagery from 2000 to 2020. And the Modules of Land Use Change Evaluation (MOLUSCE) cellular automata (CA-ANN) model was implemented to simulate future land use trends for the years 2030 and 2040. This study project made use of Landsat, Shuttle Radar Topography Mission Digital Elevation Model, and vector data. The research methodology includes three main steps: (i) semi-automatic land use classification using Landsat data from 2000 to 2020; (ii) future land use prediction using the CA-ANN (MOLUSCE) model; and (iii) monitoring change detection and interpretation of results. The research findings indicated that there was a rise in urban areas and a decline in vegetation, barren land, and water bodies for both the past and future projections. The results also revealed that about 27.41% of the urban area has been increased from 2000 to 2020 with a decrease of 42.13% in vegetation, 2.3% in barren land, and 6.51% in water bodies, respectively. The urban area is also expected to grow by 23.15% between 2020 and 2040, whereas vegetation, barren land, and water bodies will all decline by 28.05%, 1.8%, and 12.31%, respectively. Results can also aid in the long-term, sustainable planning of the city. It was also observed that the majority of the city's urban area expansion was found to have occurred in the city's eastern and southern regions. This research also suggests that decision-makers and municipal Government should reconsider city expansion strategies. Moreover, the future city master plans of 2050 must emphasize the relevance of rooftop urban planting and natural resource conservation.

Introduction

Land use describes how people use the land, while land cover refers to the characteristics of the surface materials. Rapid transformation in land use/land cover (LULC) affects the human environment (Guidigan *et al.* 2019; Hou *et al.* 2020) and ecosystem services (Chen *et al.* 2021; Huang *et al.* 2019). Over the past two decades, LULC change detection has drawn a lot of attention from researchers. Land use/land cover is primarily expedited by the construction of artificial infrastructure (Girma *et al.* 2022; Zhu *et al.* 2022). Therefore, significant change in LULC has been influenced by rapid urbanization (Li *et al.* 2019; Naikoo *et al.* 2022) and population growth all over the world. As a result of rapid urbanization and infrastructure development, mostly vegetation and water bodies have changed into urban centers (Dewan and Yamaguchi 2009; Hassan 2017). By 2050, it is projected that the metropolitan sectors will increase by 66% (Marondedze and Schütt 2021; Ullah *et al.* 2019).

There are several key issues driven by LULC change which are: increase in land surface temperature, haze, smog, vegetation loss, increase in impervious surface (Nath *et al.* 2021), environmental uncertainties, CO_2 emissions (Bhattacharjee and Chen 2020; Zhou *et al.* 2021), water degradation, and urban flooding. In the cities, a high proportion of vegetation cover is converted into impervious surfaces due to recent metropolitan expansions. Therefore, for a better knowledge of prior research on LULC, it is important to monitor existing trends and the future trajectory of LULC detection.

Remote sensing (Sohl and Sleeter 2012) combined with geo-information science has provided a new corridor for researchers to conduct studies related to urban development. Advancements in remote sensing technologies such as machine learning and artificial intelligence technologies (Abbas *et al.* 2021; Hamedianfar *et al.* 2020; Talukdar *et al.* 2020) are providing prompt and reliable results. There are numerous prediction models adopted by researchers (Ghalehteimouri *et al.* 2022; Zhang *et al.* 2022), such as Markov Chain, Artificial Neural Network (ANN), and cellular automata (CA). The cellular automata model is used more extensively to simulate future LULC change as it uses historical LULC data (Akbar *et al.* 2019; Guidigan *et al.* 2019) with independent variables to strengthen the prediction results. Cellular automata is a well-known and well-adopted artificial intelligence modeling technique (Al-Darwish *et al.* 2018). The CA model operates in such a manner that it computes cells automatically based on transitional rules and algorithm equations, and it simulates complex systems such as city expansion dynamics (Khan *et al.* 2022; Shafizadeh-Moghadam *et al.* 2021; Zhang and Wang 2021).

This research work was conducted based on CA and ANN algorithms using the Modules for Land-use Change Evaluation (MOLUSCE) model. Moreover, the machine learning-based model of semi-automatic classification (SCP) is used for land-use classification. MOLUSCE uses Markov chain analysis and cellular automata methods (Aneesha Satya *et al.* 2020) to determine the land-use dynamics.

Muhammad Nasar Ahmad, Zhenfeng Shao, Akib Javed, and Rana Waqar Aslam are with the State Key Laboratory of Information Engineering in Surveying, Mapping and Remote Sensing, Wuhan University, Wuhan 430079, China (mnasarahmad@whu.edu.cn).

Fakhrul Islam is with Khushal Khan Khattak University, Karak, Khyber Pakhtunkhwa, Pakistan.

Hafiz Haroon Ahmad is with the School of Space and Earth Sciences, University of Science and Technology of China, Hefei, Anhui, 230026, China.

Contributed by Prasad S. Thenkabail, July 19, 2022 (sent for review August 21, 2022; reviewed by Agnes Begue, Bingqing Liang).

Photogrammetric Engineering & Remote Sensing
Vol. 89, No. 1, January 2023, pp. 47–55.
0099-1112/22/47–55

doi: 10.14358/PERS.22-00102R2

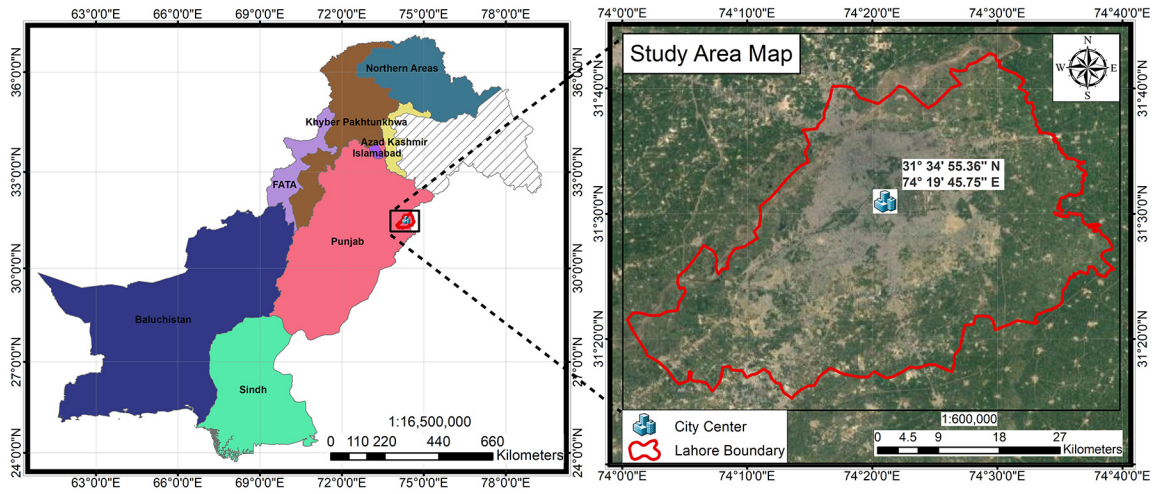

Figure 1. Location of the study area on the map.

Table 1. Satellite data set used in this study.

No.	Sensor ID	Sensor Type	Acquisition Date	Row/Path	Spatial Resolution
1	LT05149038200003110 1T1	TM	11-03-2000	149/038	30 m
2	LT05149038201003060 1T1	TM	07-03-2010	149/038	30 m
3	LC08149038202002150 1RT	OLI/TIRS	15-02-2020	149/038	30 m
4	SRTM DEM	ASTER-V3	23-09-2014	N31/E074	30 m

Source: NASA/USGS-Earth Explorer (https://earthexplorer.usgs.gov/).
TM = Thematic Mapper; OLI = Operational Land Imager; TIRS = Thermal Infrared Sensor; SRTM DEM = Shuttle Radar Topography Mission Digital Elevation Model.

Lahore has experienced a significant transformation in LULC (Fahad *et al.* 2021). Such rapidly growing cities need to simulate future LULC prediction modeling. In recent decades, Lahore's development progress has resulted in serious environmental problems (Jabbar and Yusoff 2022), such as high land surface temperature and smog formation (Farid *et al.* 2022). Lahore ranked second in the most populated cities in 2021 (Jabeen *et al.* 2022) and recorded the 453 highest air quality index. In terms of LULC change, Lahore is one of Pakistan's fastest-growing metropolitan cities. In the past, many studies have been conducted by researchers for the planning and development (Hong 2022; Hussain and Nadeem 2021; Zhang *et al.* 2019) of Lahore. According to statistics, Lahore's per capita water supply has fallen from 5600 cubic meters to 1038 cubic meters (Zhang *et al.* 2021) and the availability has been recorded at about 877 cubic meters in 2020. Although the city is confronted with several obstacles, such as a lack of urban development policies, an exploding population, and an energy crisis.

This research aims to evaluate the present LULC mapping for the years 2000, 2010, and 2020. And to simulate future LULC patterns for the years 2030 and 2040, respectively. There are two key objectives of this research work (i) LULC change detection and future simulations in Lahore and (ii) implementation of SCP semi-automatic classification model and CA-ANN simulation algorithm. Another aim of this research was to determine the efficiency of machine learning algorithms for LULC change recognition and future simulations. In recent studies, a variety of methods have been used to access LULC transformations. But in this research, the authors have implemented the SCP plugin combined with MOLUSCE-CA models to investigate LULC in Lahore. The use of these machine learning models can also help to develop applications for land use planning and vertical infrastructure development plan. It will be useful for policymakers and future research, because Lahore is the capital city of the Punjab Province.

Study Area

Lahore is the second major city in terms of population and the capital of the province. Lahore has a population of around 12 642 000 people and is located in the northeast region of Punjab, Pakistan. It has a spatial location of 31° 34' 55.36" N latitude and 74° 19' 45.75" E longitude. Lahore has an area coverage of approximately 1772 sq. km. with 217 meters of altitude above mean sea level. The location of the study area on the map is shown below in Figure 1.

Table 2. Details of vector data set used in this study.

No.	Name	Datum	Coordinate System
1	Country and City Boundary	D_WGS_1984	UTM_Zone_43N
2	Roads	D_WGS_1984	UTM_Zone_43N
3	Waterways	D_WGS_1984	UTM_Zone_43N
4	River	D_WGS_1984	UTM_Zone_43N

Source: Lahore Development Authority (https://www.lda.gop.pk).

The city has developed in a horizontal direction, and it consists of a walled city adjacent to urban and residential areas. The city has grown as a technological center, with significant commercial, industrial, and trade prospects. Lahore is the urban center of the province and has been converted to other land-use developments in the last three decades because of rapid urbanization. Lahore experiences semi-arid weather (Bakker *et al.* 2022), with little rainfall to support a humid subtropical climate. In terms of the economy, with an expected average growth rate of 5.6 percent as of 2008, the city's gross domestic product was estimated to be $40 billion (Bakker *et al.* 2022). When compared to Karachi, the economic hub of Pakistan, Lahore's economy ($78 billion in 2008) is 51% larger while having only half the population of Karachi. Lahore experiences semi-arid weather (Bakker *et al.* 2022), with little rainfall to support a humid subtropical climate.

Materials and Methods

Satellite Imagery and Vector Data Set

In this research, both satellite imagery and vector data sets are used and subsequently processed to carry out the overall analysis. Table 1 and Table 2 show the satellite and vector data sets used in this study.

Data Flow Diagram and Methodology

Multiple Landsat satellite data products were obtained from the USGS website using the EarthExplorer platform. Details of the data set such as scene ID, sensors, and path/row are explained in Table 1. Landsat

data for the Lahore district was downloaded over a 10 year period from 2000 to 2020. Landsat 5 Thematic Mapper (TM) was used for both 2000 and 2010, which were acquired in March, while Landsat 8 Operational Land Imager (OLI) was used for 2020, also acquired in January. For each Landsat product, cloud coverage was adjusted to less than 15% to improve the precision of data processing for more accurate LULC change detection. Similarly, Shuttle Radar Topography Mission Digital Elevation Model (SRTM DEM) (version 3) was also downloaded from the United States Geological Survey (USGS) website and used as an independent variable in this research. Figure 2 illustrates the overall data flow diagram for this study.

Furthermore, all the satellite data, including satellite imagery and DEM, was then clipped using the vector boundary of the Lahore district. The LULC simulation model incorporated additional three spatial variables with classified maps for more precise future simulation. For this purpose, roads, waterways, and water bodies data were obtained from the local government sectors and Lahore Development Authority. These spatial layers were used as dependent factors in the cellular automata model.

Semi-Automatic Classification Module

There are numerous image processing applications including Erdas Imagine, Envi, Catalyst, Geomatica, and ArcGIS that have been used by previous studies. In this research, a SCP tool in QGIS was applied for both LULC classifications. The SCP Plugin is an open-source plugin in QGIS (Tempa and Aryal 2022) that facilitates semi-automated classification using remote sensing data in both supervised and unsupervised modules (De Lotto *et al.* 2022). The SCP is a comprehensive tool, especially for land-use land cover mapping and classification. SCP enables the use of several classification algorithms (Congedo 2021) based on a range of satellite images such as Moderate Resolution Imaging. Spectroradiometer (MODIS), Landsat, or S2 (*Sentinel-I*, *Sentinel-II*). Furthermore, it provides various tools for pre-processing of images such as downloading satellite data and radiometric corrections, (Islam *et al.* 2021; Maung and Sasaki 2021; Riad *et al.* 2020). Similarly, SCP allows postprocessing tasks including merging of classes, accuracy assessment, and conversion from a classified raster to vector format.

In the preprocessing module, SCP automatically converts satellite bands from their digital number values to reflectance. It also provides an

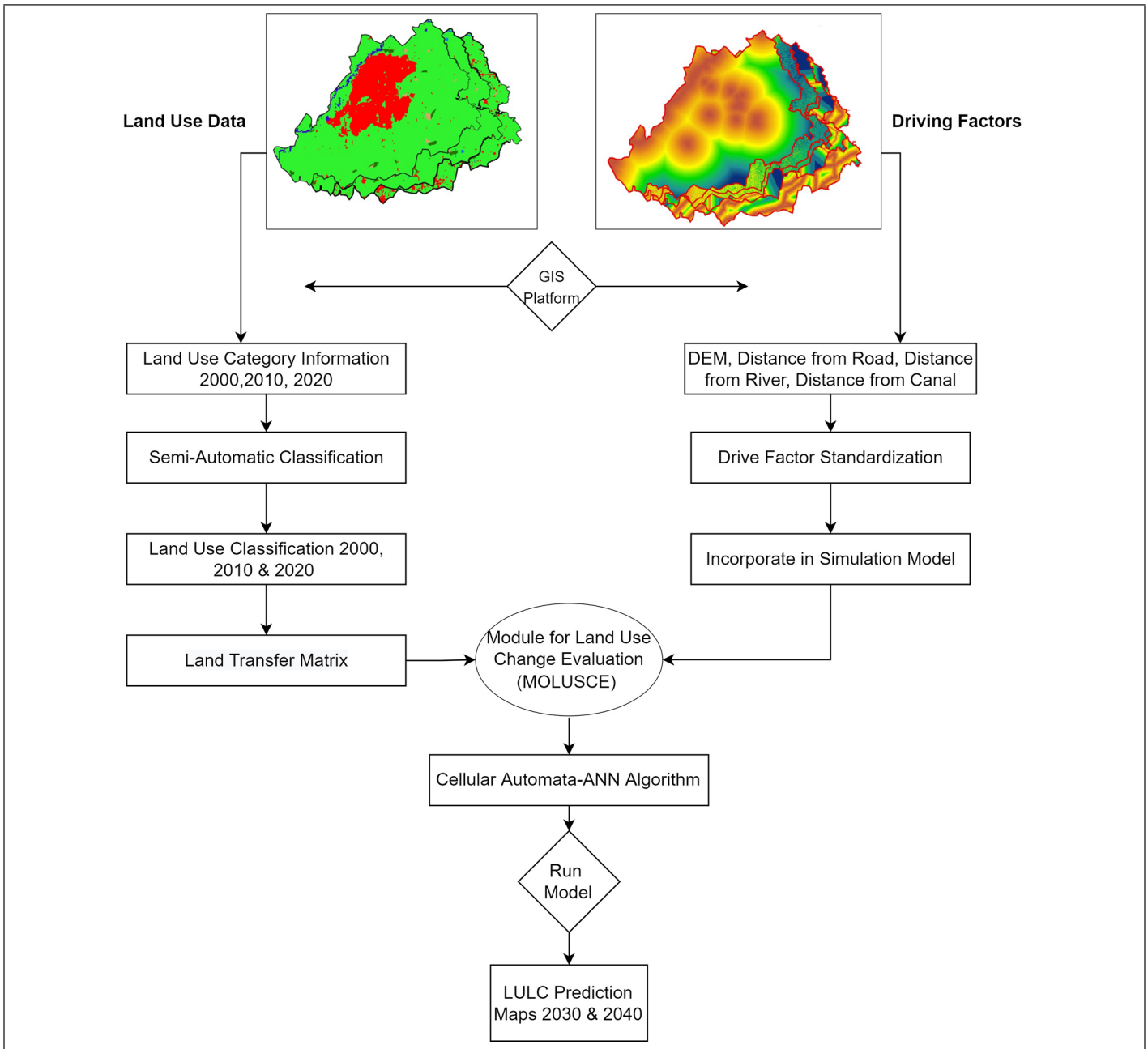

Figure 2. Overall workflow diagram.

automatic Dark Object Subtraction1 machine-learning algorithm to find the darkest pixel value in each band for atmospheric corrections. The semi-automatic classification image processing approach identifies components in an image based on their spectral signatures. The supervised classification often needs the user to pick one or more regions of interest (ROI) also known as training areas for each land-use class. Generally, in SCP, a Region Growing Algorithm is used for training area selection. The spectral distance between adjacent pixels is used by the region growing algorithm to choose pixels that are spectrally comparable.

There are several classification algorithms that are available in SCP, including (i) Minimum Distance, (ii) Maximum Likelihood, (iii) Spectral Angle Mapper, (iv) Parallelepiped Classification, (v) Land Cover Signature Classification, and (vi) Algorithm raster. However, for LULC classification, the Spectral Angle Mapper (SAM) algorithm (Christovam *et al.* 2019; Verma *et al.* 2020) is most commonly used, and it also efficiently processes multispectral satellite data. The SAM classifier is based on identifying pixel spectral value through its angular information (Hoque *et al.* 2022; Nappo *et al.* 2021). It actually calculates the angle between pixel spectral signatures and training signatures provided by the classifier user.

Methods of Land-use Change Evaluation Simulations

In this study, the MOLUSE simulation model has been applied for LUCL prediction for 2030 and 2040 in the Lahore district. MOLUSCE is an open-source tool used for land-use change simulations (Hossain *et al.* 2022). It includes well-known methods that may be applied to LULC analysis (Muhammad *et al.* 2022). There are several algorithms that are present in MOLUSCE for creating transition potential maps (Baig *et al.* 2022; Rehman *et al.* 2022), including cellular automata-artificial neural networks (CA-ANN), weights of evidence, logistic regression, and Multi-Criteria Evaluation (Kamaraj and Rangarajan 2022).

Cellular automata is a well-known and significant modeling technique (Hu *et al.* 2022; Mwabumba *et al.* 2022) uses machine learning methods. Many researchers (Abdullah *et al.* 2022; Kafy *et al.* 2021; Mohammad *et al.* 2022; Tolentino and Galo 2021) describe that artificial neural networks (CA-ANN) algorithms can provide more efficient results for land use/cover change analysis. Figure 3 illustrates the main steps involved in running the land-use change evaluation model. In this research, we have implemented a cellular automata-based artificial neural network to simulate LULC maps. For the generation of prediction maps, we used classified maps of 2000, 2010, and 2020 as input for the prediction of 2030. Similarly, we used the 2020 and 2030 classified maps as input for the 2040 prediction map.

Classification Methods and Techniques

The classification process was performed using the SCP plugin in QGIS. As SCP allows the download of seven satellite data products (Tempa and Aryal 2022) such as Landsat, Sentinel-1, Sentinel-2, Sentinel-3, ASTER satellite images, MODIS, and GOES. In this research, for the year 2000, Landsat 4-5 satellite imagery was collected, while *Landsat 8* imagery was used through SCP for the years 2010 and 2020. In the classification

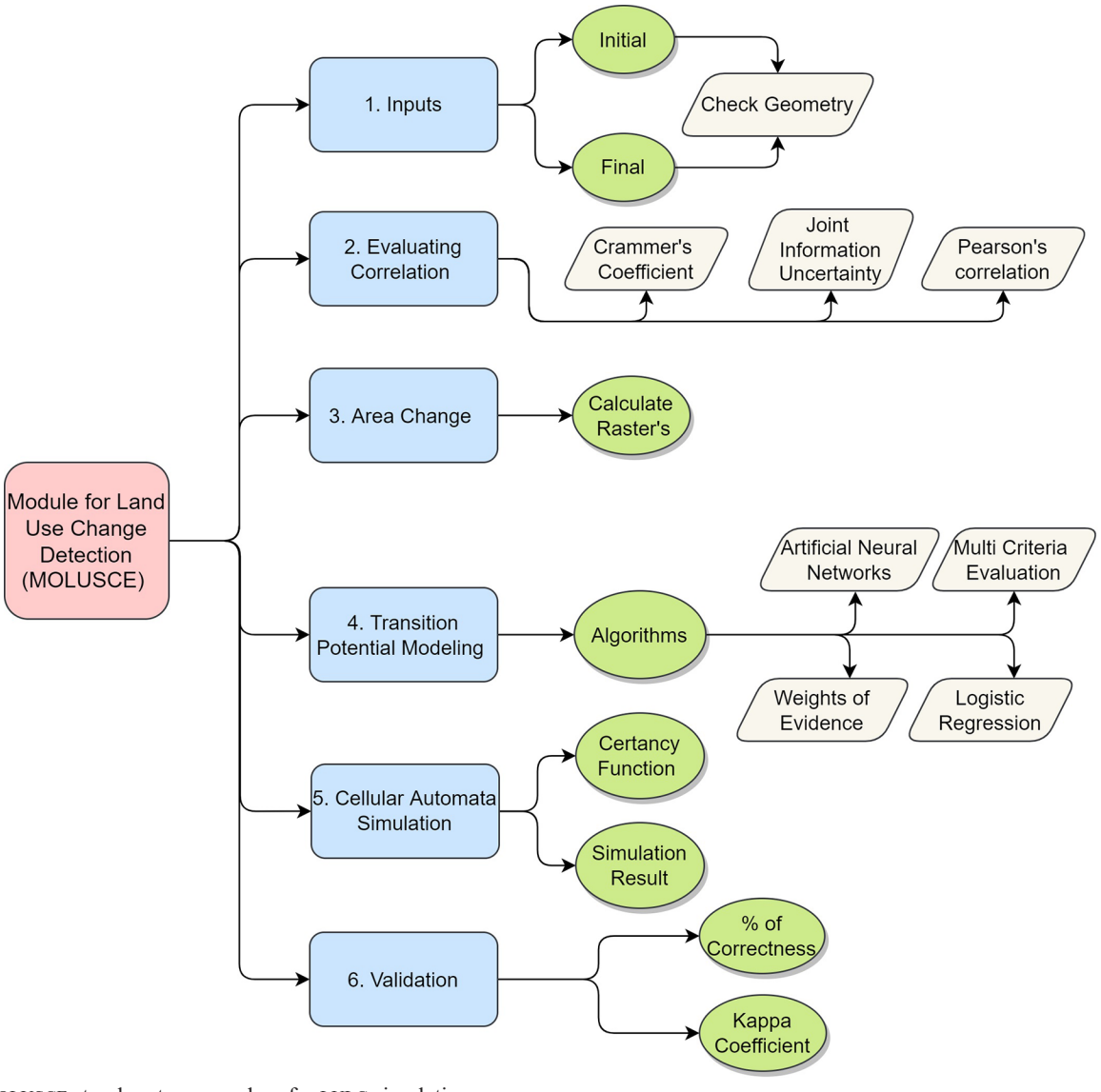

Figure 3. MOLUSCE step-by-step procedure for LULC simulation.

scheme, there were four major classes for land use mapping such as urban area, vegetation, waterbodies, and barren land. Land-use and land-cover classification has been performed by creating ROIs using manual digitization for each class. Furthermore, for each class, more than 4500 ROIs were created and the SAM algorithm was used for classification.

Dependent Variables and Their Integration in LULC *Simulations*

For more accurate simulations, we integrated some additional raster layers in the cellular automata algorithm such as DEM, distance from roads, distance from waterways, and distance from water bodies respectively, as shown in Figure 4. These spatial variables had a significant influence on the predicted results of LULC using CA-ANN. Furthermore, these factors are acute to study area because waterbodies, road infrastructure, and terrain (height) have had an impact on the city expansion in the last three decades (Abd EL-kawy *et al.* 2019; Imran and Mehmood 2020). These distance maps were created in ArcMap using spatial analysis and algebra tools such as (i) Euclidean distance, (ii) extract by mask, and (iii) reclassify. During the simulation process of 2030, we integrate these dependent variable maps with the initial (2010) and final (2020) maps and vice-versa for 2040.

Results and Discussions

This section explains the results and findings, for LULC historical modeling and future prediction through the methods and processing discussed in the section "Materials and Methods". We found that LULC patterns have increased in Lahore from 2000 to 2020. The results are further explained below individually.

LULC Change and Prediction Modeling from 2000 to 2040

The land-use change patterns as shown in Figure 6 were obtained for 2000, 2010, and 2020 respectively using the SAM classification algorithm processed in SCP-QGIS. The SAM algorithm has provided more prompt results as compared to maximum likelihood and minimum distance in SCP. It can be seen from research finding that LULC has significant impacts on the degradation of vegetation and water resources. According to the results in Figure 5 and Figure 6, it can be seen that most of the developments are observed in urban areas, with degradation in vegetation, barren land, and waterbodies, respectively.

Table 3 shows the overall land-use transformation in sq. km. from 2000 to 2020 (three decades) and the accuracy assessment information with an overall accuracy of 89%. Thus, the results of LULC analysis revealed that about 27.41% of the urban area has been increased from 2000 to 2020, while about 42.13% of vegetation and 6.51% of water bodies were degraded or converted into urban area land use.

According to (Gazi *et al.* 2021), there are several factors involved in land-use transformation, such as urbanization, population growth, and migration of people towards urban cores. Lahore is Pakistan's rapidly developing economic hub and faces numerous environmental and socio-economic challenges (Anjum *et al.* 2021).

Neural network learning curves are commonly used in machine learning algorithms and deep learning neural networks (Cohen *et al.*

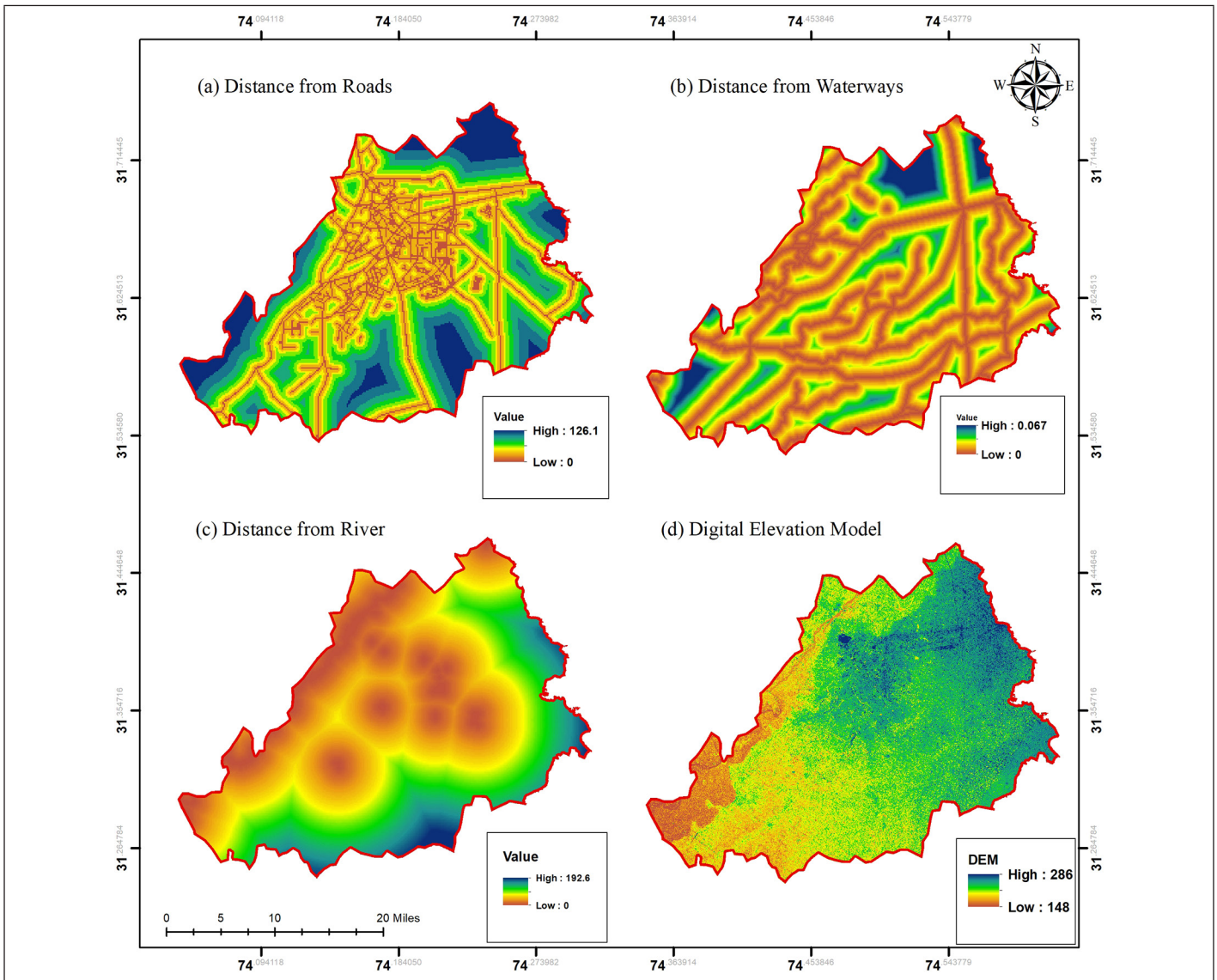

Figure 4. Dependent variables used for future prediction of land use/land cover.

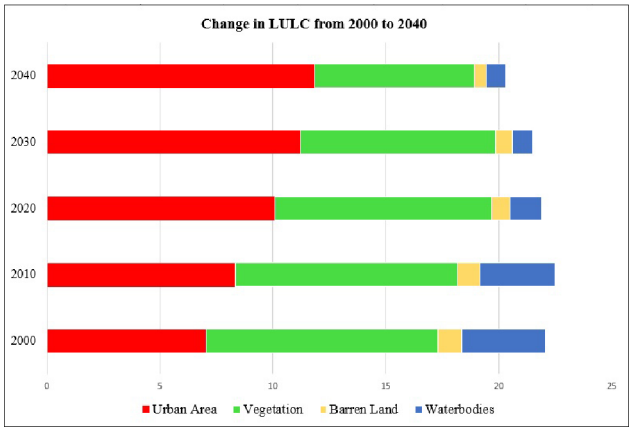

Figure 5. Land use/land cover (LULC) change and future prediction (2000–2040) in Lahore City.

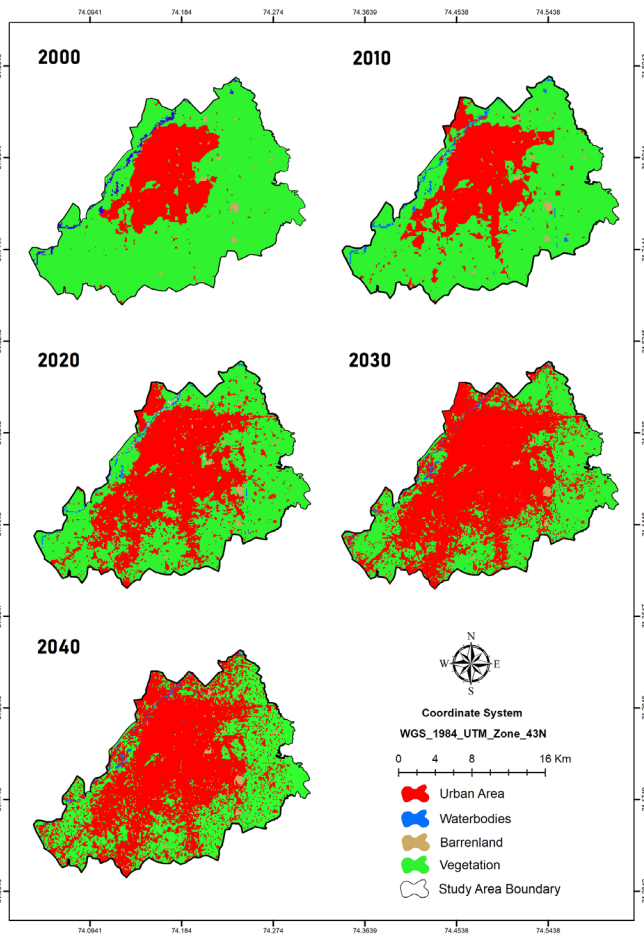

Figure 6. Historical land use/land cover change and future prediction for 2030 and 2040 using cellular automata-artificial neural networks (CA-ANN).

Table 3. Land use/land cover area change (sq. km) from 2000–2020.

	Year			Accuracy %
LULC Class	**2000**	**2010**	**2020**	**Overall 89**
Urban Area	705.73	832.45	1008.71	78
Vegetation	1026	987.12	959.12	85.5
Barren Land	10.26	9.8	8.1	95
Waterbodies	37.12	33.06	13.96	100

LULC = land use/land cover.

2021; Loureiro *et al.* 2021). Therefore, LULC simulations were predicted for the years 2030 and 2040 also presented in (Figure 6) via the cellular automata technique and neural network curves.

Furthermore, Table 4 shows the estimated change for each land use type from 2030 and 2040 and overall accuracy (82.4 %). The urban area is expected to grow by 23.15% between 2030 and 2040, whereas the amount of vegetation, bare land, and water bodies will all decrease by 28.05%, 3.5%, 1.8%, and 12.31%, respectively.

Table 4. LULC area change (sq. km) and Overall accuracy of 2030 and 2040 simulations.

	Year		Accuracy %
LULC Class	**2030**	**2040**	**Overall 82.4**
Urban Area	1184.97	1311.69	77.4
Vegetation	864.45	707.29	89.15
Barren Land	7.2	5.22	84
Waterbodies	9.08	8.83	79

LULC = land use/land cover.

Cross-Validation of the Results and Accuracy

In order to ensure that predictions made using LULC data were accurate, an CA-ANN model was first used to estimate the LULC for 2020. Therefore, first classified maps of 2000 and 2010 were used as input to predict 2020 simulated LULC map. After that simulation results of 2020 were compared with classified land use maps. The comparison between both output maps provided significant accuracy (up to 90%). Therefore, it was substantial to use CA-ANN simulation for future years. Therefore, the land use maps from 2020 and 2030 were used to anticipate 2040 LULC projection. Furthermore, we used MOLUSCE kappa validation technique to compare existing and projected LULC images to verify the model and prediction accuracy for our results. Thus, we found an overall accuracy for predicted land use (sum of 2030 and 2040) is 82.4%, indicating that simulated results are significant and consistent.

Moreover, the neural network curves also provide the cross validation of future simulations. These curves can be under-fit, over-fit, and good-fit, which reflects the accuracy (correctness) of the prediction. In addition, under-fitting occurs when model is too simplistic for data, over-fitting occurs when model is too sophisticated for data, and good fitting occurs when the validation and training data both are symmetrical. The neural network learning curves in this study were found a medium to good fit trend. Because the train and validation points curves were symmetrical, as shown in Figure 7 for 2030 and Figure 8 for 2040, respectively. The CA-ANN algorithm has effectively assessed historical LULC and predicted the future trends of land-use in Lahore.

A trend analysis was also performed to identify the direction of land use change in the study area. From trend analysis, we found that most of urban area was transformed in east and south-ward direction of the city. Figure 9 shows the overall trend of city expansion from year 2000 to 2040. It also indicates that the future urban development can be projected in the south and east region of the city by 2040. This trend makes it possible for urban planners to organize available land and resources for future sustainable urban development.

According to this research, the expansion of urban areas of the Lahore district is increasing high-temperature zones, and if this trend continues, the city will confront an urban heat island that can lead to more environmental issues in future. This study recommends that effective land management plans and policies must be developed and implemented to manage future LULC scenarios. Although Lahore is facing multiple challenges including energy consumption crises (Ahmad *et al.* 2022), clean water scarcity, urbanization, population growth, and smog, this study mainly aimed to monitor LULC from 2000 to 2040. These outcomes and findings can assist city planners in land-use planning, tree-cover preservation, agricultural land conservation, and environmental protection. Future advancements in geospatial methods like remote sensing technology can assist researchers more in future. It also motivates policymakers to pay greater attention to and invest more in geospatial infrastructure as a way to address the majority of environmental issues.

Conclusions

The core objective of this research work was to analyze the current status of LULC change and then to simulate the future patterns for LULC in Lahore using remote sensing imagery. We have implemented the CA-ANN algorithm using the MOLUSCE tool for future prediction. A machine learning-based model, SCP was adopted for LULU classification. The LULC maps were generated at 10-year intervals from 2000 to 2020 to detect the land-use change and future land-use patterns were predicted for the years 2030 and 2040. This study shows that about 27.41% of the urban area has been increased from 2000 to 2020 with a decrease of 42.13% in vegetation, 2.3% in the barren land, and 6.51% in water bodies, respectively. Also, projected that the urban area will increase by 23.15% from 2020 to 2040 while vegetation, barren land, and water bodies will decrease by 28.05%, 1.8%, and 12.31%,

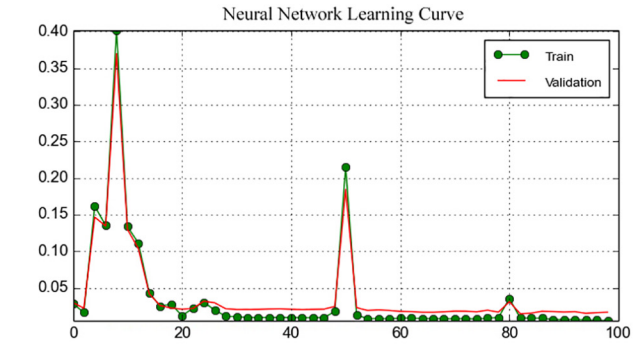

Figure 7. Neural network curve for 2030 land use/land cover predictions (good-fit).

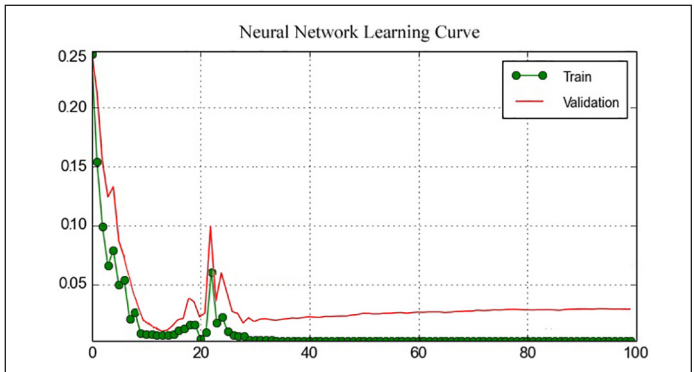

Figure 8. Neural network curve for 2040 land use/land cover predictions (good-fit).

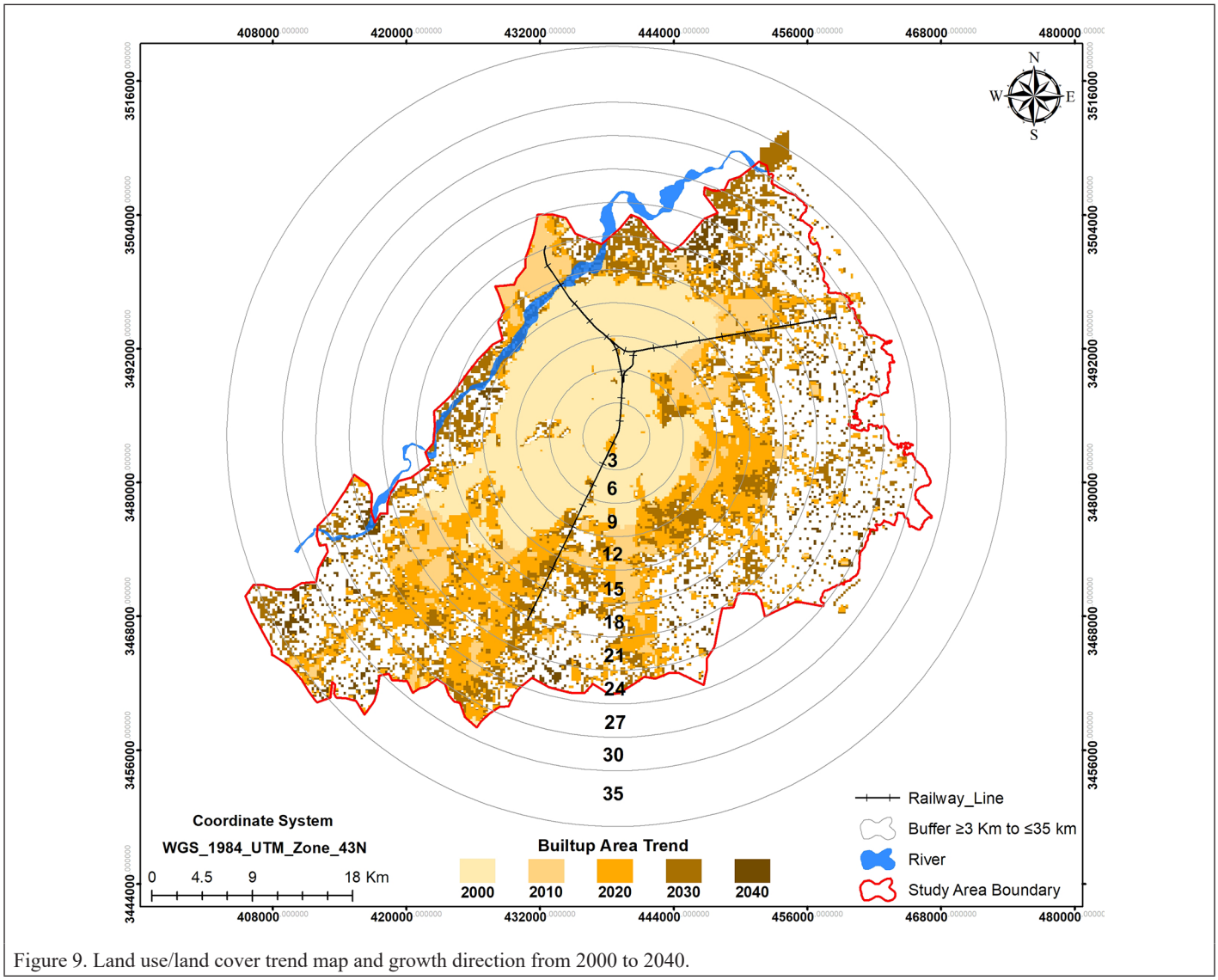

Figure 9. Land use/land cover trend map and growth direction from 2000 to 2040.

respectively. Therefore, it can be concluded that, concerning LULC, collectively 55.46% of the urban area will be increased in Lahore by 2040. The overall accuracy for land use future prediction is 82.4%, which indicates that simulated results are significant. It is concluded that this study can help in better preparedness for land-use planning in Lahore. It is also concluded that most of urban expansion was observed (Figure 9), in the eastern and southern parts of the city, that can assist urban planners to plan available land and resources for future sustainable city development. Our research findings also revealed that machine learning models such as MOLUSCE can process multispectral satellite imagery more quickly and can provide significant future simulation with high % of correctness. This research can also help on the national level to achieve sustainable development goals by 2030, especially in developing countries. By preserving ecological and agricultural land in the city area, government sectors can accomplish regulated urban expansion and planning.

Acknowledgments

The authors would like to thank the local and provincial government sectors for providing the statistical data. In addition to USGS and NASA, satellite imagery is freely available for researchers. The authors would like to thank the anonymous reviewers for their constructive comments and suggestions for improving the manuscript.

All persons who meet authorship criteria are listed as authors, and all authors certify that they have participated sufficiently in the work to take public responsibility for the content, including participation in the concept, design, analysis, writing, or revision of the manuscript. Furthermore, each author certifies that this material or similar material has not been submitted to published in any other journal.

This work was supported in part by the National Natural Science Foundation of China under Grants 42090012, in part by the Guangxi science and technology program Guangxi key R & D plan, GuiKe 2021AB30019 03 special research and 5G project of Jiangxi Province in China (20212ABC03A09); Zhuhai industry university research cooperation project of China (ZH22017001210098PWC) Sichuan Science and Technology Program 2022YFN0031; Hubei key R & D plan (2022BAA048), and Zhizhuo Research Fund on Spatial-Temporal Artificial Intelligence (Grant No.ZZJJ202202).

References

Abbas, Z., G. Yang, Y. Zhong and Y. Zhao. 2021. Spatiotemporal change analysis and future scenario of LULC using the CA-ANN approach: A case study of the greater bay area, China. *Land* 10(6):584.

Abd EL-kawy, O. R., H. A. Ismail, H. M. Yehia and M. A. Allam. 2019. Temporal detection and prediction of agricultural land consumption by urbanization using remote sensing. *The Egyptian Journal of Remote Sensing and Space Science* 22(3):237–246.

Abdullah, S., D. Barua, S. Abdullah, M. Abubakar and Y. W. Rabby. 2022. Investigating the impact of land use/land cover change on present and future land surface temperature (LST) of Chittagong, Bangladesh. *Earth Systems and Environment* 1–15.

Ahmad, M. N., Q. Cheng and F. Luo. 2022. dynamic linkage between urbanization, electrical power consumption, and suitability analysis using remote sensing and GIS techniques. *Photogrammetric Engineering & Remote Sensing* 88(3):171–179. https://doi.org/10.14358/PERS.21-00026R3.

Akbar, T. A., Q. K. Hassan, S. Ishaq, M. Batool, H. J. Butt and H. Jabbar. 2019. Investigative spatial distribution and modelling of existing and future urban land changes and its impact on urbanization and economy. *Remote Sensing* 11(2):105.

Al-Darwish, Y., H. Ayad, D. Taha and D. Saadallah. 2018. Predicting the future urban growth and it's impacts on the surrounding environment using urban simulation models: Case study of Ibb city–Yemen. *Alexandria Engineering Journal* 57(4):2887–2895.

Aneesha Satya, B., M. Shashi and P. Deva. 2020. Future land use land cover scenario simulation using open source GIS for the city of Warangal, Telangana, India. *Applied Geomatics* 12(3):281–290.

Anjum, M. S., S. M. Ali, M. A. Subhani, M. N. Anwar, A.-S. Nizami, U. Ashraf and M. F. Khokhar. 2021. An emerged challenge of air pollution and ever-increasing particulate matter in Pakistan; a critical review. *Journal of Hazardous Materials* 402:123943.

Baig, M. F., M. R. U. Mustafa, I. Baig, H. B. Takaijudin and M. T. Zeshan. 2022. Assessment of land use land cover changes and future predictions using CA-ANN simulation for Selangor, Malaysia. *Water* 14(3):402.

Bakker, D. M., H. Javed and Z. Ashfaq. 2022. Implementation and modelling of turf grass management options to improve soil carbon sequestration in a semi-arid environment. *Environmental Sustainability*:1–11.

Bhattacharjee, S. and J. Chen. 2020. Prediction of satellite-based column CO 2 concentration by combining emission inventory and LULC information. *IEEE Transactions on Geoscience and Remote Sensing* 58(12):8285–8300.

Chen, D., X. Lu, W. Hu, C. Zhang and Y. Lin. 2021. How urban sprawl influences eco-environmental quality: Empirical research in China by using the Spatial Durbin model. *Ecological Indicators* 131:108113.

Christovam, L. E., G. G. Pessoa, M. H. Shimabukuro and M. Galo. 2019. Land use and land cover classification using hyperspectral imagery: evaluating the performance of spectral angle mapper, support vector machine and random forest. *International Archives of the Photogrammetry, Remote Sensing & Spatial Information Sciences* XLII-2/W13:1841–1847. https://doi.org/10.5194/isprs-archives-XLII-2-W13-1841-2019.

Cohen, O., O. Malka and Z. Ringel. 2021. Learning curves for overparametrized deep neural networks: A field theory perspective. *Physical Review Research* 3(2):23034.

Congedo, L. 2021. Semi-automatic classification plugin: A Python tool for the download and processing of remote sensing images in QGIS. *Journal of Open Source Software* 6(64):3172.

De Lotto, R., M. Sessi and E. M. Venco. 2022. Semi-automatic method to evaluate ecological value of urban settlements with the biotope area factor index: Sources and logical framework. *Sustainability* 14(4):1993.

Dewan, A. M. and Y. Yamaguchi. 2009. Land use and land cover change in Greater Dhaka, Bangladesh: Using remote sensing to promote sustainable urbanization. *Applied Geography* 29(3):390–401.

Fahad, S., W. Li, A. H. Lashari, A. Islam, L. H. Khattak and U. Rasool. 2021. Evaluation of land use and land cover Spatio-temporal change during rapid Urban sprawl from Lahore, Pakistan. *Urban Climate* 39:100931. https://doi.org/10.1016/j.uclim.2021.100931.

Farid, N., M. F. U. Moazzam, S. R. Ahmad, R. Coluzzi and M. Lanfredi. 2022. Monitoring the impact of rapid urbanization on land surface temperature and assessment of surface urban heat island using Landsat in megacity (Lahore) of Pakistan. *Frontiers in Remote Sensing* 3:897397. https://doi.org/10.3389/frsen.2022.897397.

Gazi, M., M. Rahman, M. Uddin and F. M. Rahman. 2021. Spatio-temporal dynamic land cover changes and their impacts on the urban thermal environment in the Chittagong metropolitan area, Bangladesh. *GeoJournal* 86(5):2119–2134.

Ghalehteimouri, K. J., A. Shamsoddini, M. N. Mousavi, F.B.C. Ros and A. Khedmatzadeh. 2022. Predicting spatial and decadal of land use and land cover change using integrated cellular automata Markov chain model based scenarios (2019–2049) Zarriné-Rūd river basin in Iran. *Environmental Challenges* 6:100399.

Girma, R., C. Fürst and A. Moges. 2022. Land use land cover change modeling by integrating artificial neural network with cellular Automata-Markov chain model in Gidabo river basin, main Ethiopian rift. *Environmental Challenges* 6:100419.

Guidigan, M.L.G., C. L. Sanou, D. S. Ragatoa, C. O. Fafa and V. N. Mishra. 2019. Assessing land use/land cover dynamic and its impact in Benin Republic using land change model and CCI-LC products. *Earth Systems and Environment* 3(1):127–137.

Hamedianfar, A., M.B.A. Gibril, M. Hosseinpoor and P.K.E. Pellikka. 2020. Synergistic use of particle swarm optimization, artificial neural network, and extreme gradient boosting algorithms for urban LULC mapping from WorldView-3 images. *Geocarto International*:1–19.

Hassan, M. M. 2017. Monitoring land use/land cover change, urban growth dynamics and landscape pattern analysis in five fastest urbanized cities in Bangladesh. *Remote Sensing Applications: Society and Environment* 7:69–83.

Hong, C. 2022. "Safe Cities" in Pakistan: Knowledge infrastructures, urban planning, and the security state. *Antipode* 54(5): 1476–1496.

Hoque, M. Z., I. Islam, M. Ahmed, S. S. Hasan and F. A. Prodhan. 2022. Spatio-temporal changes of land use land cover and ecosystem service values in coastal Bangladesh. *The Egyptian Journal of Remote Sensing and Space Science* 25(1):173–180.

Hossain, M. T., T. Zarin, M. R. Sahriar and M. N. Haque. 2022. Machine learning based modeling for future prospects of land use land cover change in Gopalganj District, Bangladesh. *Physics and Chemistry of the Earth, Parts A/B/C* 126:103022.

Hou, L., F. Wu and X. Xie. 2020. The spatial characteristics and relationships between landscape pattern and ecosystem service value along an urban-rural gradient in Xi'an city, China. *Ecological Indicators* 108:105720.

Hu, X., F. Liu, X. Li, Y. Qi and J. Zhang. 2022. A novel strategy to assimilate category variables in land-use models based on Dirichlet distribution. *Environmental Modelling & Software*:105324.

Huang, A., Y. Xu, P. Sun, G. Zhou, C. Liu, L. Lu, Y. Xiang and H. Wang. 2019. Land use/land cover changes and its impact on ecosystem services in ecologically fragile zone: A case study of Zhangjiakou City, Hebei Province, China. *Ecological Indicators* 104:604–614.

Hussain, Z. and O. Nadeem. 2021. The nexus between growth strategies of master plans and spatial dynamics of a metropolitan city: The case of Lahore, Pakistan. *Land Use Policy* 109:105609.

Imran, M. and A. Mehmood. 2020. Analysis and mapping of present and future drivers of local urban climate using remote sensing: A case of Lahore, Pakistan. *Arabian Journal of Geosciences* 13(6):1–14.

Islam, M. R., M.N.I. Khan, M. Z. Khan and B. Roy. 2021. A three decade assessment of forest cover changes in Nijhum dwip national park using remote sensing and GIS. *Environmental Challenges* 4:100162.

Jabbar, M. and M. M. Yusoff. 2022. Assessing the spatiotemporal urban green cover changes and their impact on land surface temperature and urban heat island in Lahore (Pakistan). *Geography, Environment, Sustainability* 15(1):130–140.

Jabeen, F., M. Adrees, M. Ibrahim, A. Mahmood, S. Khalid, H.F.K. Sipra, A. Bokhari, M. Mubashir, K. S. Khoo and P. L. Show. 2022. Trash to energy: A measure for the energy potential of combustible content of domestic solid waste generated from an industrialized city of Pakistan. *Journal of the Taiwan Institute of Chemical Engineers*:104223.

Kafy, A.-A., N. N. Dey, A. Al Rakib, Z. A. Rahaman, N.M.R. Nasher and A. Bhatt. 2021. Modeling the relationship between land use/land cover and land surface temperature in Dhaka, Bangladesh using CA-ANN algorithm. *Environmental Challenges* 4:100190.

Kamaraj, M. and S. Rangarajan. 2022. Predicting the future land use and land cover changes for Bhavani basin, Tamil Nadu, India, using QGIS MOLUSCE plugin. *Environmental Science and Pollution Research*:1–12.

Khan, F., B. Das and P. Mohammad. 2022. Urban growth modeling and prediction of land use land cover change over Nagpur City, India using cellular automata approach. In *Geospatial Technology for Landscape and Environmental Management*, 261–282. Singapore: Springer.

Li, D., J. Ma, T. Cheng, J. L. van Genderen and Z. Shao. 2019. Challenges and opportunities for the development of MEGACITIES. *International Journal of Digital Earth* 12(12):1382–1395. https://doi.org/10.1080/17538947.2018.1512662.

Loureiro, B., C. Gerbelot, H. Cui, S. Goldt, F. Krzakala, M. Mézard and L. Zdeborová. 2021. Learning curves of generic features maps for realistic datasets with a teacher-student model. *Advances in Neural Information Processing Systems*:34.

Marondedze, A. K. and B. Schütt. 2021. Predicting the impact of future land use and climate change on potential soil erosion risk in an urban district of the Harare Metropolitan Province, Zimbabwe. *Remote Sensing* 13(21):4360.

Maung, W. S. and J. Sasaki. 2021. Assessing the natural recovery of mangroves after human disturbance using neural network classification and Sentinel-2 imagery in Wunbaik Mangrove Forest, Myanmar. *Remote Sensing* 13(1):52.

Mohammad, P., A. Goswami, S. Chauhan and S. Nayak. 2022. Machine learning algorithm based prediction of land use land cover and land surface temperature changes to characterize the surface urban heat island phenomena over Ahmedabad city, India. *Urban Climate* 42:101116.

Muhammad, R., W. Zhang, Z. Abbas, F. Guo and L. Gwiazdzinski. 2022. Spatiotemporal change analysis and prediction of future land use and land cover changes using QGIS MOLUSCE plugin and remote sensing big data: A case study of Linyi, China. *Land* 11(3):419.

Mwabumba, M., B. K. Yadav, M. J. Rwiza, I. Larbi and S. Twisa. 2022. Analysis of land use and land-cover pattern to monitor dynamics of Ngorongoro world heritage site (Tanzania) using hybrid cellular automata-Markov model. *Current Research in Environmental Sustainability* 4:100126.

Naikoo, M. W., A.R.M.T. Islam, J. Mallick and A. Rahman. 2022. Land use/land cover change and its impact on surface urban heat island and urban thermal comfort in a metropolitan city. *Urban Climate* 41:101052.

Nappo, N., O. Mavrouli, F. Nex, C. van Westen, R. Gambillara and A. M. Michetti. 2021. Use of UAV-based photogrammetry products for semi-automatic detection and classification of asphalt road damage in landslide-affected areas. *Engineering Geology* 294:106363.

Nath, B., W. Ni-Meister and R. Choudhury. 2021. Impact of urbanization on land use and land cover change in Guwahati city, India and its implication on declining groundwater level. *Groundwater for Sustainable Development* 12:100500.

Rehman, A., J. Qin, A. Pervez, M. S. Khan, S. Ullah, K. Ahmad and N. U. Rehman. 2022. Land-use/land cover changes contribute to land surface temperature: A case study of the Upper Indus Basin of Pakistan. *Sustainability* 14(2):934.

Riad, P., S. Graefe, H. Hussein and A. Buerkert. 2020. Landscape transformation processes in two large and two small cities in Egypt and Jordan over the last five decades using remote sensing data. *Landscape and Urban Planning* 197:103766.

Shafizadeh-Moghadam, H., M. Minaei, R. G. Pontius Jr, A. Asghari and H. Dadashpoor. 2021. Integrating a forward feature selection algorithm, random forest, and cellular automata to extrapolate urban growth in the Tehran-Karaj Region of Iran. *Computers, Environment and Urban Systems* 87:101595.

Sohl, T. and B. Sleeter. 2012. 15 role of remote sensing for land-use and land-cover change modeling. *Remote Sensing of Land Use and Land Cover*:225.

Talukdar, S., P. Singha, S. Mahato, S. Pal, Y.-A. Liou and A. Rahman. 2020. Land-use land-cover classification by machine learning classifiers for satellite observations—A review. *Remote Sensing* 12(7):1135.

Tempa, K. and K. R. Aryal. 2022. Semi-automatic classification for rapid delineation of the geohazard-prone areas using Sentinel-2 satellite imagery. *SN Applied Sciences* 4(5):1–14.

Tolentino, F. M. and M. de L.B.T. Galo. 2021. Selecting features for LULC simultaneous classification of ambiguous classes by artificial neural network. *Remote Sensing Applications: Society and Environment* 24:100616.

Ullah, S., A. A. Tahir, T. A. Akbar, Q. K. Hassan, A. Dewan, A. J. Khan and M. Khan. 2019. Remote sensing-based quantification of the relationships between land use land cover changes and surface temperature over the Lower Himalayan Region. *Sustainability* 11(19):5492.

Verma, P., A. Raghubanshi, P. K. Srivastava and A. S. Raghubanshi. 2020. Appraisal of kappa-based metrics and disagreement indices of accuracy assessment for parametric and nonparametric techniques used in LULC classification and change detection. *Modeling Earth Systems and Environment* 6(2):1045–1059.

Zhang, B. and H. Wang. 2021. A new type of dual-scale neighborhood based on vectorization for cellular automata models. *GIScience & Remote Sensing* 58(3):386–404.

Zhang, D., M. S. Sial, N. Ahmad, A. J. Filipe, P. A. Thu, M. Zia-Ud-Din and A. B. Caleiro. 2021. Water scarcity and sustainability in an emerging economy: a management perspective for future. *Sustainability* 13(1):144.

Zhang, L., Z. Shao, J. Liu and Q. Cheng. 2019. Deep learning based retrieval of forest aboveground biomass from combined LiDAR and Landsat 8 data. *Remote Sensing* 11(12):1459. https://doi.org/10.3390/rs11121459.

Zhang, M., C. Zhang, A.-A. Kafy and S. Tan. 2022. Simulating the relationship between land use/cover change and urban thermal environment using machine learning algorithms in Wuhan City, China. *Land* 11(1):14.

Zhou, Y., M. Chen, Z. Tang and Z. Mei. 2021. Urbanization, land use change, and carbon emissions: Quantitative assessments for city-level carbon emissions in Beijing-Tianjin-Hebei region. *Sustainable Cities and Society* 66:102701.

Zhu, Q., X. Guo, W. Deng, Q. Guan, Y. Zhong, L. Zhang and D. Li. 2022. Land-use/land-cover change detection based on a Siamese global learning framework for high spatial resolution remote sensing imagery. *ISPRS Journal of Photogrammetry and Remote Sensing* 184:63–78.

Call for *PE&RS* Special Issue Submissions

Innovative Methods for Geospatial Data using Remote Sensing and GIS

Internationally comparable data is a global need for managing resources, monitoring current trends and taking actions for sustainable living. Even though there has been a significant progress on geospatial data availability, extensive data gaps are still a major problem for general assessment and supervise the progress through the years. According to United Nations 2022 The Sustainable Development Goals Report, while health and energy sectors have the highest data available, limited data available for climate action.

The COVID-19 crisis has also shown that there are innovative data collection methods utilizing information and computer technologies. However, only 5% of the countries have benefit from remote sensing technologies to measure the impact of COVID-19. Additionally, novel approaches such as artificial intelligence should be used in conjunction with assessments to make sure they are put to use for critical situations.

The recent developments in remote sensing, geographic information systems and ICT have provided a wide accessibility to create geospatial data for various purposes. The proposed special issue focuses on *"Innovative Methods for Geospatial Data using Remote Sensing and GIS" for wide range of applications. This special issue aims to bring researchers to share knowledge and their expertise about innovative methods to contribute to fill data gaps around the world for a better future.*

The proposed special issue aims to contributes ASPRS's key mission on 'Simplify and promote the use of image-based geospatial technologies for the end-user', 'Promote collaboration between end users and geospatial experts to match data and technology to applications and solutions' and 'promote the transfer of geospatial data and information technology to developing nations' by providing innovative methods to create geospatial data using remote sensing and geographic information systems utilizing state-of-the-art developments and solutions.

Deadline for Manuscript Submission—July 1, 2023

Submit your Manuscript to http://asprs-pers.edmgr.com

Guest Editors

Dr. Tolga Bakirman, bakirman@yildiz.edu.tr , *Yildiz Technical University, Department of Geomatic Engineering*, Davutpasa Campus, 34220 Esenler-Istanbul/Turkey

Dr. George Arampatzis, garampatzis@pem.tuc.gr, *Technical University Crete, School of Production Engineering & Management*, 73100 Chania – Crete/Greece

WHO'S WHO IN ASPRS

Founded in 1934, the American Society for Photogrammetry and Remote Sensing (ASPRS) is a scientific association serving thousands of professional members around the world. Our mission is to advance knowledge and improve understanding of mapping sciences to promote the responsible applications of photogrammetry, remote sensing, geographic information systems (GIS) and supporting technologies.

BOARD OF DIRECTORS

BOARD OFFICERS

President
Christopher Parrish, Ph.D
Oregon State University

President-Elect
Lorraine B. Amenda, PLS, CP
Towill, Inc.

Vice President
Bandana Kar
Oak Ridge National Lab

Past President
Jason M. Stoker, Ph.D,
U.S. Geological Survey

Treasurer
John McCombs
NOAA

Secretary
Harold Rempel
ESP Associates, Inc.

COUNCIL OFFICERS

ASPRS has six councils. To learn more, visit https://www.asprs.org/Councils.html.

Sustaining Members Council
Chair: Ryan Bowe
Deputy Chair: Melissa Martin

Technical Division Directors Council
Chair: Bill Swope
Deputy Chair: Hope Morgan

Standing Committee Chairs Council
Chair: David Stolarz
Deputy Chair: TBA

Early-Career Professionals Council
Chair: Madeline Stewart
Deputy Chair: Kyle Knapp

Region Officers Council
Chair: Demetrio Zourarakis
Deputy Chair: Jason Krueger

Student Advisory Council
Chair: Lauren McKinney-Wise
Deputy Chair: Oscar Duran

TECHNICAL DIVISION OFFICERS

ASPRS has seven professional divisions. To learn more, visit https://www.asprs.org/Divisions.html.

Geographic Information Systems Division
Director: Denise Theunissen
Assistant Director: Jin Lee

Lidar Division
Director: Ajit Sampath
Assistant Director: Mat Bethel

Photogrammetric Applications Division
Director: Ben Wilkinson
Assistant Director: Hank Theiss

Primary Data Acquisition Division
Director: Greg Stensaas
Assistant Director: Srini Dharmapuri

Professional Practice Division
Director: Bill Swope
Assistant Director: Hope Morgan

Remote Sensing Applications Division
Director: Amr Abd-Ehrahman
Assistant Director: Tao Liu

Unmanned Autonomous Systems (UAS)
Director: Jacob Lopez
Assistant Director: Bahram Salehi

REGION PRESIDENTS

ASPRS has 13 regions to serve the United States. To learn more, visit https://www.asprs.org/regions.html.

Alaska Region

Cascadia Region
Robert Hariston-Porter

Eastern Great Lakes Region
Michael Joos, CP, GISP

Florida Region
Xan Fredericks

Heartland Region
Whit Lynn

Intermountain Region
Robert T. Pack

Mid-South Region
David Hughes

Northeast Region

North Atlantic Region

Pacific Southwest Region
John Erickson, PLS, CP

Potomac Region
Dave Lasko

Rocky Mountain Region

Western Great Lakes Region
Adam Smith

SUSTAININGMEMBERS

ACI USA Inc.
Weston, Florida
https://acicorporation.com/
Member Since: 2/2018

Aerial Services, Inc.
Cedar Falls, Iowa
www.AerialServicesInc.com
Member Since: 5/2001

Airworks Solutions Inc.
Boston, Massachusetts
Member Since: 3/2022

Applanix
Richmond Hill, Ontario, Canada
http://www.applanix.com
Member Since: 7/1997

Ayres Associates
Madison, Wisconsin
www.AyresAssociates.com
Member Since: 1/1953

CT Consultants
Mentor, Ohio
Member Since: 3/2022

Dewberry
Fairfax, Virginia
www.dewberry.com
Member Since: 1/1985

Esri
Redlands, California
www.esri.com
Member Since: 1/1987

GeoCue Group
Madison, Alabama
http://www.geocue.com
Member Since: 10/2003

Geographic Imperatives LLC
Centennial, Colorado
Member Since: 12/2020

GeoWing Mapping, Inc.
Richmond, California
www.geowingmapping.com
Member Since: 12/2016

Halff Associates, Inc.
Richardson, Texas
www.halff.com
Member Since: 8/2021

Keystone Aerial Surveys, Inc.
Philadelphia, Pennsylvania
www.kasurveys.com
Member Since: 1/1985

Kucera International
Willoughby, Ohio
www.kucerainternational.com
Member Since: 1/1992

L3Harris Technologies
Broomfield, Colorado
www.l3harris.com
Member Since: 6/2008

Merrick & Company
Greenwood Village, Colorado
www.merrick.com/gis
Member Since: 4/1995

Nearmap
South Jordan, Utah
www.nearmap.com
Member Since: 6/2023

NV5 Geospatial
Sheboygan Falls, Wisconsin
www.quantumspatial.com
Member Since: 1/1974

Pickett and Associates, Inc.
Bartow, Florida
www.pickettusa.com
Member Since: 4/2007

Riegl USA, Inc.
Orlando, Florida
www.rieglusa.com
Member Since: 11/2004

Robinson Aerial Surveys, Inc.(RAS)
Hackettstown, New Jersey
www.robinsonaerial.com
Member Since: 1/1954

Sanborn Map Company
Colorado Springs, Colorado
www.sanborn.com
Member Since: 10/1984

Surdex Corporation
Chesterfield, Missouri
www.surdex.com
Member Since: 12/2011

Surveying And Mapping, LLC (SAM)
Austin, Texas
www.sam.biz
Member Since: 12/2005

T3 Global Strategies, Inc.
Bridgeville, Pennsylvania
https://t3gs.com/
Member Since: 6/2020

Towill, Inc.
San Francisco, California
www.towill.com
Member Since: 1/1952

Woolpert LLP
Dayton, Ohio
www.woolpert.com
Member Since: 1/1985

SUSTAININGMEMBER**BENEFITS**

Membership

- ✓ Provides a means for dissemination of new information
- ✓ Encourages an exchange of ideas and communication
- ✓ Offers prime exposure for companies

Benefits of an ASPRS Membership

- Complimentary and discounted Employee Membership*
- E-mail blast to full ASPRS membership*
- Professional Certification Application fee discount for any employee
- Member price for ASPRS publications
- Discount on group registration to ASPRS virtual conferences
- Sustaining Member company listing in ASPRS directory/website
- Hot link to company website from Sustaining Member company listing page on ASPRS website
- Press Release Priority Listing in *PE&RS* Industry News
- Priority publishing of Highlight Articles in *PE&RS* plus, 20% discount off cover fee
- Discount on *PE&RS* advertising
- Exhibit discounts at ASPRS sponsored conferences (exception ASPRS/ILMF)
- Free training webinar registrations per year*
- Discount on additional training webinar registrations for employees
- Discount for each new SMC member brought on board (Discount for first year only)

*quantity depends on membership level

PE&RS 2023 Advertising Rates & Specs

THE MORE YOU ADVERTISE THE MORE YOU SAVE! *PE&RS* offers frequency discounts. Invest in a three-times per year advertising package and receive a 5% discount, six-times per year and receive a 10% discount, 12-times per year and receive a 15% discount off the cost of the package.

	Sustaining Member Exhibiting at a 2023 ASPRS Conference	**Sustaining Member**	**Exhibitor**	**Non Member**
All rates below are for four-color advertisments				
Cover 1	$1,850	$2,000	$2,350	$2,500
In addition to the cover image, the cover sponsor receives a half-page area to include a description of the cover (maximum 500 words). The cover sponsor also has the opportunity to write a highlight article for the journal. Highlight articles are scientific articles designed to appeal to a broad audience and are subject to editorial review before publishing. The cover sponsor fee includes 50 copies of the journal for distribution to their clients. More copies can be ordered at cost.				
Cover 2	$1,500	$1,850	$2,000	$2,350
Cover 3	$1,500	$1,850	$2,000	$2,350
Cover 4	$1,850	$2,000	$2,350	$2,500
Advertorial	1 Complimentary Per Year	1 Complimentary Per Year	$2,150	$2,500
Full Page	$1,000	$1,175	$2,000	$2,350
2 page spread	$1,500	$1,800	$3,200	$3,600
2/3 Page	$1,100	$1,160	$1,450	$1,450
1/2 Page	$900	$960	$1,200	$1,200
1/3 Page	$800	$800	$1,000	$1,000
1/4 Page	$600	$600	$750	$750
1/6 Page	$400	$400	$500	$500
1/8 Page	$200	$200	$250	$250
Other Advertising Opportunities				
Employment Promotion	$500 (30 day web + 1 email) $300 (30 day web)	$500 (30 day web + 1 email) $300 (30 day web)	$500 (30 day web + 1 email) $300 (30 day web)	$500 (30 day web + 1 email) $300 (30 day web)
Dedicated Content Email blast	$3000	$3000	$3000	$3000
Newsletter Display Advertising	1 Complimentary Per Year	1 Complimentary Per Year	$500	$500
PE&RS Digital Edition Announcement E-Mail	$1000	$1000	$1000	$1000

A 15% commission is allowed to recognized advertising agencies

Ad Size	**Width**	**Height**
Cover (bleed only)	8.625"	11.25"
Full Page (bleed)	8.625"	11.25"
Full Page (trim)	8.375"	10.875"
2/3 Page Horizontal	7.125"	6.25"
2/3 Page Vertical	4.58"	9.625"
1/2 Page Horizontal	7.125"	4.6875"
1/2 Page Vertical	3.4375"	9.625"
1/3 Page Horizontal	7.125"	3.125"
1/3 Page Vertical	2.29"	9.625"
1/4 Page Horizontal	7.125"	2.34"
1/4 Page Vertical	3.4375"	4.6875"
1/8 Page Horizontal	7.125"	1.17"
1/8 Page Vertical	1.71875"	4.6875"

- Publication Size: 8.375" × 10.875" (W x H)
- Live area: 1/2" from gutter and 3/8" from all other edges
- No partial page bleeds
- Publication Style: Perfect bound
- Printing Method: Web offset press
- Software Used: PC InDesign
- Supported formats:
  TIFF, EPS, BMP, JPEG, PDF, PNG
  PC InDesign, Illustrator,
  and Photoshop

Send ad materials to:
Rae Kelley
rkelley@asprs.org

Ship inserts to:
Alicia Coard
Walsworth
2180 Maiden Lane
St. Joseph, MI 49085
888-563-3220 (toll free)
269-428-1021 (direct)
269-428-1095 (fax)
alicia.coard@walsworth.com

Special Advertising Opportunities

FRONT COVER SPONSORSHIP

A *PE&RS* cover sponsorship is a unique opportunity to capture the undivided attention of your target market through three premium points of contact.

1— *PE&RS* FRONT COVER

(Only twelve available, first-come, first-served)
PE&RS is world-renowned for the outstanding imagery displayed monthly on its front cover—and readers have told us they eagerly anticipate every issue. This is a premium opportunity for any company, government agency, university or non-profit organization to provide a strong image that demonstrates their expertise in the geospatial information industry.

2— FREE ACCOMPANYING "HIGHLIGHT" ARTICLE

A detailed article to enhance your cover image is welcome but not a condition of placing an image. Many readers have asked for more information about the covers and your article is a highly visible way to tell your story in more depth for an audience keenly interested in your products and services. No article is guaranteed publication, as it must pass ASPRS editorial review. For more information, contact Rae Kelley at rkelley@asprs.org.

3— FREE TABLE OF CONTENTS COVER DESCRIPTION

Use this highly visible position to showcase your organization by featuring highlights of the technology used in capturing the front cover imagery. Limit 200-word description.

Terms: Fifty percent nonrefundable deposit with space reservation and payment of balance on or before materials closing deadline.

Cover Specifications: Bleed size: 8 5/8" × 11 1/4", Trim: 8 3/8" × 10 7/8"

PRICING

	Sustaining Member Exhibiting at a 2023 ASPRS Conference	Sustaining Member	Exhibitor	Non Member
Cover 1	$1,850	$2,000	$2,350	$2,500

Belly Bands, Inserts, Outserts & More!

Make your material the first impression readers have when they get their copy of *PE&RS*. Contact Bill Spilman at bill@innovativemediasolutions.com

VENDOR SEMINARS

ASPRS Sustaining Members now have the opportunity to hold a 1-hour informational session as a Virtual Vendor Seminar that will be free to all ASPRS Members wishing to attend. There will be one opportunity per month to reach out to all ASPRS Members with a demonstration of a new product, service, or other information. ASPRS will promote the Seminar through a blast email to all members, a notice on the ASPRS web site home page, and ads in the print and digital editions of *PE&RS*.

The Virtual Seminar will be hosted by ASPRS through its Zoom capability and has the capacity to accommodate 500 attendees.

Vendor Seminars	
Fee	$2,500 (no discounts)

DIGITAL ADVERTISING OPPORTUNITIES

EMPLOYMENT PROMOTION

When you need to fill a position right away, use this direct, right-to-the-desktop approach to announce your employment opportunity. The employment opportunity will be sent once to all ASPRS members in our regular Wednesday email newsletter to members, and will be posted on the ASPRS Web site for one month. This type of advertising gets results when you provide a web link with your text.

Employment Opportunity	Net Rate
30-Day Web + 1 email	$500/opportunity
Web-only (no email)	$300/opportunity

Do you have multiple vacancies that need to be filled? Contact us for pricing details for multiple listings.

NEWSLETTER DISPLAY ADVERTISING

Your vertical ad will show up in the right hand column of our weekly newsletter, which is sent to more than 3,000 people, including our membership and interested parties. **Open Rate: 32.9%**

Newsletter vertical banner ad	Net Rate
180 pixels x 240 pixels max	$500/opportunity

DEDICATED CONTENT EMAIL BLAST

Send a dedicated email blast to the ASPRS email list. Advertiser supplies HTML (including images). Lead time: 14 days.

Materials	Net Rate
Advertiser supplies HTML, including images.	$3000/ opportunity

PE&RS Digital Edition

Digital Edition Announcement E-Mail: 5,800+

PE&RS is available online in both a public version that is available to anyone but does not include the peer-reviewed articles, and a full version that is available to ASPRS members only upon login.

The enhanced version of *PE&RS* contains hot links for all ASPRS Sustaining Member Companies, as well as hot links on advertisements, ASPRS Who's Who, and internet references.

Become a sponsor today!

The e-mail blast sponsorship opportunity includes a **180 x 240 pixel ad** in the email announcement that goes out to our membership announcing the availability of the electronic issue.

Digital Edition Opportunities	Net Rate
E-mail Blast Sponsorship*	$1,000

Landsat's Enduring Legacy

Pioneering Global Land Observations from Space

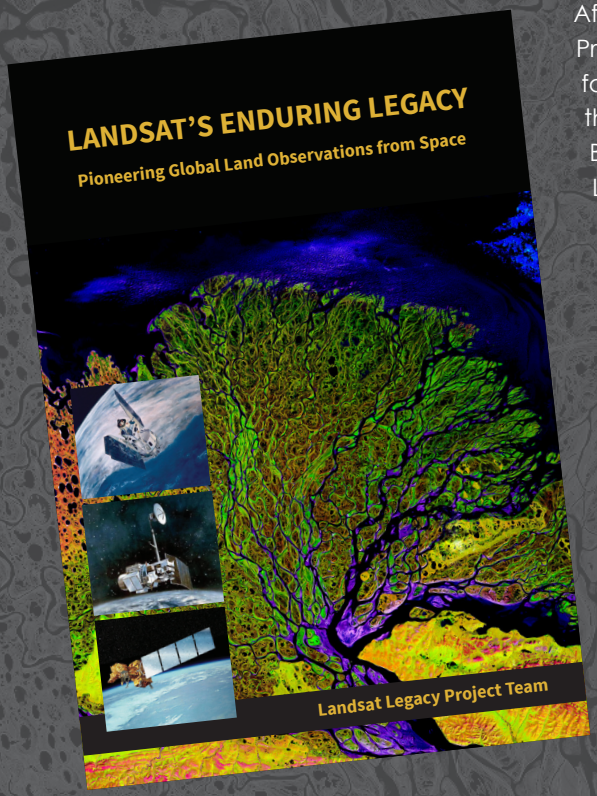

After more than 15 years of research and writing, the Landsat Legacy Project Team published, in collaboration with the American Society for Photogrammetry and Remote Sensing (ASPRS), a seminal work on the nearly half-century of monitoring the Earth's lands with Landsat. Born of technologies that evolved from the Second World War, Landsat not only pioneered global land monitoring but in the process drove innovation in digital imaging technologies and encouraged development of global imagery archives. Access to this imagery led to early breakthroughs in natural resources assessments, particularly for agriculture, forestry, and geology. The technical Landsat remote sensing revolution was not simple or straightforward. Early conflicts between civilian and defense satellite remote sensing users gave way to disagreements over whether the Landsat system should be a public service or a private enterprise. The failed attempts to privatize Landsat nearly led to its demise. Only the combined engagement of civilian and defense organizations ultimately saved this pioneer satellite land monitoring program. With the emergence of 21st century Earth system science research, the full value of the Landsat concept and its continuous 45-year global archive has been recognized and embraced. Discussion of Landsat's future continues but its heritage will not be forgotten.

The pioneering satellite system's vital history is captured in this notable volume on Landsat's Enduring Legacy.

Landsat Legacy Project Team

Samuel N. Goward
Darrel L. Williams
Terry Arvidson
Laura E. P. Rocchio
James R. Irons
Carol A. Russell
Shaida S. Johnston

Landsat's Enduring Legacy

Hardback. 2017, ISBN 1-57083-101-7

Member/Non-member	$48*
Student Member	$36*

* Plus shipping

Order online at

www.asprs.org/landsat

asprs THE IMAGING & GEOSPATIAL INFORMATION SOCIETY